TESIS DE LA UNIVERSIDAD
DE ZARAGOZA

2025

119

Pedro Luis Compais Serrano

Monitorización de la combustión de gas de alto horno con técnicas de visualización de imagen e inteligencia artificial

Director/es

Gil Martínez, Antonia
Arroyo Villanueva, Jorge

ISSN 2254-7606

Prensas de la Universidad
Universidad Zaragoza

Universidad de Zaragoza
Servicio de Publicaciones

ISSN 2254-7606

Tesis Doctoral

MONITORIZACIÓN DE LA COMBUSTIÓN DE GAS DE ALTO HORNO CON TÉCNICAS DE VISUALIZACIÓN DE IMAGEN E INTELIGENCIA ARTIFICIAL

Autor

Pedro Luis Compais Serrano

Director/es

Gil Martínez, Antonia
Arroyo Villanueva, Jorge

UNIVERSIDAD DE ZARAGOZA
Escuela de Doctorado

2025

Tesis Doctoral

Monitorización de la combustión de gas de alto horno con técnicas de visualización de imagen e inteligencia artificial

Autor

Pedro Luis Compais Serrano

Director/es

Antonia Gil Martínez
Jorge Arroyo Villanueva

Universidad de Zaragoza
2024

Monitorización de la combustión de gas de alto horno con técnicas de visualización de imagen e inteligencia artificial

Memoria realizada para optar al título de Doctor

Programa de doctorado en Energías Renovables y Eficiencia Energética

Dirigida por

Antonia Gil Martínez

Jorge Arroyo Villanueva

Instituto Universitario Mixto de la Energía y Eficiencia de los Recursos de Aragón ENERGAIA

Universidad de Zaragoza

2024

Resumen

Esta tesis doctoral tiene como objetivo la monitorización de la combustión de gas de alto horno a partir del desarrollo de un sistema de visión, basado en el procesamiento imágenes en color con técnicas de inteligencia artificial. Esta alternativa avanzada de diagnóstico de la combustión tiene un alto potencial para incrementar la precisión y rapidez de los sensores convencionales de temperatura y gases de combustión; una mejora de especial interés para la combustión de gas de alto horno y su mayor sensibilidad ante perturbaciones de operación. Con el desarrollo del sistema de visión se busca promover el consumo de gas de alto horno, incrementando la valorización de esta corriente residual generada en grandes cantidades durante la producción del acero, reduciendo así el consumo de combustibles fósiles e incrementando la descarbonización y sostenibilidad de los procesos siderúrgicos.

El trabajo de investigación incluye varias aportaciones alineadas con el objetivo de la tesis, descritas a continuación. Se ha analizado el estado del arte para la monitorización visual de llamas, incluyendo la extracción de características de imagen y su modelado con técnicas de aprendizaje automático. Se han realizado tres campañas experimentales centradas en la mezcla de combustible óptima para la valorización del gas de alto horno, adquiriendo imágenes de llama con distinta composición de combustible y relación aire-combustible, en escala de laboratorio y semiindustrial. Las imágenes se han procesado para extraer variables numéricas y entrenar modelos con técnicas de aprendizaje automático en la predicción del exceso de aire en la combustión.

A partir del trabajo realizado, se extraen varios resultados principales. En primer lugar, se ha conseguido la combustión en laboratorio de mezclas de gases con diferencias significativas en su poder calorífico, utilizando una única configuración de quemador, al igual que en condiciones industriales. En segundo lugar, tanto para la escala de laboratorio como para la semiindustrial, se ha confirmado la relación del exceso de aire de la combustión con al menos 51 características extraídas de imágenes de color. Por último, con las técnicas de modelado empleadas se ha conseguido predecir correctamente el exceso de aire para más del 95 % de las imágenes en la mayoría de las condiciones, obteniendo una precisión del 79 % en el peor escenario. El procesamiento definido en esta tesis ha permitido detectar pequeñas variaciones en la combustión y en las imágenes, alcanzando una precisión superior a la de trabajos previos e incluso a la del ojo humano.

Esta tesis ha propuesto, estudiado y validado un sistema de visión para la monitorización de la combustión de gas de alto horno. Para completar su madurez tecnológica y alcanzar su implementación final en la industria, esta tesis propone la adaptación de su procesamiento de imágenes para la supervisión individual de varios quemadores con una única cámara.

Nomenclatura y acrónimos

Nomenclatura

$[O_2]_{fg}$	Concentración de oxígeno en los gases de salida (%v)
T_{cc}	Temperatura de la cámara de combustión (°C)

Acrónimos

BFG	*Blast Furnace Gas*
COG	*Coke Oven Gas*
EA	Exceso de Aire
LR	*Logistic Regression*
MILD	*Moderate or Intense Low Oxygen Dilution*
MLP	*MultiLayer Perceptron*
PCI	Poder Calorífico Inferior
SE	Serie de Ensayos
SVM	*Support Vector Machine*

Informe compendio de publicaciones

Esta tesis doctoral se presenta en la modalidad de compendio de publicaciones, según la siguiente normativa.

- Acuerdo de 25 de junio de 2020, del Consejo de Gobierno de la Universidad, por el que se aprueba el Reglamento sobre Tesis Doctorales de la UZ.
- Procedimiento de depósito, autorización y defensa de tesis de la UZ (Comité de Dirección de la EDUZ, 28 de julio de 2020).

A continuación, se incluyen las referencias completas de los artículos que constituyen el cuerpo de la tesis.

I. Optical analysis of blast furnace gas combustion in a laboratory premixed burner. **P. Compais**, J. Arroyo, A. González-Espinosa, M. A. Castán-Lascorz, A. Gil. ACS Omega (2022); Vol. 7, pp. 24498-24510.

II. Detection of slight variations in combustion conditions with machine learning and computer vision. **P. Compais**, J. Arroyo, M. A. Castán-Lascorz, J. Barrio, A. Gil. Engineering Applications of Artificial Intelligence (2023); Vol. 126, 106772.

III. Flame monitoring system based on images for steel reheating furnaces: a case study of validation from laboratory to semi-industrial scales. **P. Compais**, J. Arroyo, V. Cuervo-Piñera, A. Gil. *Proceedings of the 18th Conference on Sustainable Development of Energy, Water and Environment Systems* (2023), Dubrovnik (Croatia).

IV. Promoting the valorization of blast furnace gas in the steel industry with the visual monitoring of combustion and artificial intelligence. **P. Compais**, J. Arroyo, F. Tovar, V. Cuervo-Piñera, A. Gil. Fuel (2024); Vol. 362, 130770.

Por último, se incluye una contribución adicional a congreso científico en la que el doctorando presentó parte de los resultados obtenidos en la línea de investigación de la tesis.

A. Experimental analysis of blast furnace gas co-firing in a semi-industrial furnace using colour images. P. Compais, J. Arroyo, A. González-Espinosa, C. Gonzalo-Tirado, M. A. Castán-Lascorz, J. Barrio, V. Cuervo-Piñera. *Proceedings of the 7th World Congress on Momentum, Heat and Mass Transfer* (2022), Virtual Conference.

Índice

Índice de figuras

Índice de tablas

1. Introducción general

El objetivo de esta tesis doctoral es el desarrollo de un sistema de monitorización para la combustión de gas de alto horno, a partir de la adquisición y procesamiento de imágenes en color con técnicas de inteligencia artificial. Las actividades principales de este trabajo incluyen la realización de pruebas experimentales, el procesamiento de imágenes, el ajuste de modelos predictivos y el análisis de resultados.

La tesis se enmarca en el programa de doctorado de Energías Renovables y Eficiencia Energética (Universidad de Zaragoza), en las líneas de investigación de eficiencia energética y procesos térmicos. El trabajo incluye un desarrollo semiindustrial en colaboración con ArcelorMittal, así como la difusión de los resultados a través de artículos, por lo que se presenta en la modalidad de doctorado industrial y mediante compendio de publicaciones.

La memoria se estructura en tres bloques principales. En primer lugar, la introducción general recoge la revisión bibliográfica, objetivos, unidad temática y trabajos realizados. Posteriormente se incluyen los artículos elaborados en el marco de la tesis, y, por último, se presentan las aportaciones y las conclusiones.

La tesis se fundamenta en la necesidad de incrementar la sostenibilidad de los procesos de producción, un problema crítico para las industrias con un alto consumo de energía, como la siderurgia. Una de las estrategias industriales para afrontar este desafío es la valorización de corrientes residuales, aprovechando por ejemplo el subproducto siderúrgico del gas de alto horno como combustible alternativo. Sin embargo, la combustión de este gas tiene una menor estabilidad, por lo que se pueden producir desviaciones respecto a las condiciones nominales. Estas perturbaciones reducen la eficiencia en la operación del horno, y en el peor escenario, extinguen o hacen retroceder la llama, incrementando también los tiempos de parada. En este sentido, se requiere una monitorización precisa para detectar esos cambios, reduciendo el tiempo de operación en condiciones subóptimas, y aumentando la eficiencia global del proceso. En el ámbito de la combustión, los sistemas de visión son una alternativa avanzada de supervisión, con un alto potencial para el control de procesos complejos. Esta tesis tiene como objetivo final dar respuesta a las necesidades de la planta de ArcelorMittal en Asturias, que busca promover la valorización del gas de alto horno mediante una mejor monitorización de su combustión.

1.1. Revisión bibliográfica

1.1.1. Situación actual

La sociedad actual necesita un modelo energético sostenible. Para conseguirlo, la Unión Europea ha marcado unos objetivos ambiciosos de descarbonización, con la reducción de emisiones en un 55 % para 2030, y la neutralidad climática para 2050. En este desafío, las acerías tienen un papel clave debido a dos de sus características. En primer lugar, la siderurgia es una industria de alto consumo con elevadas emisiones, que globalmente representa el 8 % de la demanda energética y el 7 % de las emisiones directas de CO_2 en el sistema energético [1]. En segundo lugar, el acero es crucial para nuestra sociedad, debido a su uso en la construcción de edificios e infraestructuras, así como en la fabricación de vehículos, la estructura de paneles fotovoltaicos, y el eje y la caja de cambios de aerogeneradores [2]. En números, el acero es el material con la tercera mayor producción global (1900 millones de toneladas anuales), siendo Europa el segundo mayor fabricante con un 9 % de la producción total.

Para incrementar la descarbonización de la industria se pueden estudiar distintas alternativas, como la flexibilidad eléctrica [3] y la recuperación de calor residual [4]. En Europa, la mayor parte del acero se produce a través de dos rutas: el alto horno-horno de oxígeno básico y el horno de arco eléctrico, responsables de alrededor del 60 y 40 % de la producción, respectivamente [5]. En el caso de la ruta de alto horno-horno de oxígeno básico (Figura 1), las emisiones también se pueden reducir haciendo modificaciones en los procesos productivos, como por ejemplo con el uso de biochar en vez de combustibles fósiles [7], o hidrógeno en lugar de carbón o coque para la reducción química del mineral de hierro en el alto horno [8]. No obstante, estas tecnologías tienen actualmente un coste elevado, y su implementación requiere de desarrollos adicionales. Otra alternativa para la descarbonización es la valorización de corrientes residuales [9], que en el caso de las siderurgias se centra en el uso de sus principales gases subproducto como combustible. Frente al uso de biochar e hidrógeno, esta estrategia de reducción de emisiones tiene la ventaja de que los gases combustibles se generan en elevadas cantidades en el propio proceso de producción del acero, pudiendo usarse en la misma acería donde se generan, y reduciendo así el consumo de gas natural e incrementando la sostenibilidad en las acerías europeas [10]. Por ello, la optimización de la combustión de estos gases es de vital importancia para la descarbonización siderúrgica.

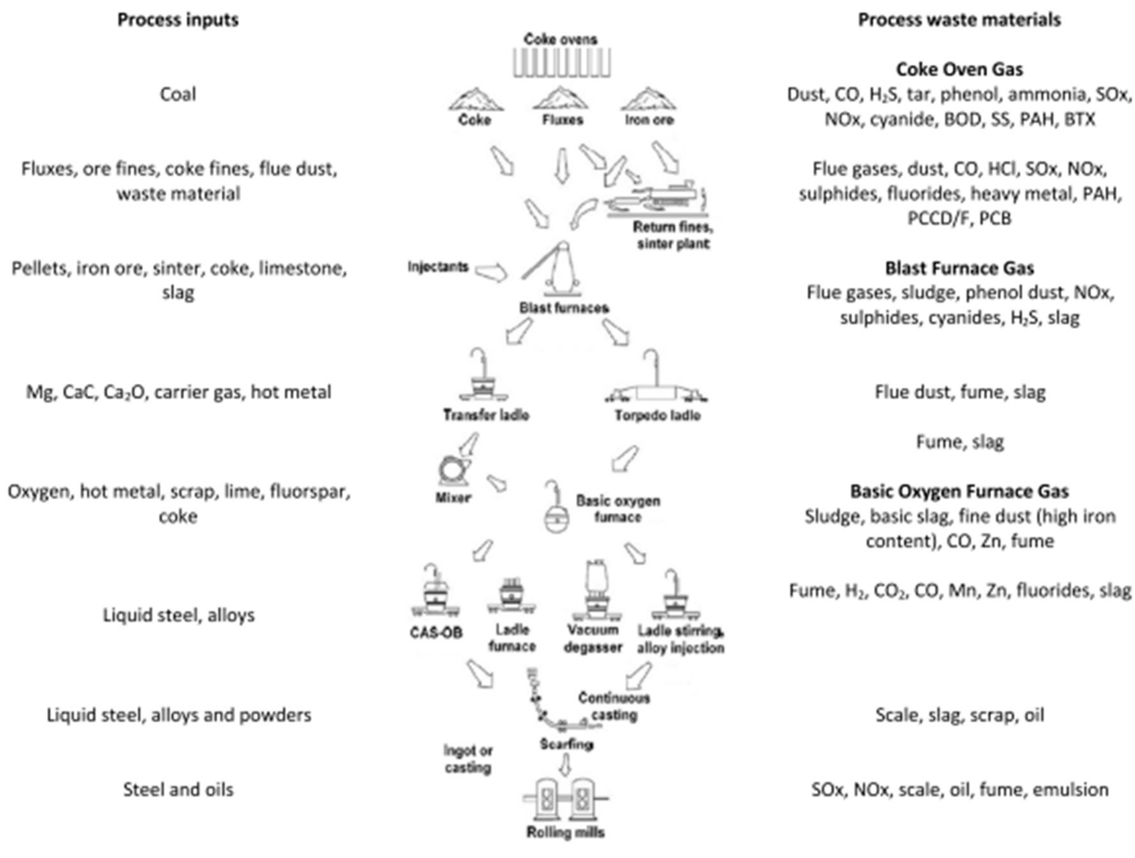

Figura 1. Resumen de la ruta del alto horno-horno de oxígeno básico [6].

En la ruta del alto horno-horno de oxígeno básico se generan tres corrientes residuales de gas: el gas de horno de coque (*Coke Oven Gas*, COG), el gas de horno de oxígeno básico, y el gas de alto horno (*Blast Furnace Gas*, BFG) [6]. La composición de estas corrientes depende de las propiedades de la materia prima utilizada y de las condiciones de operación de los hornos, por lo que sus valores fluctúan. Los rangos típicos de composición y Poder Calorífico Inferior (PCI) de estos gases se incluyen en la Tabla 1. A modo de ejemplo, se ha estimado que la valorización del gas de alto horno generado en la planta de ArcelorMittal Asturias proporcionaría ahorros anuales en la producción del acero de 200 GWh de energía consumida, 50.000 toneladas de emisión equivalente de CO_2 y 10 millones de euros de coste económico [11], [12]. Considerando el volumen de acero producido a escala europea [1], [5], la replicación de esta valorización alcanzaría un ahorro total 30 veces mayor.

Tabla 1. Rangos típicos de composición volumétrica y poder calorífico del gas de horno de coque, gas de alto horno, y gas de horno de oxígeno básico [6].

Corriente residual	Gas de horno de coque (COG)	Gas de alto Horno (BFG)	Gas de horno de oxígeno básico
[H_2] (%v.)	36 – 62	1 – 8	2 – 10
[CO] (%v.)	3 – 6	19 – 27	55 – 80
[CH_4] (%v.)	16 – 27	-	-
[C_xH_y] (%v.)	1 – 2	-	-
[CO_2] (%v.)	1 – 5	16 – 26	10 – 18
[N_2 + Ar] (%v.)	2 – 6	44 – 58	8 – 26
PCI (MJ/m^{3}N)	9 – 19	3 – 4	7 – 10

1.1.2. Combustión del gas de alto horno

El gas de alto horno posee una elevada concentración de gases inertes, y debido a ello, un reducido poder calorífico, diez veces menor al del gas natural. Por lo tanto, el uso del gas de alto horno en procesos de alta temperatura requiere del uso de estrategias adicionales, como su mezcla con combustibles con un mayor poder calorífico (gas natural o gas de horno de coque) [6], así como el precalentamiento del aire de combustión y el gas de alto horno a temperaturas entre 250 – 450 °C, y más recientemente, el empleo de quemadores de oxicombustión y regenerativos [13]. Otra consecuencia del bajo poder calorífico del gas de alto horno es su mayor inestabilidad en la combustión [14], [15]. Por lo tanto, las perturbaciones en la operación de quemadores pueden resultar en desviaciones más graves que para otros combustibles con una mayor densidad energética. Debido a ello, la combustión del gas de alto horno se beneficia de la implementación de monitorizaciones más precisas, con el objetivo de detectar pequeñas desviaciones en la operación y realizar una corrección más rápida.

1.1.3. Sistemas de visión e inteligencia artificial para la combustión

Los hornos industriales tienen múltiples quemadores (Figura 2), y el control de su rendimiento se centra en la medida de la temperatura y las concentraciones de oxígeno y monóxido de carbono en los gases de combustión. Además, las concentraciones de óxidos de nitrógeno y dióxido de azufre se monitorizan para controlar contaminantes. Los sensores tradicionales permiten monitorizar la operación del horno en distintos puntos del horno, pero la medida en todos los quemadores no es viable económicamente. Por ello, los gases de combustión se caracterizan únicamente a la salida del horno, realizando el control a partir de una variable promedio, lo que dificulta la detección de desviaciones en quemadores individuales.

Figura 2. Horno industrial con varios quemadores [16].

En contraposición a los sensores convencionales, una cámara permitiría monitorizar la operación del horno en distintos puntos, cuya información se puede registrar de manera simultánea con la adquisición de imágenes. De esta manera, un único sistema de visión podría controlar individualmente varios quemadores, con el objetivo de reducir los costes de operación y mantenimiento del horno. Los sistemas de visión capturan y procesan imágenes de llama para estimar variables de combustión, utilizando técnicas de inteligencia artificial. En los últimos años, esta tecnología se ha postulado como una alternativa avanzada para el diagnóstico de la combustión, por lo que ostenta un gran potencial para monitorizar la compleja operación de los quemadores con gas de alto horno.

Para describir más en detalle el funcionamiento de los sistemas de visión, esta tesis se basa en la nomenclatura utilizada en [17]. El concepto de inteligencia artificial se relaciona con dispositivos sintéticos capaces de comportarse como humamos, o incluso superarlos, aunque los sistemas actuales se centran en tareas concretas y limitadas. Dentro de este campo, la visión artificial se especializa en actividades con una componente visual significativa, cuya aplicación en la industria se conoce como visión de máquina. Estas últimas técnicas se dividen a su vez en varias tareas (Figura 3): adquisición de imágenes, preprocesamiento, segmentación, extracción de características e interpretación. La segmentación agrupa los píxeles de la imagen en distintas clases, lo que permite caracterizar la información en varias regiones de la imagen. En la fase de interpretación, las propiedades de los píxeles se asocian con variables del proceso industrial, cuya relación se puede modelar empíricamente utilizando otra rama de la inteligencia artificial: el aprendizaje automático. A continuación, se revisa la aplicación de la visión de máquina para la monitorización de la combustión.

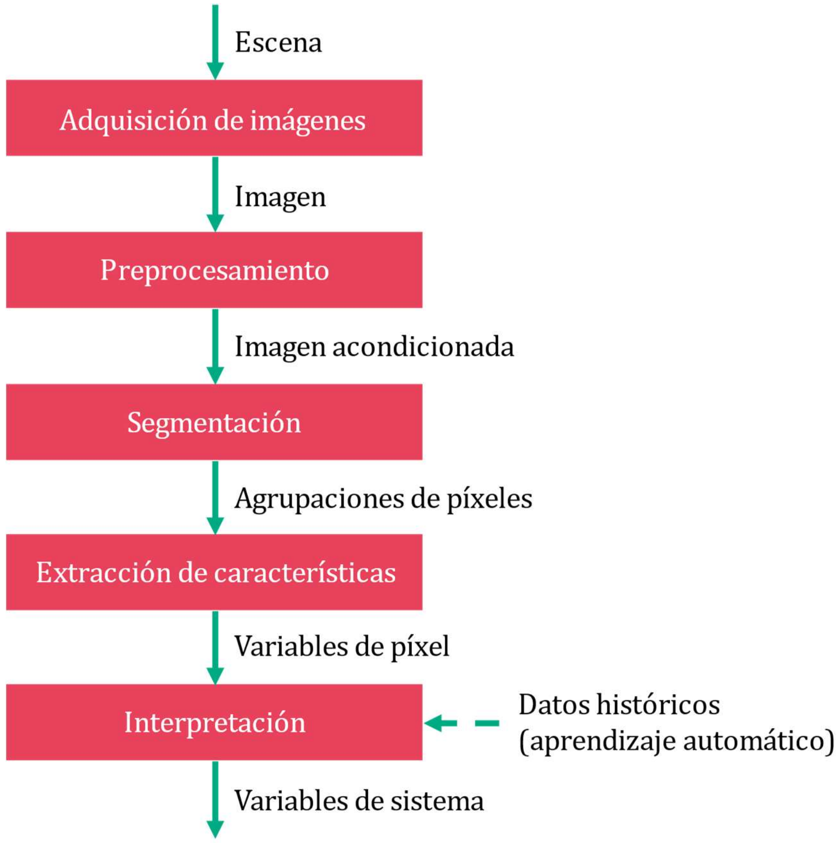

Figura 3. Operaciones realizadas por las aplicaciones de visión de máquina, siguiendo la terminología de [17].

1.1.4. Adquisición de imágenes de llamas en procesos de combustión

Las imágenes de llama capturadas por una cámara dependen de su energía radiante, que a su vez se relaciona con las condiciones de combustión. Por un lado, las llamas de difusión se caracterizan por la radiación continua de cuerpo gris emitida por las partículas de hollín [18], [19], cuya alta emisividad proporciona un comportamiento similar al de cuerpo negro. Por otro lado, las llamas de premezcla tienen una emisión en longitudes de onda discretas, asociadas a especies intermedias en la combustión (quimioluminiscencia de llama). En este caso, la energía se emite por la transición de dichas especies de estados energéticos excitados a fundamentales, resultando en una radiación azulada que depende de la composición de los reactivos [19] y de la relación aire-combustible [19], [20]. A modo de ejemplo, la Figura 4 muestra espectros de combustión del metano, etileno, etano y propano. El estudio de la quimioluminiscencia de llama se centra en el análisis de las emisiones de especies químicas concretas, principalmente OH^*, CH^*, C_2^* y CO_2^*. Mientras que el OH^* emite radiación en longitudes de onda en el rango ultravioleta (en torno a 310 nm) [21]-[26], el CH^* (430 nm) [21]-[26] y C_2^* (470 y 515 nm) [21], [23], [25] lo hacen en el rango visible. A diferencia de estos radicales, el CO_2^* presenta una radiación distribuida a lo largo del rango ultravioleta-visible (350-610 nm) [21], [22], [24], [25].

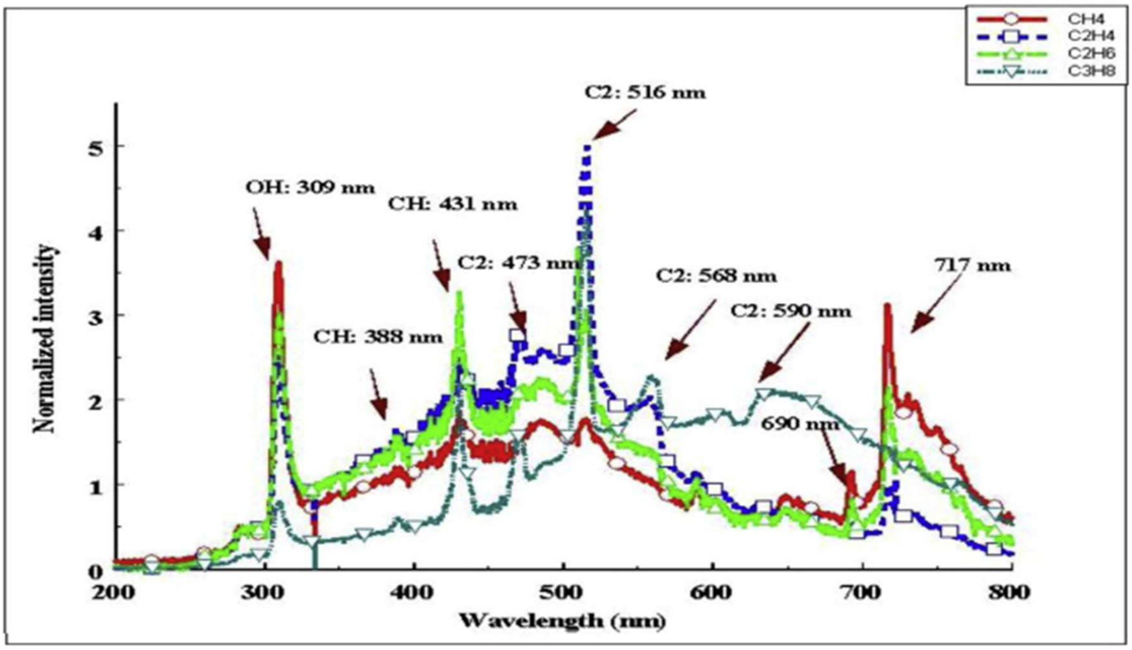

Figura 4. Espectros de la combustión de varios hidrocarburos, para un quemador de premezcla y una relación volumétrica aire-combustible de 8.57 [27].

Para estudiar una aplicación específica de monitorización de la combustión, se debe identificar la radiación emitida por las llamas, para luego escoger un sensor con la sensibilidad espectral adecuada. Existen distintos tipos de sensores, entre los que se encuentran los detectores de llama (para los rangos ultravioleta o infrarrojo), los espectrómetros, y más recientemente, las cámaras digitales. Con esta última tecnología, se pueden capturar imágenes tanto en el rango visible, como el ultravioleta e infrarrojo (termografía). También se dispone de filtros de paso banda, para adquirir únicamente la radiación asociada a un radical de la combustión [28]-[32]. En los últimos años ha aparecido la tecnología hiperespectral, que también permite obtener información detallada de cada longitud de onda sin necesidad de usar filtros adicionales, aunque a expensas de un coste superior [33].

Las aplicaciones de monitorización de la combustión pueden tener distintos requisitos de operación. En concreto, se distingue entre el uso para campañas puntuales en laboratorio y la monitorización continua en la industria, en la que se instalan equipos adicionales de refrigeración, control y extracción para cumplir con sus requisitos de operación más exigentes [34]. Actualmente se utilizan sistemas de visión comerciales en varias industrias, como las del vidrio y cemento (Figura 5), facilitando las labores de operación y mantenimiento. Estos equipos también pueden incluir el procesamiento e interpretación de las imágenes, aunque con métodos más básicos y menos personalizados que los considerados en el estado del arte.

(a)

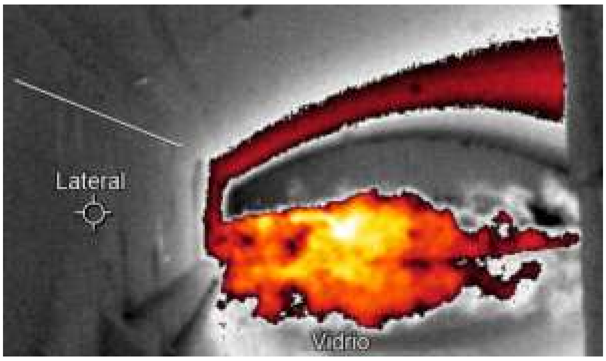

(b)

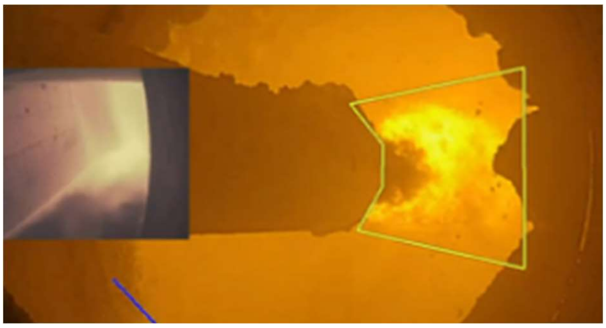

Figura 5. Imágenes postprocesadas y capturadas por (a) una cámara termográfica en un horno de fusión de vidrio [35], y (b) una cámara de color en un horno rotatorio de cemento [36].

1.1.5. Preprocesamiento, segmentación y extracción de características de imágenes de llama

La etapa de preprocesamiento tiene un carácter de apoyo a tareas posteriores en las aplicaciones de visión de máquina, y puede incluir operaciones como la transformación del espacio de color [37], [38], y el filtrado de ruido [39], [40]. Después del preprocesamiento se puede realizar la operación de segmentación para identificar los píxeles de llama, eliminando la influencia de factores ajenos en el diagnóstico visual [37], [41]. En la práctica, las llamas pueden tener una geometría difusa y variable, por lo que la segmentación puede ser imprecisa y reducir la eficacia de la monitorización. Por ello, también existe la alternativa de prescindir de la segmentación y supervisar de manera general la imagen [40], [42].

Para la caracterización de las imágenes de llama se dispone de un elevado número de propiedades visuales, por lo que la mayoría de los estudios escoge manualmente un conjunto limitado y específico de variables para su caso. No obstante, los parámetros más comunes se basan en las mismas propiedades de la llama: intensidad [37], [40], [41], [43]-[47], textura [40], [42] y geometría [37], [38], [48], [49]. Las características de intensidad incluyen por ejemplo la media o desviación estándar de los valores de intensidad de los píxeles. Las variables de textura suelen basarse en la matriz de coocurrencia de niveles de gris, que considera tanto la intensidad como la distribución espacial de los píxeles. Dicha matriz cuantifica el número combinaciones de intensidad para parejas de píxeles según una distancia y dirección definidas [42], [50]. Por último, las características de geometría engloban parámetros como la longitud o área de la llama, por lo que requieren una segmentación previa de la llama, a diferencia de las características de intensidad y textura.

1.1.6. Interpretación de características de llama

La etapa final de los sistemas de visión es la transformación de las propiedades de imagen en variables relacionadas con la combustión. Las características visuales de las llamas se han utilizado para modelar velocidades de llama [51], [52] y parámetros asociados a la relación aire-combustible, como las ratios de aire primario, secundario y terciario [40], y la concentración de oxígeno [42]. Además, el bloque de interpretación también puede identificar condiciones de combustión complejas, definidas por la combinación de varios parámetros [53], [54].

Las técnicas convencionales de análisis de datos tienen dificultades con volúmenes elevados y relaciones complejas, como es el caso del modelado de la combustión a partir de imágenes. Una alternativa con un alto potencial para resolver este problema es el aprendizaje automático, que utiliza distintos algoritmos de modelado como los árboles de decisión [53], las máquinas de vectores soporte [40], [53], [54] y las redes neuronales artificiales [40], [53], [54]. Aparte de las imágenes de llama, los modelos de aprendizaje automático pueden usar información diversa del proceso de combustión, para por ejemplo optimizar la relación entre emisiones y eficiencia [55], o predecir el comportamiento dinámico [56], las emisiones [57], la viscosidad del combustible [58] o la temperatura del horno a largo plazo [59]. El aprendizaje automático se ha empleado como una herramienta transversal de modelado en campos de estudio muy diversos, como la agricultura [60], la vigilancia [61], la ingeniería bioquímica [62], [63], la transferencia de calor [64], los sistemas energéticos [65] y de control [66], y los motores de combustión [67]. En los métodos de aprendizaje automático predomina el aprendizaje supervisado, descrito a continuación utilizando la terminología de un estudio previo [68]. Esta técnica dispone de multitud de algoritmos para analizar los datos, proporcionando distintas alternativas de modelo (hipótesis) para un mismo conjunto de datos. Además, el comportamiento de los algoritmos se puede ajustar con varios parámetros, incrementado el número de opciones disponibles. Independientemente del algoritmo considerado, la tarea de aprendizaje se ejecuta como un proceso iterativo de optimización en el que diferentes modelos se evalúan según su error de predicción. Los métodos de aprendizaje automático buscan incrementar la capacidad de generalización de la hipótesis seleccionada, por lo su comportamiento se analiza ante datos no observados previamente. Para ello, el conjunto de datos previos se divide en varios grupos, realizando la optimización y evaluación del modelo con partes del conjunto diferentes.

1.2. Objetivos

El objetivo general de esta tesis es el desarrollo de un sistema de monitorización para la combustión de gas de alto horno, basado en la adquisición de imágenes en color y en su procesamiento con técnicas de inteligencia artificial. Este objetivo general se desglosa en varios objetivos específicos, definidos a continuación junto a su publicación asociada.

- Procesamiento y análisis de pruebas iniciales semiindustriales con diferentes relaciones aire-combustible (Artículo A), para realizar una evaluación preliminar de la viabilidad técnica de la tecnología.

- Configuración de una instalación de laboratorio para la combustión de varias mezclas de gas, con distinto poder calorífico y en condiciones seguras.

- Realización, procesamiento y análisis de las pruebas de laboratorio con diferentes relaciones aire-combustible (Artículo I), con el propósito de definir el procedimiento base de extracción de características para la escala semiindustrial.

- Ajuste y análisis de los modelos predictivos de laboratorio (Artículo II), proporcionando un escenario de referencia sobre el que preparar y evaluar la escala semiindustrial.

- Definición de requisitos, evaluación, selección y configuración del sistema de visión para la realización de las pruebas semiindustriales finales.

- Procesamiento y análisis de las pruebas semiindustriales finales con distintas relaciones aire-combustible (Artículo III), adaptando el desarrollo de laboratorio a esta escala.

- Ajuste y análisis de modelos predictivos semiindustriales (Artículo III) para su comparación con los resultados de laboratorio.

- Desarrollo de una aplicación informática para la monitorización en tiempo real, con el objetivo de integrar el desarrollo en los procesos de monitorización y control de ArcelorMittal.

- Validación del desarrollo del sistema de monitorización (Artículo IV), para proporcionar una evaluación final de su rendimiento y capacidad de adaptación ante distintos escenarios.

1.3. Unidad temática

Los artículos que constituyen la tesis proceden de la misma línea de investigación, centrada en la caracterización de la combustión de gas de alto horno mediante la captura de imágenes en color, así como su procesamiento utilizando métodos de inteligencia artificial. El trabajo de investigación incluye la realización de pruebas experimentales, procesamiento de datos, ajuste de modelos predictivos y análisis de resultados. Cada artículo describe un estudio diferente, caracterizado por unas actividades y condiciones concretas. A pesar de que el objetivo final del desarrollo es mejorar la monitorización en escala semiindustrial, también se ha realizado trabajo a escala de laboratorio. Estos ensayos tienen un consumo de combustible y coste asociado menor, lo que ha permitido hacer más pruebas para estudiar condiciones adicionales de combustión.

Los artículos estudian diferentes mezclas de combustible, definidas según el interés de la sustitución del gas natural por gas de alto horno, relacionado con el incremento de la eficiencia de la acería. El aumento de la proporción de gas de alto horno en la mezcla reduce el consumo de gas natural, pero también disminuye la temperatura de la combustión, por lo que el uso de gas de alto horno en la mezcla está limitado para procesos de alta temperatura. Esta tesis analiza la mezcla óptima de gas de alto horno (*Blast Furnace Gas*, BFG) con gas natural, BFG70, con 70 y 30 %v. respectivamente. Además, la investigación considera tres combustibles adicionales como referencia: BFG0 (100 %v. gas natural), BFG80 (80 %v. gas de alto horno y 20 %v. gas natural) y BFG100 (100 %v. gas de alto horno).

El **Artículo A** describe la realización, procesamiento y análisis de las pruebas iniciales a escala semiindustrial. Este trabajo presenta el horno, la cámara de color y el procesamiento de imágenes de llama según sus características de intensidad. A partir de los resultados se estudia la relación entre las propiedades visuales calculadas, las mezclas de combustible y las relaciones aire-combustible, caracterizadas según el exceso de aire y concentración y de oxígeno en gases de salida.

El **Artículo I** se centra en la realización, procesamiento y análisis de las pruebas de laboratorio. La instalación experimental se describe en detalle, incluyendo la cámara de combustión, quemador, líneas de combustible y aire, cámara de color, equipos de medida adicionales y mezclas de combustible. Se definen los ensayos, combinaciones de combustible y exceso de aire, métodos experimentales, configuración de la cámara de color y procesamiento de sus imágenes. En esta última actividad se incluyen las transformaciones aplicadas a las imágenes de llama, así como la extracción de características visuales relacionadas con la intensidad, textura y geometría. Los resultados del Artículo I se engloban en el estudio de la combustión del gas de alto horno a escala de laboratorio, analizando el efecto del exceso de aire sobre las emisiones contaminantes y las características de la imagen. Debido a que la instalación de laboratorio facilita la monitorización de la combustión con varios equipos ópticos a la vez, y para caracterizar con mayor profundidad las propiedades de las llamas, el Artículo I incluye el uso de un espectrómetro y una cámara del rango ultravioleta-visible, así como el procesamiento de sus datos. Dicho trabajo complementa a los objetivos de la tesis, con la caracterización de la combustión de gas de alto horno mediante dos técnicas ópticas adicionales.

La línea de investigación continua con el **Artículo II** y su ajuste y análisis de modelos predictivos a escala de laboratorio. Estos modelos se desarrollan a partir de las imágenes de color y datos capturados en la campaña experimental a escala de laboratorio (Artículo I). En particular, se estudia el modelado del exceso de aire a partir de características de imagen. El procesamiento de imágenes del trabajo anterior se expande con la extracción de características visuales adicionales. Para el desarrollo de los modelos predictivos, se define un método de aprendizaje automático, que define la estandarización de los datos, la selección de características de imagen, los algoritmos de aprendizaje, la optimización de hiperparámetros, las métricas de rendimiento y la evaluación de los modelos. Los resultados de este trabajo analizan la variación estadística de las características de imagen respecto al exceso de aire, y también la precisión de los modelos al variar el combustible, el exceso de aire, el algoritmo de aprendizaje automático y las muestras de entrenamiento y validación.

Tras haber estudiado en detalle la caracterización de la combustión en laboratorio, el trabajo continúa con su análisis a escala semiindustrial. En este sentido, el **Artículo III** integra el procesamiento y análisis de las pruebas semiindustriales finales, con distintas concentraciones de oxígeno en los gases de salida, así como el ajuste y análisis de los modelos predictivos para esta escala. Este trabajo detalla la instalación experimental, describiendo el horno, el quemador, el sistema de visión, los equipos de medida complementarios y los combustibles. Se recogen también los métodos para la operación del horno, las condiciones de ensayo, el procesamiento de imágenes y el método de modelado. El Artículo III adapta el procesamiento de imágenes de los Artículo I y II para la escala semiindustrial, y evalúa el comportamiento de los modelos predictivos del Artículo II en esta nueva configuración. A diferencia del Artículo A, el Artículo III utiliza un sistema de visión industrial instalado en el interior del horno, amplía las condiciones de operación estudiadas, y añade la extracción de características de textura y el entrenamiento de modelos predictivos. Los resultados del artículo incluyen el análisis de las imágenes capturadas en la escala semiindustrial y el estudio de la dependencia estadística de las características de imagen con la concentración de oxígeno en los gases de salida. También se compara la precisión de los modelos según las condiciones de operación, el combustible empleado, la concentración de oxígeno en los gases de salida, el algoritmo de aprendizaje automático, y el uso de muestras no observadas previamente.

Una vez concluido el trabajo a escala de laboratorio y semiindustrial, la línea de investigación se completa con el Artículo IV, en el que se analiza la adaptabilidad del sistema de monitorización a lo largo del desarrollo. El método de estudio se basa en la identificación de los distintos escenarios en los que se ha desarrollado el sistema, caracterizados por el tipo de quemador y la posición de cámara, por ejemplo. Los resultados recogen el efecto de estos cambios sobre las imágenes capturadas, su procesamiento y los modelos predictivos. De esta manera, se evalúa la adaptabilidad del sistema ante los distintos escenarios del desarrollo.

Según lo expuesto anteriormente, los cuatro artículos que componen esta tesis siguen una línea de investigación con una clara unidad temática. Por lo tanto, se cumple el requisito para la presentación de la tesis como compendio de publicaciones, definido en el Reglamento sobre Tesis Doctorales de la Universidad de Zaragoza (aprobado el 25 de junio de 2020 por el Consejo de Gobierno de la Universidad).

1.4. Trabajos realizados

1.4.1. Procedimiento experimental y métodos

En este apartado se describen los materiales y métodos empleados en el trabajo de investigación, que se realiza de forma secuencial en dos escalas diferentes: laboratorio y semiindustrial. Para cada una de las escalas se define la instalación experimental, las pruebas y el procesamiento de imágenes, que incluye el ajuste de modelos predictivos. En primer lugar, se realizan unas pruebas iniciales a escala semiindustrial como punto de partida para la investigación, para después continuar con una campaña extensiva en entorno de laboratorio, y finalizar con las pruebas definitivas en escala semiindustrial. Para facilitar su comprensión, la descripción de los ensayos se estructura en bloques según su escala (laboratorio y semiindustrial). En esta sección de métodos también se incluye la técnica para evaluar todo el desarrollo del sistema de monitorización.

Como comentario general, la tesis tiene como objetivo final promover la valorización del gas de alto horno en la industria, donde la modificación de los quemadores comerciales es limitada. Por lo tanto, los métodos se han definido para reproducir esas condiciones industriales a escala de laboratorio y semiindustrial, reduciendo las barreras para implementar las técnicas estudiadas en escala industrial. Las implicaciones de este criterio sobre las pruebas realizadas se describen en detalle en los siguientes apartados.

1.4.1.1. Escala de laboratorio

Parte del estudio se realizó en la instalación experimental de CIRCE Centro Tecnológico (Zaragoza). Dicha instalación cuenta con una cámara de combustión que permite la monitorización y la adquisición de imágenes de llama. Un esquema de dicho laboratorio se muestra en la Figura 6.

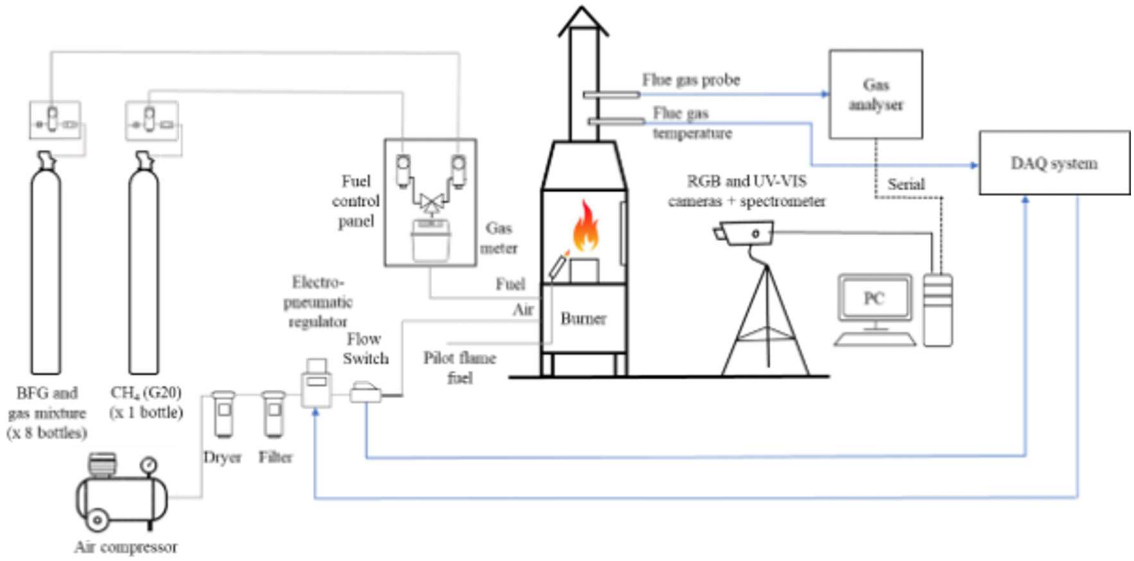

Figura 6. Esquema de la instalación experimental de combustión a escala de laboratorio.

La cámara de combustión está equipada con un quemador de premezcla para combustible gaseoso de 20 kW_t. El quemador posee dos entradas de un diámetro de 25 y 10 mm, por donde se inyecta el combustible y aire, respectivamente (Figura 7). El diseño del quemador permite el montaje de distintos cabezales para optimizar las condiciones de operación. Los cabezales tienen un diámetro de 100 mm y una matriz de orificios por la que sale la mezcla de combustible-aire. El diámetro de los orificios varía según el cabezal (1, 5 y 10 mm), lo que modifica la velocidad de la mezcla aire-combustible, la estabilidad de la llama y su distribución sobre el quemador (Figura 8). Para reproducir condiciones industriales, este estudio utiliza en todas las pruebas el mismo cabezal, de 5 mm de diámetro de orificios, seleccionado para proporcionar la mayor estabilidad de llama y distribución más uniforme para el gas de alto horno, además de permitir la operación con metano.

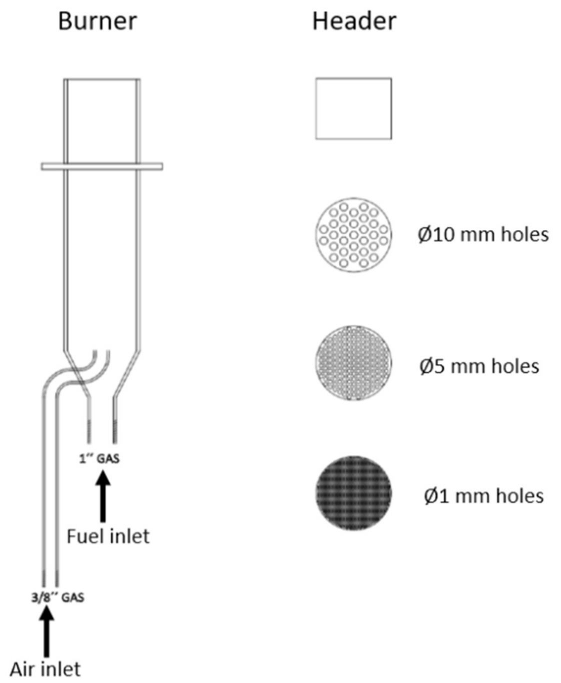

Figura 7. Esquema del quemador de premezcla para combustible gaseoso.

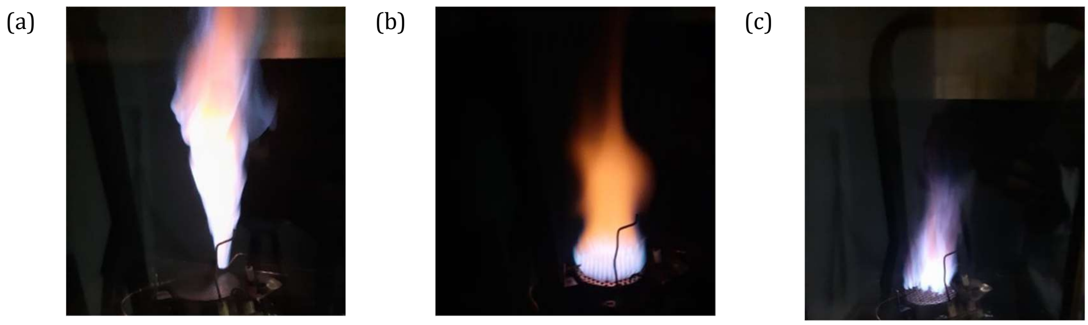

Figura 8. Tipos de llamas obtenidas con los cabezales de (a) 1, (b) 5 y (c) 10 mm, para el combustible BFG100 y una potencia de 4 kW_t en condiciones subestequiométricas.

La cámara de combustión está sellada y tiene una base cuadrada de 65 cm de anchura y profundidad, y una altura de 90 cm. Dos de sus paredes cuentan con ventanas de inspección de cristal y cuarzo, que permiten la transmisión de energía en los rangos visible y ultravioleta-visible, respectivamente (Figura 9). Para quemar restos de combustible de operaciones previas e incrementar la seguridad de la instalación, la combustión se inicia con una llama piloto de butano de 2 kW_t de potencia.

(a)

(b)

Figura 9. Ventanas de inspección de cristal (a) y cuarzo (b) de la cámara de combustión.

El quemador está conectado a dos líneas independientes de gas, lo que permite utilizar un combustible diferente en cada una, reduciendo así el tiempo de preparación cuando se cambia de combustible. El laboratorio también incluye un caudalímetro volumétrico para medir el consumo de gas, y un sistema de seguridad para interrumpir la alimentación de combustible ante la detección de fugas.

Cada línea de gas se alimenta con botellas de combustible proporcionadas por un distribuidor de gas, cuyo consumo depende del poder calorífico del gas y de la potencia de las pruebas. A una potencia constante, el uso de un combustible con menor poder calorífico requiere más botellas, pudiendo necesitar su reemplazo en mitad de los ensayos. Para reducir el tiempo de preparación asociado, una línea está conectada a un grupo de ocho botellas, mientras que la otra línea se alimenta con una única botella, proporcionando una configuración más eficiente para combustible con un mayor poder calorífico. En este estudio, la línea de una botella se utiliza para el metano, mientras que la otra se usa con gas de alto horno y su mezcla con metano.

El aire de combustión se inyecta en el quemador a través de otra línea, alimentada por un compresor. La presión del aire se controla con un regulador electroneumático SMC ITV2000, lo que permite regular el caudal de aire, que es a su vez medido por un caudalímetro IFM SD6000. Este sensor tiene una repetibilidad de ± 1.5 % y una precisión de ± (3 % de lectura + 0.3 % de escala completa). La comunicación con estos equipos se gestiona mediante un ordenador a través de un sistema de adquisición de datos, que también incluye un termopar para la medida de la temperatura del gas de combustión en la chimenea.

La composición de los gases de combustión se mide con dos analizadores de gases situados en dos puntos de la instalación. La medida principal se realiza en el conducto vertical de evacuación de humos con el modelo MRU Vario Plus Industrial, analizando las concentraciones de O_2, CO, CO_2, NO_x y CH_4 (Tabla 2). El segundo analizador de gases (MRU

Optima 7) proporciona una medida de apoyo en la cámara de combustión, utilizada para determinar la estabilidad de los gases de combustión.

Tabla 2. Especificaciones del analizador de gases MRU Vario Plus Industrial.

Gas	Principio de medida	Rango	Precisión
O_2	Electroquímico	0 – 21.0 %v.	± 0.2 %v. abs.
CH_4	Infrarrojo no dispersivo	0 – 10000 ppm	± 60 ppm o 5 % de lectura
CO	Infrarrojo no dispersivo	0 – 10000 ppm	± 40 ppm o 5 % de lectura
CO_2	Infrarrojo no dispersivo	0 – 30 %v.	± 0.5 %v. o 3 % de lectura
NO	Electroquímico	0 – 1000 ppm (hasta 5000 ppm)	± 5 ppm o 5 % de lectura ≤ 1000 ppm
			10 % de lectura > 1000 ppm
NO_2	Electroquímico	0 – 200 ppm (hasta 1000 ppm)	± 5 ppm o 5 % de lectura ≤ 200 ppm
			10 % de lectura > 200 ppm

La instrumentación de la instalación experimental se completa con tres equipos ópticos: un espectrómetro (Ocean Optics Flame-S Miniature, 2048 píxeles), una cámara ultravioleta-visible (Raptor Photonics Falcon Blue, 1.0 megapíxel), y una cámara de color (The Imaging Source DFK 33GX174, 2.3 megapíxeles). La cámara ultravioleta-visible se equipa con un filtro de paso (ASAHI) para la banda 310 ± 10 nm, asociada a la emisión del radical OH en estudios de quimioluminiscencia de llama [21]-[26]. El análisis de las imágenes ultravioleta-visible y los espectros de emisión de llama complementa el objetivo principal de la tesis, centrado en el estudio de las imágenes de color.

A escala de laboratorio se estudiaron tres mezclas de combustible: BFG70, BFG100 y BFG0. A diferencia de la escala semiindustrial, para las mezclas se usó metano en lugar de gas natural, cuyo suministro en botellas es más económico. La composición y poder calorífico de las mezclas empleadas en laboratorio se muestra en la Tabla 3.

Tabla 3. Composición y poder calorífico de las mezclas de combustible utilizadas en laboratorio.

Mezcla de combustible	BFG0	BFG70	BFG100
[CH_4] (%v.)	100	28	-
[H_2] (%v.)	-	3	4
[CO] (%v.)	-	16	22
[CO_2] (%v.)	-	16	22
[N_2] (%v.)	-	37	52
PCI (MJ/m^3N)	36	13	4

La campaña experimental se realizó a una potencia fija de 5.5 kW_t, ajustando el caudal de combustible para cada mezcla y modificando el caudal de aire para estudiar todo el rango de operación del quemador. De esta manera, se estudiaron condiciones de operación ineficientes, cuya monitorización es de interés para la industria. El rango de operación se definió para cada mezcla de combustible según los límites de estabilidad de su llama. El aumento del caudal de aire incrementa la velocidad de la mezcla aire-combustible, aumentando su inestabilidad y provocando que la llama se despegue de la base del quemador y se extinga en condiciones extremas. A su vez, una reducción excesiva del caudal de aire causa el retroceso de la llama a la cámara de mezcla del quemador.

Cada punto de operación se caracterizó calculando su exceso de aire, definido como la proporción entre la relación másica aire-combustible del punto de operación y la estequiométrica. Por lo tanto, un exceso de aire superior a 1.0 se relaciona con combustión rica en aire y pobre en combustible.

Dado que cada mezcla de combustible tiene un poder calorífico diferente, cada una de ellas necesita un caudal distinto para obtener la misma potencia. Al variar el caudal, también se modifica la velocidad de la mezcla aire-combustible en el quemador, lo que a su vez condiciona los puntos de operación de cada combustible. La velocidad de la mezcla se puede alterar utilizando cabezales con distinta sección de paso, pero la modificación de los quemadores comerciales utilizados en la industria es limitada. Dado que este estudio busca reproducir esta característica industrial en el laboratorio, se utilizó el mismo cabezal y área de paso para todos los combustibles. Como resultado, se obtuvo un rango de exceso de aire diferente para cada mezcla de combustible, con los que se realizaron tres Series de Ensayos (SE, Tabla 4). Los intervalos de Exceso de Aire (EA) fueron [1.41, 2.01], [1.13, 1.91] y [0.91, 1.24], para las mezclas de combustible BFG0, BFG70 y BFG100, respectivamente.

Tabla 4. Puntos de operación de las mezclas de combustible en las pruebas de laboratorio.

Serie de ensayos	SE1	SE2	SE3
Mezcla de combustible	BFG0	BFG70	BFG100
EA_1	1.41	1.13	0.91
EA_2	1.43	1.27	0.94
EA_3	1.51	1.37	1.09
EA_4	1.64	1.41	1.11
EA_5	1.76	1.57	1.24
EA_6	1.88	1.67	-
EA_7	2.01	1.78	-
EA_8	-	1.91	-

La campaña experimental incluyó 20 pruebas, divididas en tres series de ensayos (una por cada mezcla de combustible). En todas ellas, la cámara de color se situó delante de la ventana de cristal, y la cámara ultravioleta-visible y el espectrómetro enfrente de la de cuarzo. De esta manera, los tres equipos ópticos obtenían datos simultáneamente. Al comienzo de cada serie, el quemador se precalentaba durante una hora para alcanzar temperaturas estables, y después, se ajustaban las condiciones para el primer punto de operación, siguiendo el mismo procedimiento para el resto. En primer lugar, se fijaban los caudales de combustible y aire, y luego se monitorizaba la composición de los gases en la cámara de combustión y chimenea. Cuando la composición era similar en ambos puntos, se consideraba que se alcanzaban las condiciones estacionarias, y se comenzaba a capturar las imágenes y los espectros durante 6 minutos. Finalmente, para cada punto de operación se promediaban los caudales de combustible y aire, así como la composición de los gases de combustión.

Para obtener medidas ópticas comparables entre los distintos ensayos, la configuración de los equipos ópticos se mantuvo constante durante toda la campaña. Los parámetros de estos sensores se ajustan según la radiación de la escena, cuya medida incrementa con el tiempo de exposición de las cámaras y el tiempo de integración del espectrómetro. La estrategia de configuración busca medir señales con una intensidad elevada, pero inferior al valor máximo que puede cuantificar el sensor. Si este límite superior se alcanza, los píxeles del sensor se saturan y se pierde información sobre la radiación. En este trabajo se realizaron pruebas preliminares para estudiar distintas configuraciones de adquisición y elegir aquella que proporcionase la mayor intensidad de señal sin llegar a saturar. Para ello, se analizaron imágenes utilizando los mapas de calor e histogramas de sus valores promedios. A modo de ejemplo, la Figura 10 muestra los resultados para las imágenes ultravioleta-visible.

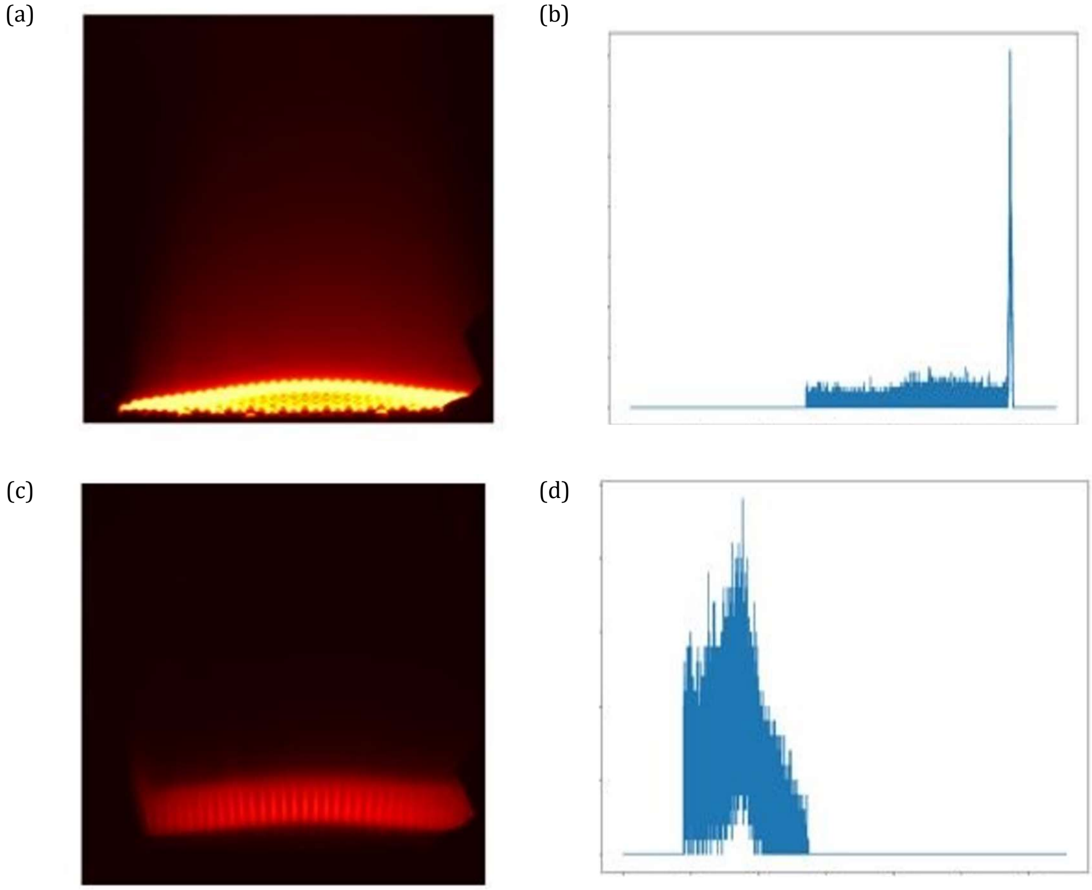

Figura 10. Mapas de calor e histogramas de la cámara ultravioleta-visible para la mezcla BFG0 (a, b) y BFG100 (c, d).

Por cada imagen de color, se obtuvieron tres imágenes monocromas, una por canal de color (rojo, verde y azul), mientras que en el caso de la cámara ultravioleta-visible sólo se capturó una imagen monocroma por disparo. Todas las imágenes monocromas recibieron un procesamiento similar, en el que primero se segmentaron los píxeles de llama según un umbral, calculado con el método de Otsu [37], [69]. Este procedimiento estudia distintos valores de umbral para agrupar los píxeles de la imagen: los píxeles con una intensidad inferior al umbral se asignan a una clase, y el resto a la otra. Para cada umbral, se calcula la varianza entre las dos agrupaciones de píxeles, y se elige el valor que maximiza dicha dispersión.

Tras segmentar la llama, se extrajeron sus características de intensidad, textura y geometría, obteniéndose un total de 66 características para las imágenes de color. Por cada canal de color, se calcularon 22 propiedades: cuatro de intensidad (media [37] - [41], desviación estándar [37]-[39], [41], asimetría [39], [41] y curtosis [39]), 13 de textura (seleccionadas del trabajo de Haralick et al. [70], y utilizadas en [40]), y cinco de geometría (área [37], [38], [71], abscisa y ordenada del centroide [71], [72], anchura [71] y altura [37], [71]). Debido al carácter complementario de las imágenes ultravioleta-visible en esta investigación, sólo se calcularon para ellas cuatro de las 22 características previas. Estas propiedades incluyen una de intensidad (media), otra de textura (medida de información de la correlación I) y dos de geometría (área y ordenada).

Las características geométricas pueden alterarse significativamente debido a pequeños errores de clasificación en la segmentación. Por ejemplo, si una llama tiene una altura de 5 cm, y un píxel elevado 15 cm sobre ella se clasifica como llama, el método de cálculo visual de la altura de la llama obtendrá un valor equivalente a 20 cm. Para evitar este efecto, se descartaron los píxeles de llama cuyos píxeles adyacentes no eran de llama, utilizando una transformación morfológica de erosión con una máscara de 3x3 píxeles [73].

Para cada una de las tres mezclas de combustible, se entrenaron y evaluaron varios modelos predictivos para identificar el exceso de aire asociado a cada imagen de color, según sus 66 características extraídas. Con ese objetivo, se empleó el mismo método de aprendizaje automático para todas las mezclas de combustible. Primero se dividieron todas las imágenes de una mezcla de combustible en dos grupos: entrenamiento y prueba. El grupo de entrenamiento se usó para (1) seleccionar el subgrupo de características con una mayor relación con el exceso de aire, (2) ajustar hiperparámetros de los algoritmos de aprendizaje automático, y (3) evaluar el rendimiento de las distintas opciones. En concreto, se estudiaron tres algoritmos: la regresión logística (*Logistic Regression*, LR) [53], [54], las máquinas de vectores soporte (SVM) [40], [53], [54] y las redes neuronales artificiales [40], [53], [54]. En este último caso, se escogió la tipología de perceptrón multicapa (*MultiLayer Perceptron*, MLP). El comportamiento de estos algoritmos se caracteriza por el ajuste de un modelo probabilístico a partir de funciones logísticas (LR), la definición del hiperplano que maximiza el margen entre las clases (SVM), o el entrenamiento de una red neuronal prealimentada a partir de la propagación hacia atrás de errores (MLP). Tras comparar la precisión de cada algoritmo, la alternativa que proporcionó los mejores resultados se evaluó una vez más con los datos del grupo de prueba.

De las 66 características calculadas, sólo se utilizaron las diez con una mayor varianza respecto a las clases de exceso de aire de cada combustible. El ajuste de hiperparámetros y la evaluación del rendimiento en el entrenamiento se realizó a partir de validaciones cruzadas, basadas en el entrenamiento y validación de un modelo con distintos subgrupos de datos para obtener una medida de evaluación más robusta. No obstante, la validación cruzada puede proporcionar resultados con un sesgo optimista si se usa a la vez para ajustar hiperparámetros y evaluar el rendimiento de los modelos [74], [75]. A pesar de ello, si los modelos se ordenan según su precisión, el resultado es generalmente el mismo con validación cruzada sin anidar o anidada [76]. Para obtener una medida más realista del rendimiento de los modelos, en este trabajo se utilizó una validación cruzada anidada con dos bucles. El bucle exterior de la validación anidada dividió el grupo de entrenamiento en diez pares de subgrupos de entrenamiento y validación, a partir de los cuales se promedió la precisión de cada algoritmo de aprendizaje automático. En el bucle interior, cada subgrupo de entrenamiento se dividió en cinco nuevas particiones de entrenamiento y validación, para escoger los hiperparámetros con una mayor precisión promedio. El rendimiento de los modelos predictivos se evaluó adicionalmente a través del cálculo de sus matrices de confusión y curvas de aprendizaje.

El lenguaje de programación Python (versión 3.7) se utilizó para procesar las imágenes y estudiar los modelos predictivos, usando las librerías de OpenCV, Scikit-learn, NumPy, SciPy, Mahotas y Pandas.

1.4.1.2. Escala semiindustrial

Parte de la campaña experimental se realizó en una instalación experimental de la planta de ArcelorMittal Asturias (Avilés), equipada con un horno semiindustrial (Figura 11).

(a) (b)

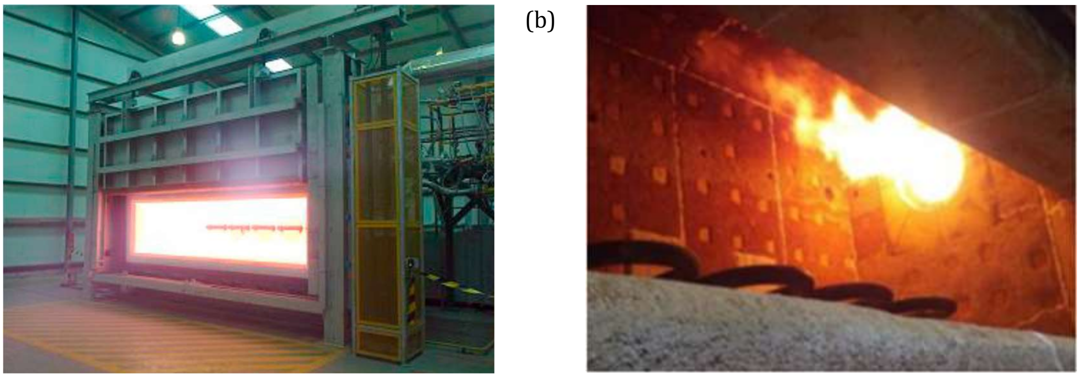

Figura 11. Horno utilizado en los ensayos a escala semiindustrial [77].

El horno tiene una cámara de combustión de 4.6 m de largo, 1.5 m de anchura y 2.8 de altura, y su configuración se puede modificar para probar distintos combustibles y condiciones de operación. Un circuito de agua con seis lanzas semicirculares simula la transferencia de calor de un horno industrial a una lámina de acero: el caudal de agua se calienta en el interior del horno, se enfría a la salida mediante un refrigerador, y se introduce de nuevo en la cámara de combustión. Un sistema de control y adquisición de datos registra el caudal, la temperatura, la presión, la concentración de oxígeno ($[O_2]_{fg}$) y las emisiones de gases contaminantes (CO, NO_x, SO_2 y CO_2) en los gases de salida. La temperatura de la cámara de combustión (T_{cc}) se promedia a partir de las medidas de cinco termopares distribuidos en distintos puntos del horno.

En las primeras pruebas semiindustriales se utilizó un quemador de difusión de 1.2 MW_t y una cámara de color (The Imaging Source DFK 33GX174, 2.3 megapíxeles), situada en el exterior del horno y alineada con una ventana de inspección enfrente del quemador. El quemador usado en estas pruebas se cambió para las pruebas finales, debido a las necesidades de ArcelorMittal de implementar un nuevo modelo en sus procesos productivos. Este modelo mantiene la tipología de difusión y la potencia de 1.2 MW_t, y además incluye una lanza central y dos laterales de combustible, así como varias entradas de aire (Figura 12).

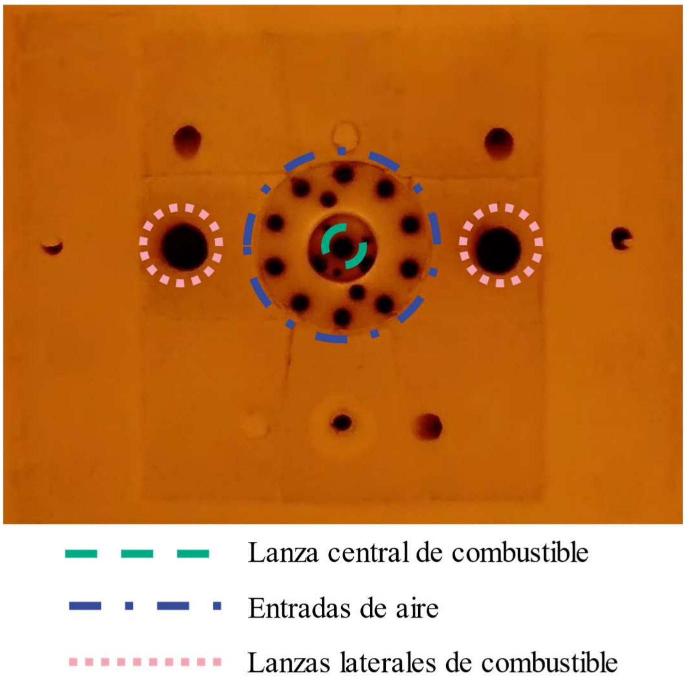

Figura 12. Quemador de difusión utilizado en las pruebas finales en escala semiindustrial.

Las pruebas experimentales utilizaron distintas mezclas de gas de alto horno, extraído y filtrado en la misma instalación. Debido a ello, la composición de las mezclas es variable y depende de la operación del alto horno. La composición y el poder calorífico típicos de las mezclas de combustible a escala semiindustrial se muestran en la Tabla 5.

Tabla 5. Composición y poder calorífico típicos de las mezclas de combustible utilizadas en escala semiindustrial.

Mezcla de combustible	BFG0	BFG70	BFG80	BFG100
[CH_4] (%v.)	92	28	18	-
[C_2H_6] (%v.)	8	2	2	-
[H_2] (%v.)	-	3	3	4
[CO] (%v.)	-	16	18	22
[CO_2] (%v.)	-	15	18	22
[N_2] (%v.)	-	34	39	49
[H_2O] (%v.)	-	1	1	2
[O_2] (%v.)	-	1	1	1
PCI (MJ/m^3N)	38	14	11	4

Las primeras pruebas semiindustriales se centraron en la combustión de las mezclas de BFG0, BFG70 y BFG100, para valores de $[O_2]_{fg}$ entre 0 y 5 %v. Para reducir las emisiones de BFG0, se suministró oxígeno como comburente, operando parcialmente en régimen de oxicombustión. En todos los ensayos, el aire de combustión se precalentaba a 500 °C. La Tabla 6 recoge las condiciones de operación para las pruebas iniciales a escala semiindustrial.

Tabla 6. Puntos de operación de las pruebas iniciales a escala semiindustrial.

Serie de ensayos	SE1	SE2	SE3
Mezcla de combustible	BFG0	BFG70	BFG100
Modo de operación	Oxicombustión parcial	Estándar	Estándar
$[O_2]_{fg,1}$ (%v.)	0.0	0.0	0.0
$[O_2]_{fg,2}$ (%v.)	1.0	1.5	1.0
$[O_2]_{fg,3}$ (%v.)	3.5	5.0	3.0

Para cada imagen de color, se obtuvieron tres imágenes monocromas, una por canal de color (rojo, verde y azul). De cada canal de color se extrajeron cuatro características de intensidad (media [37] - [41], desviación estándar [37]-[39], [41], asimetría [39], [41] y curtosis [39]), obteniendo 12 propiedades por imagen de color.

Después de estas primeras pruebas semiindustriales, se realizó la campaña de laboratorio, para luego finalizar el estudio con ensayos adicionales a escala semiindustrial. A diferencia de los ensayos iniciales en escala semiindustrial, la segunda campaña usó un sistema de visión diferente. Este cambio se debe que el desarrollo continuó con la ingeniería, compra e instalación de un sistema de visión industrial en el horno, mejorando la posición de la cámara y permitiendo una operación continua en un entorno industrial. En primer lugar, se evaluaron distintas alternativas para la colocación del sistema: montaje interior o exterior, ventana de inspección superior o inferior, y alineación con el quemador (Figura 13). Considerando las distintas opciones, se definieron los requisitos específicos para el diámetro de la sonda, la distancia de trabajo y el campo de visión de la lente, y se contactó con once proveedores para estudiar un total de 20 propuestas de sistema. Aparte del cumplimiento de los requisitos, se analizaron distintas características de cada oferta, tales como la resolución y tamaño del sensor, la refrigeración del sistema y el coste económico. Además, la perspectiva del horno capturada por los sistemas de visión se simuló definiendo la escena y la cámara con el programa SKETCHUP (Figura 14).

(a)

(b)

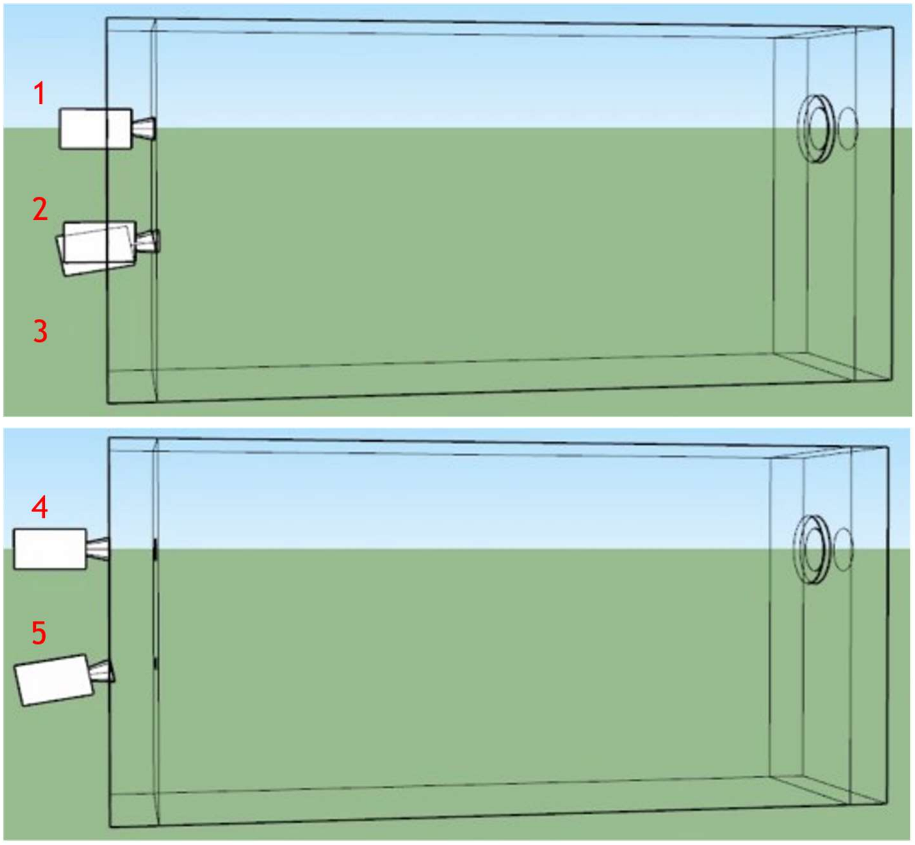

Figura 13. Posiciones de la cámara para un montaje (a) interior y (b) exterior, ilustradas con el programa SKETCHUP.

(a)

(b)

(c)

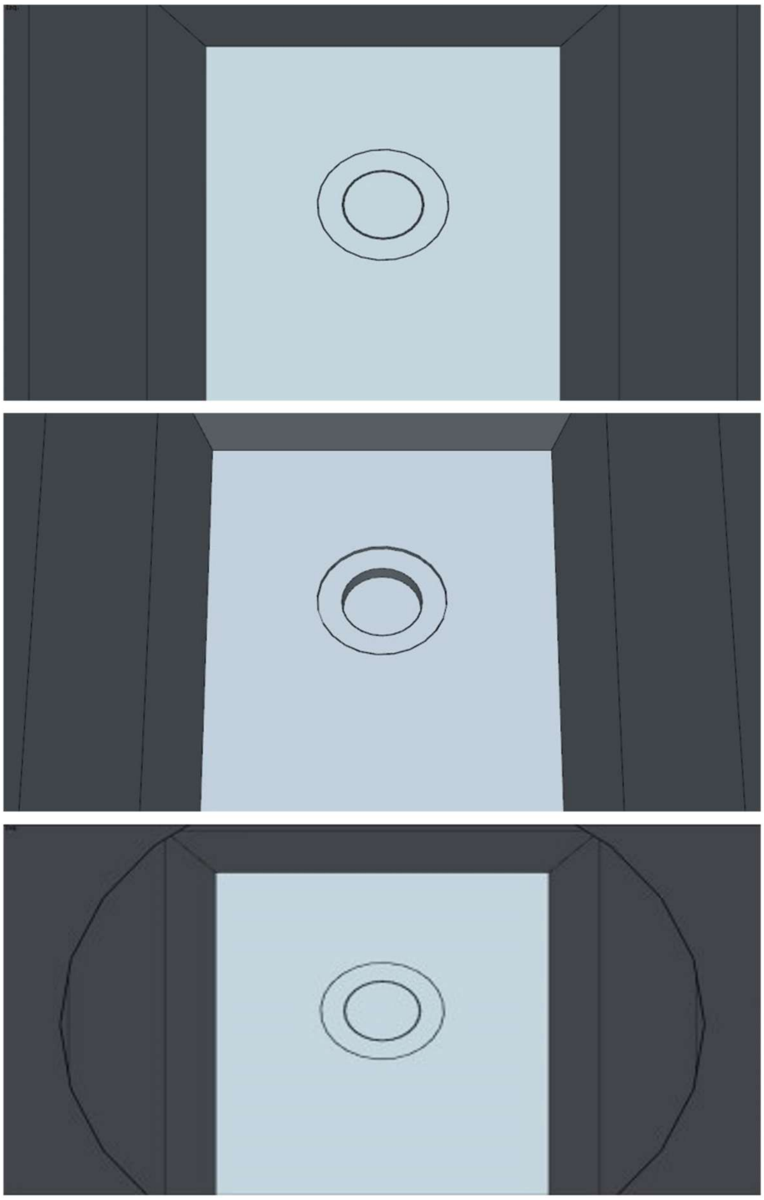

Figura 14. Ejemplos de simulaciones de perspectiva para los siguientes casos: montaje interior en (a) ventana superior y (b) ventana inferior con orientación hacia quemador, y (c) montaje exterior en ventana superior.

Finalmente, el sistema de visión seleccionado como mejor alternativa incluía una cámara de color (BASLER BIP2-1920c, 2.1 megapíxeles), protegida por una carcasa metálica refrigerada con agua y un dispositivo retráctil (SOBOTTA). La cámara y su carcasa se introducen en el interior del horno, y en caso de temperaturas peligrosas o fallo del sistema, el equipo se extrae mediante el dispositivo retráctil. Este sistema se escogió porque proporcionaba la mejor combinación de campo de visión y protección ante llamas.

En los ensayos semiindustriales finales se utilizó una potencia constante de 920 kW_t. Para cada mezcla, el caudal de combustible se mantuvo constante, y el de aire se modificó para obtener los distintos valores de exceso de aire. El aire de combustión se introducía precalentado a una temperatura de 485 °C, con una concentración de oxígeno de 21 %v. La combustión de las mezclas se estudió para los valores de concentración de oxígeno en gases de salida de 0, 1 y 5 %v. El combustible se introdujo por la lanza central del quemador para las mezclas de BFG0 y BFG70, mientras que para mejorar la operación con BFG80, el combustible se inyectó por las lanzas centrales y laterales. De esta manera, los reactivos se diluyen con los productos de la combustión, operando en modo *sin llama,* también conocido como dilución moderada o intensa con bajo contenido en oxígeno *(Moderate or Intense Low Oxygen Dilution,* MILD) [78], [79]. En estas condiciones, la zona de reacción se distribuye a lo largo de todo el horno, favoreciendo la reducción de temperaturas de llama pico y las emisiones de NO_x [78], [80]. A pesar de referirse a estas condiciones como *sin llama*, el ojo humano puede observar la llama en algunos casos [80]-[82], aunque con una visibilidad inferior a la de la llama de otros combustibles convencionales.

El procedimiento utilizado para la realización de las pruebas se describe a continuación. En primer lugar, el horno se precalentó para alcanzar condiciones estables de emisiones y temperatura. Debido a las dimensiones del horno, la concentración de los gases de combustión se estabiliza a la media hora, y la temperatura a las 8 horas. Tras alcanzar el régimen estacionario, se adquirieron imágenes de llama durante 10 minutos, para cada una de las mezclas de combustible. Además, también se estudiaron las condiciones transitorias para la mezcla de BFG70 a partir de la grabación de las imágenes después de la estabilización de las emisiones, aunque la temperatura no hubiese alcanzado su valor estacionario. De esta manera se analizaron las imágenes obtenidas para concentraciones de O_2 en gases de salida de 1, 2, 3, 4 y 5 %v. La Tabla 7 resume las características de los ensayos en la campaña.

Tabla 7. Puntos de operación de las mezclas de combustible para escala semiindustrial.

Serie de ensayos	SE1	SE2	SE3	SE4
Régimen	Estacionario	Estacionario	Estacionario	Transitorio
Mezcla de combustible	BFG0	BFG70	BFG80	BFG70
Modo de operación	Estándar	Estándar	Sin llama	Estándar
$[O_2]_{fg,1}$ (%v.)	0	0	0	1
$[O_2]_{fg,2}$ (%v.)	1	1	1	2
$[O_2]_{fg,3}$ (%v.)	5	5	5	3
$[O_2]_{fg,4}$ (%v.)	-	-	-	4
$[O_2]_{fg,5}$ (%v.)	-	-	-	5

De manera análoga a los ensayos de laboratorio, los parámetros de adquisición de la cámara se definieron según unos ensayos previos, y se mantuvieron constantes en toda la campaña. Los métodos de procesamiento de imágenes de llama en escala semiindustrial se basaron parcialmente en los de las imágenes de color para laboratorio, como se describe a continuación.

Mediante una inspección preliminar de la operación del horno, se observó que las imágenes de llamas eran significativamente diferentes a las de laboratorio. Las imágenes semiindustriales incluían elementos adicionales a la llama, como el quemador y las paredes del horno, que además tenían un color muy similar a las llamas. En contraposición, las llamas de laboratorio se mostraban sobre un fondo negro, lo que facilitaba su segmentación. En este sentido, incluso el ojo humano tenía problemas para identificar las llamas semiindustriales en las imágenes, por lo que la evaluación manual de la precisión de una segmentación automática presentaba dificultades. Ante el riesgo de hacer una clasificación imprecisa de los píxeles de llama, la etapa de procesamiento de imágenes no incluyó la operación de segmentación.

Esta decisión de diseño afecta a la fase posterior de extracción de características. En primer lugar, el cálculo de las propiedades de geometría requiere de la segmentación de la llama, ya que, por ejemplo, no se puede obtener la anchura de la llama si no se identifican los píxeles de llama. Por lo tanto, las características de geometría no se extrajeron en escala semiindustrial, y sólo se utilizaron las 51 propiedades de intensidad y textura. En segundo lugar, debido a que no se identifican píxeles de llama, las características de imagen se extraen de todos los píxeles en la imagen.

Los modelos predictivos para llamas semiindustriales se ajustan para estimar la concentración de oxígeno en gases de combustión, una variable diferente al exceso de aire estudiado en laboratorio. Aparte de entrenar los modelos para tres mezclas de combustible distintas, se analiza el comportamiento de una de ellas (BFG70) en condiciones transitorias. Para el entrenamiento y evaluación de cada uno de los cuatro modelos predictivos, se utilizó el procedimiento de laboratorio.

Por último, a diferencia de la escala de laboratorio, se desarrolló un programa informático para permitir el uso de los modelos predictivos en tiempo real por operarios de la acería. Esta aplicación utiliza los modelos entrenados para analizar las imágenes de una carpeta, mostrando los resultados en pantalla con una interfaz, en la que se observa la última imagen analizada y la gráfica con las predicciones de las 100 imágenes previas.

1.4.1.3. Validación del desarrollo del sistema de monitorización

Cómo último paso, el sistema de monitorización se validó analizando los resultados obtenidos en las distintas fases de desarrollo de forma conjunta. Este estudio se centró en la identificación de los cambios en condiciones de operación durante el desarrollo, y en evaluar su efecto sobre el sistema de monitorización. Para ello, se analizaron las imágenes de llama, la correlación entre las características de imagen y las condiciones de combustión, y la precisión de los modelos predictivos.

1.4.2. Análisis de resultados

En esta sección se presentan y analizan los resultados obtenidos. De forma similar al apartado del procedimiento experimental y métodos, se describe primero la escala de laboratorio (Artículos I y II) y luego la semiindustrial (Artículos A y III). En cada una de las escalas se analizan las imágenes de llama y la relación de las características extraídas con las condiciones de combustión, así como la precisión de los modelos predictivos ajustados.

En los resultados de escala de laboratorio, se incluye tanto el estudio de las emisiones del quemador experimental de las pruebas como el análisis de los espectros de quimioluminiscencia y las imágenes ultravioleta-visible. Dichos trabajos son complementarios a la línea de investigación de la tesis, centrada en el procesamiento de imágenes de color para la monitorización de la combustión. Por último, tras los resultados de la escala semiindustrial se incluyen los de la validación general del desarrollo (Artículo IV).

1.4.2.1. Escala de laboratorio

En primer lugar, se analizan las emisiones medidas en las pruebas de laboratorio (Figura 15) con el objetivo de evaluar el comportamiento del quemador experimental en las distintas condiciones de combustión consideradas.

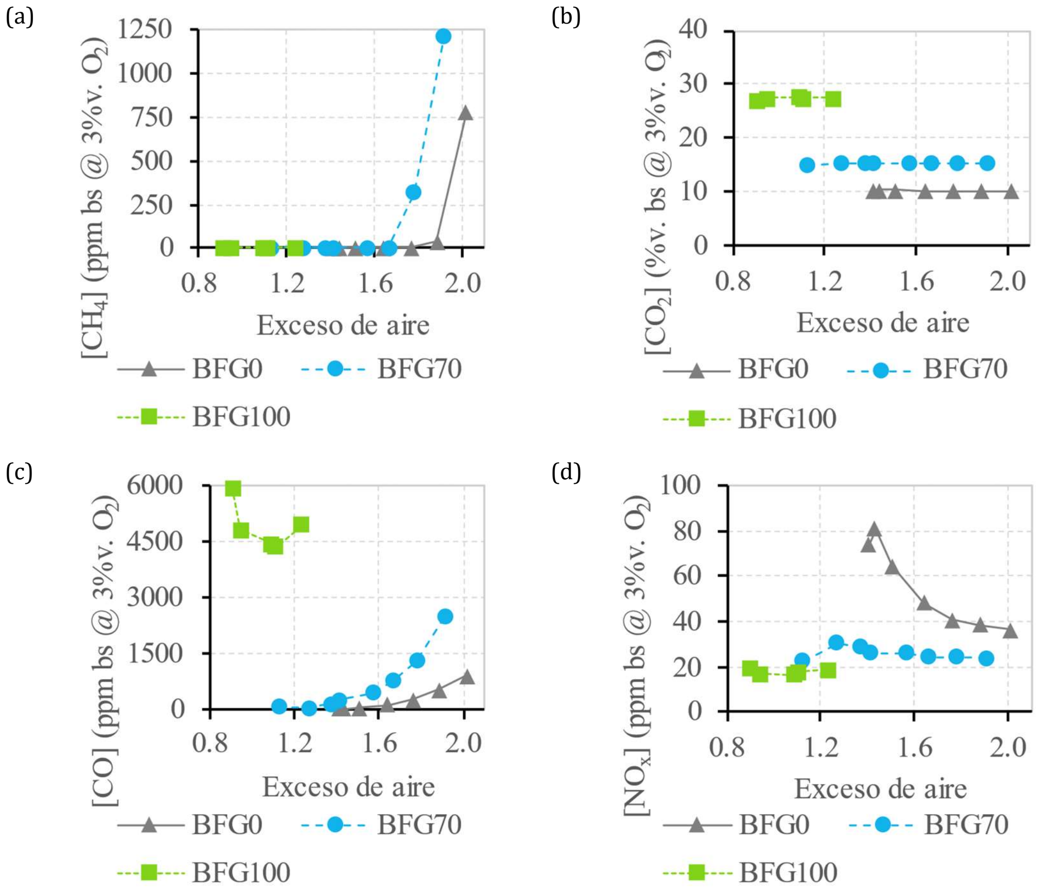

Figura 15. Concentración en los gases de combustión de (a) CH_4, (b) CO_2, (c), CO y (d) NO_x, para las mezclas BFG0, BFG70 y BFG100.

Para los puntos de operación con un exceso de aire por encima de 1.7 se detecta CH_4 en los gases, lo que es una prueba indirecta de combustión incompleta. El incremento del exceso de aire aumenta la velocidad de la mezcla de combustible y aire e inestabiliza la combustión, extinguiendo la llama en los puntos con un exceso de aire superior a 1.9.

Debido a la operación con una potencia térmica fija, las emisiones de CO_2 son constantes respecto al exceso de aire para un mismo combustible. La concentración de CO_2 aumenta al incrementar la proporción de gas de alto horno en la mezcla, ya que el CO_2 del combustible y el producido por el CO superan al generado por la combustión del CH_4.

Las emisiones de CO se incrementan al alejarse de las condiciones estequiométricas (exceso de aire de 1.0) debido a la combustión incompleta por falta de oxígeno o por inestabilidades de combustión. Además, el aumento de la proporción de gas de alto horno en la mezcla incrementa su contenido en CO.

La formación de NO_x está condicionada por la temperatura de llama y la disponibilidad de N_2 para su oxidación [83]. Al elevar la proporción de gas de alto horno en la mezcla, la temperatura adiabática de llama desciende [84], por lo que las emisiones de NO_x pueden reducirse, como ha ocurrido en los ensayos. Para el BFG0, la concentración de NO_x disminuye al aumentar el exceso de aire debido a su mayor caudal de aire y dilución asociadas [85]. En el caso del BFG70 y BFG100, el efecto de la dilución del aire no es tan significativo porque las mezclas ya incluyen unas altas concentraciones de diluyentes (CO_2 y N_2) [13].

Como conclusión, se observó la dependencia de las emisiones con la composición del combustible y el exceso de aire para el quemador experimental utilizado. Las tendencias son las esperadas para los excesos de aire inferiores a 1.7, aunque por encima de dicho valor se obtiene combustión incompleta. Este comportamiento se debe al uso del mismo quemador para las distintas mezclas de combustible, a pesar de sus elevadas diferencias en poder calorífico. De esta manera, cada mezcla se quema en condiciones subóptimas, pero se cumple el objetivo de replicar condiciones industriales al mantener fija la configuración del quemador.

Tras analizar las emisiones de los ensayos, se estudian los espectros de quimioluminiscencia para describir el comportamiento de los diferentes radicales. La Figura 16 muestra los espectros promedio para las mezclas de combustible y diferentes excesos de aire.

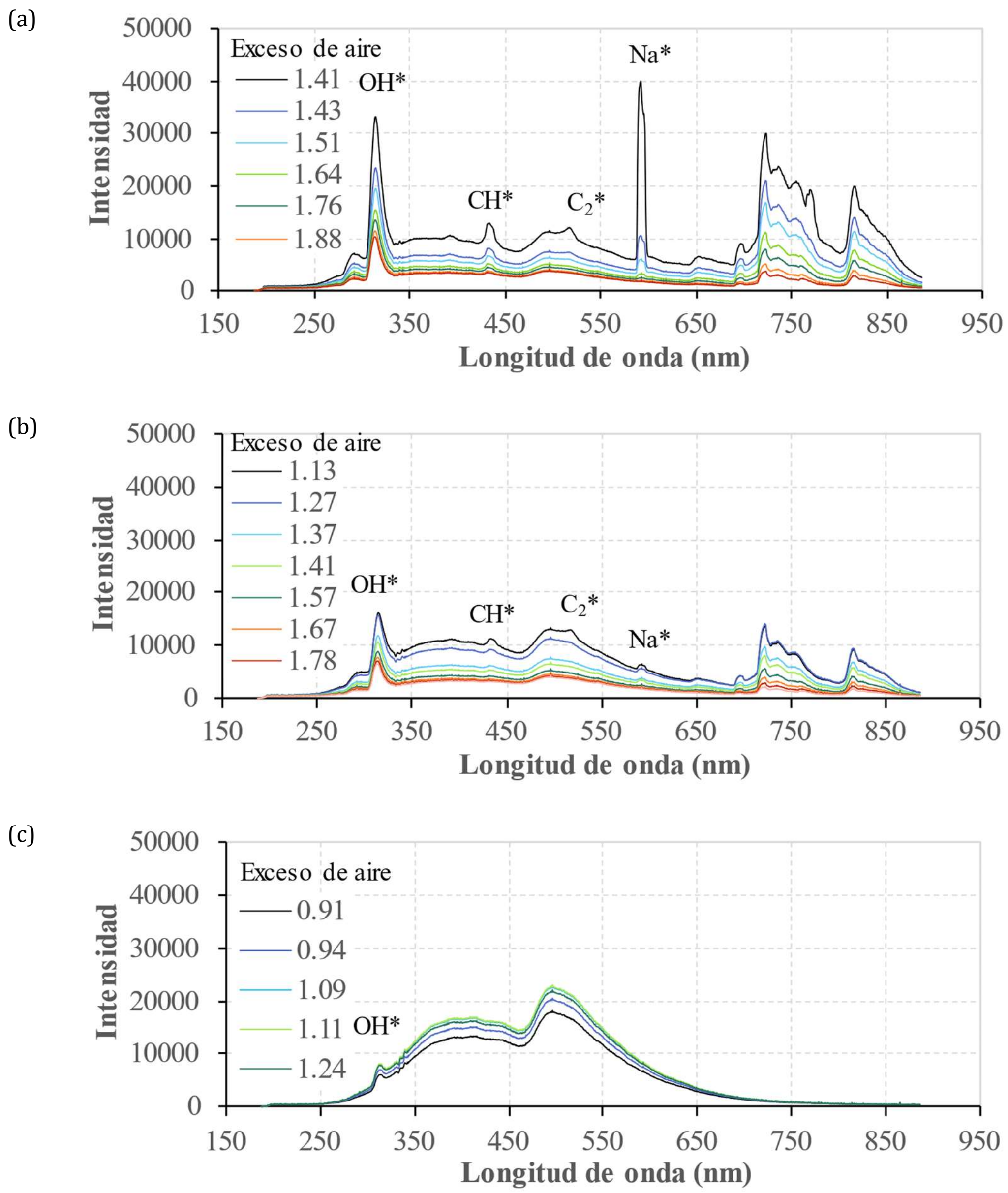

Figura 16. Espectro medio de las mezclas de combustible (a) BFG0, (b) BFG70 y (c) BFG100, para distintos excesos de aire.

Tal y como se puede observar en la Figura 16, los espectros de BFG0 (100% CH_4) y BFG100 tienen una forma característica muy diferenciada, mientras que el espectro de BFG70 comparte rasgos de ambos. En todos los casos, se observa cómo la intensidad en todo el ancho de banda se reduce al alejarse de las condiciones estequiométricas. La aparición de estos máximos de intensidad cerca de las condiciones estequiométricas ha sido previamente documentada para el OH* y CO_2* [21], [86], [87].

Para el BFG0 se observan las emisiones esperadas del OH*, CH* y C_2*, a 310, 430 y 470-515 nm. El espectro también muestra un máximo de intensidad a 589 nm, asociado al Na* originado en la combustión de impurezas provenientes de trazas [23], [88], [89]. Las emisiones para longitudes de onda entre 700 y 800 nm son similares a las registradas por Parameswaran et al. para la combustión de hidrocarburos con un quemador de premezcla [27]. La intensidad medida entre 630 y 900 nm se puede relacionar con distintas fuentes de radiación, como el HNO* (630 – 872 nm) [88]. Entre 813 y 847 nm también se encuentra la emisión de las transiciones vibracionales-rotacionales de moléculas diatómicas con hidrógeno, como el CH (813 – 847 nm), NH (829 – 844 nm) u OH (835 – 845 nm) [88]. Por último, la superficie del quemador también puede emitir radiación en este rango infrarrojo [21]. El espectro de BFG100 no tiene los máximos de CH* y C_2* porque no incluye CH_4 en su composición, aunque si aparece el de OH*, debido a su contenido en H_2. Además, el BFG tiene CO_2, que modifica el espectro con la emisión de banda ancha del CO_2*.

Las variaciones de OH* se pueden relacionar con las emisiones de CO y CO_2 según la ecuación CO + OH = CO_2 + H [90], por lo que el defecto de OH impide la reacción completa del CO, y su concentración incrementa a la vez que se reduce la del CO_2. Este comportamiento se confirma con los resultados experimentales, en los que la concentración mínima de CO (Figura 15.c) se relaciona con la intensidad máxima de OH* (Figura 16), asociada a la mayor concentración de OH.

A modo de resumen, los espectros medidos para la mezcla BFG0 coinciden con los resultados de referencias previas para la combustión de llamas. Además, las pruebas con BFG100 han permitido identificar su espectro, caracterizado por la emisión continua del CO_2*.

Tras estudiar la espectroscopía de quimioluminiscencia, se analizan las imágenes de llama adquiridas por las cámaras ultravioleta-visible y de color en la instalación de laboratorio. En la Figura 17 y Figura 18 se muestran varios ejemplos de imágenes, obtenidas con distinto exceso de aire.

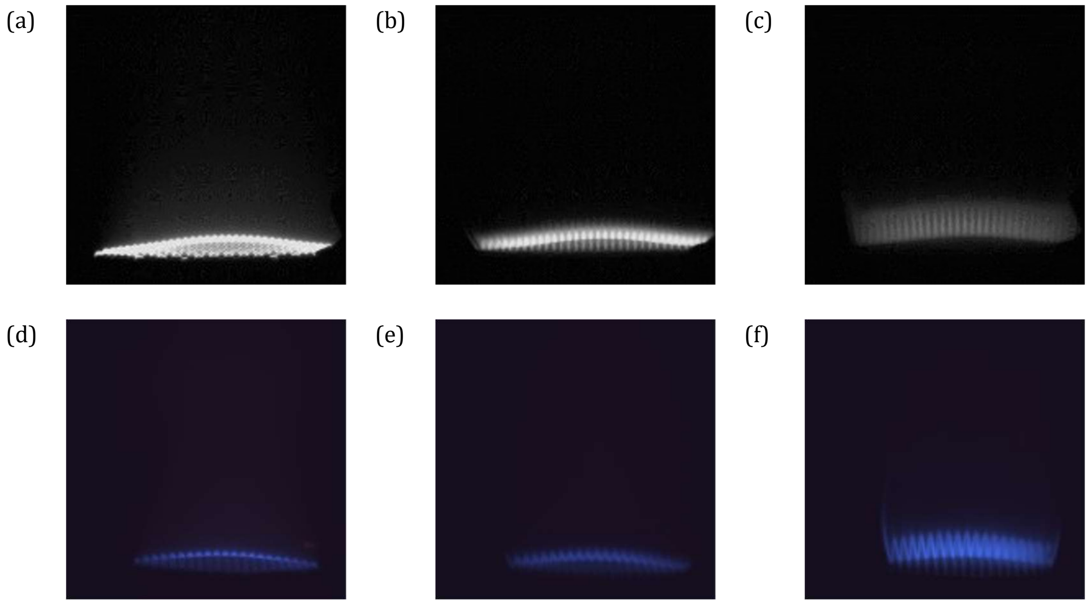

Figura 17. Imágenes de llama con exceso de aire de 1.3 ± 0.1, adquiridas por la cámara ultravioleta-visible con el filtro de 310 nm para las mezclas de combustible (a) BFG0, (b) BFG70 y (c) BFG100, y por la cámara de color para las mezclas (d) BFG0, (e) BFG70 y (f) BFG100.

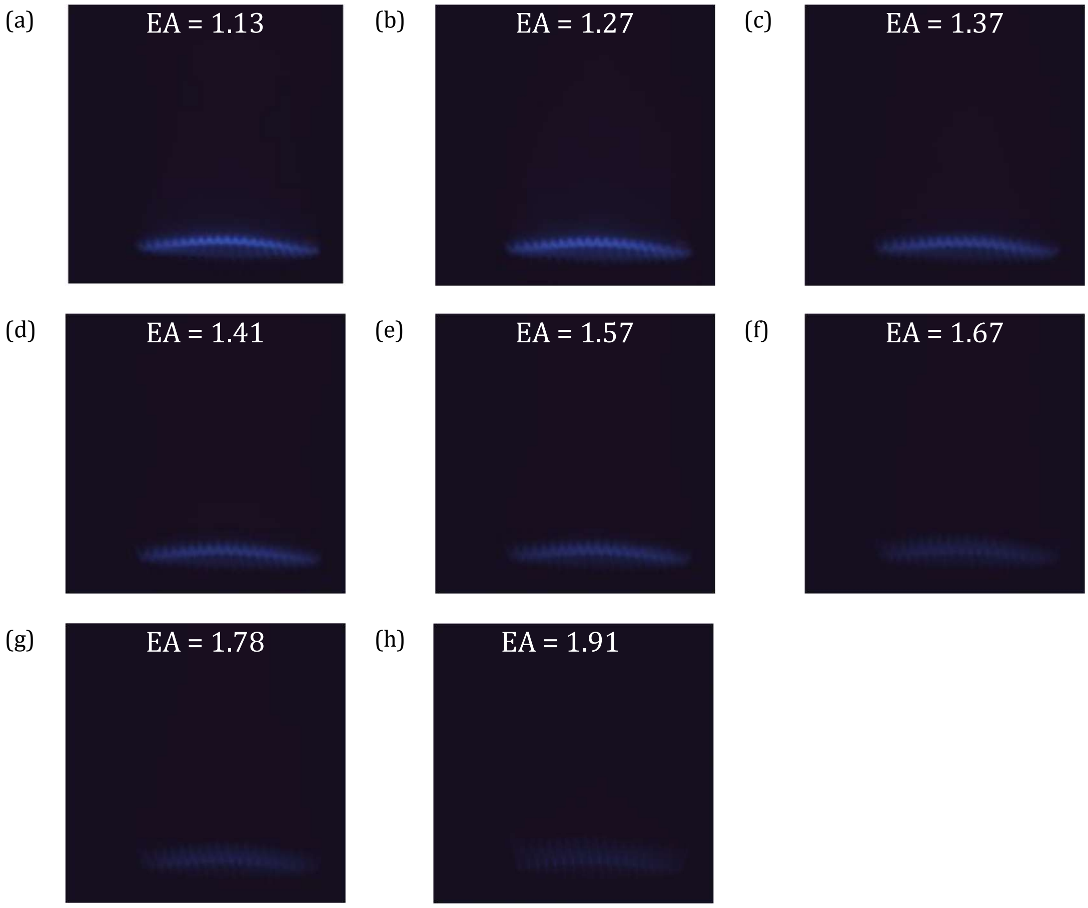

Figura 18, Imágenes de llama adquiridas con la cámara de color para la mezcla de combustible BFG70 y los excesos de aire de (a) 1.13, (b) 1.27, (c) 1.37, (d) 1.41, (e) 1.57, (f) 1.67, (g) 1.78 y (h) 1.91.

Las imágenes de llama se caracterizaron cuantitativamente mediante su procesamiento y la extracción de características. En un primer estudio se analizó la relación entre la mezcla de combustible y exceso de aire con varias propiedades de las imágenes ultravioleta-visible y color, mostradas en la Figura 19 y Figura 20, respectivamente.

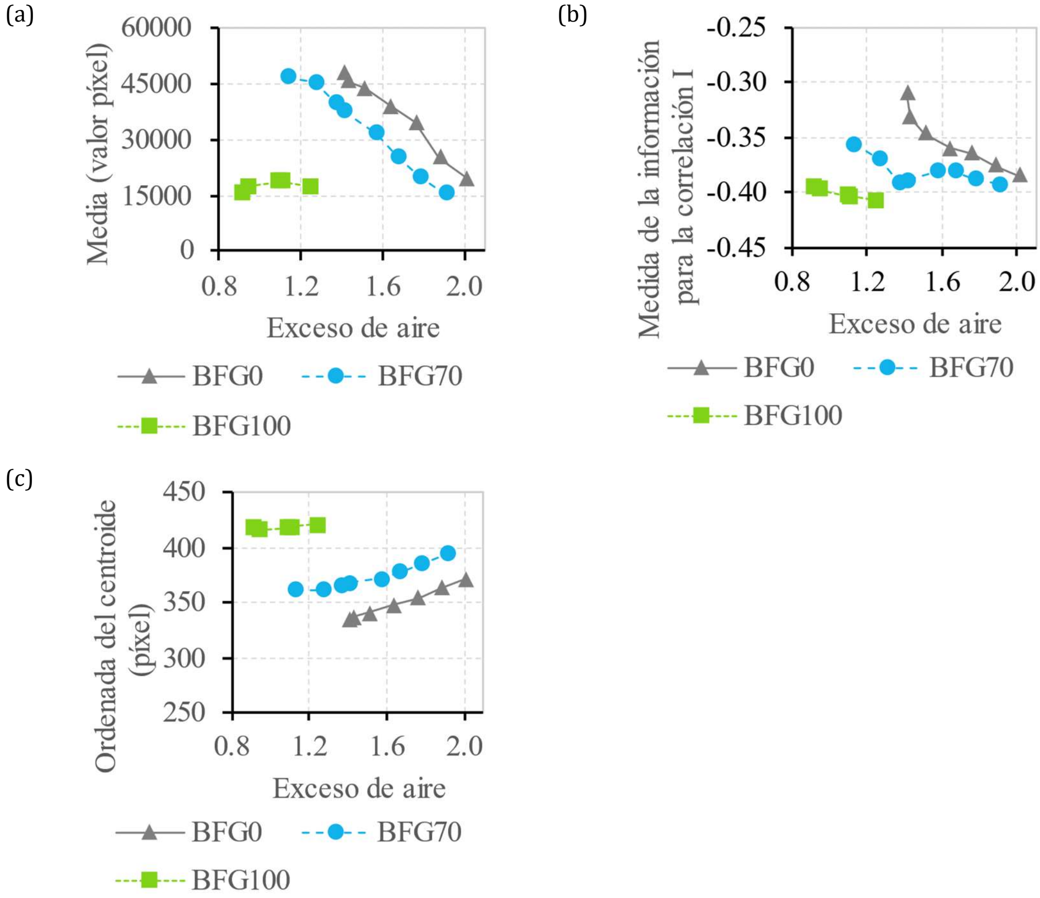

Figura 19. Características de (a) media, (b) medida de la información para la correlación I y (c) ordenada del centroide frente al exceso de aire, para las imágenes adquiridas por la cámara ultravioleta-visible con el filtro de 310 nm en laboratorio.

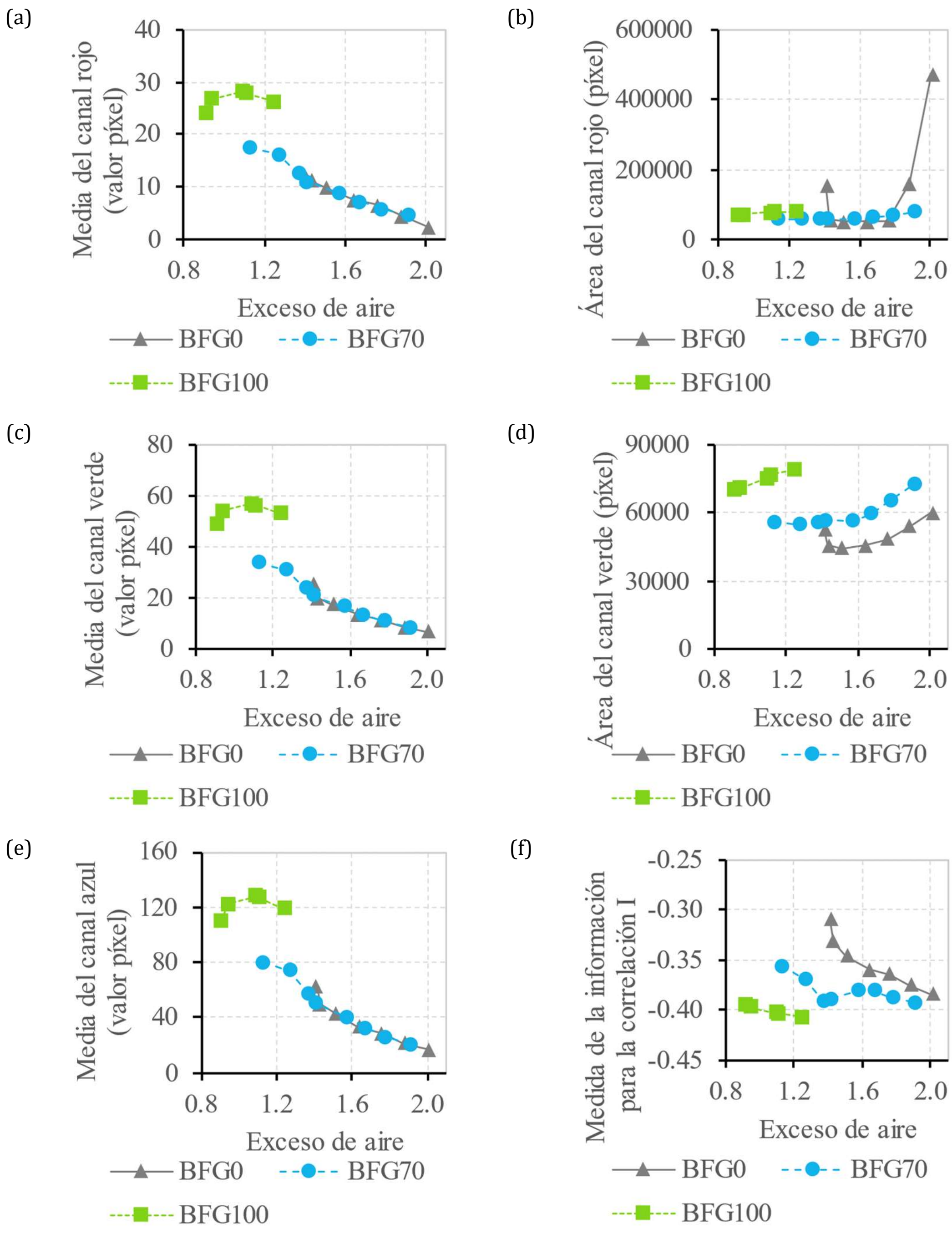

Figura 20. Características de media y área para el canal rojo (a, b), verde (c, d) y azul (e, f) frente al exceso de aire, para las imágenes adquiridas por la cámara de color en laboratorio.

Según los resultados obtenidos, se confirma la dependencia de las características de imagen con la mezcla del combustible y el exceso de aire, para los dos tipos de cámara (ultravioleta-visible y color). Además, dicha relación se puede definir a partir de características de intensidad, geometría o textura. En el caso de la cámara de color, las condiciones de combustión afectan a las propiedades extraídas de los tres canales de color.

La relación del exceso de aire con cada una de las 66 características de las imágenes de color se estudia en mayor detalle mediante un análisis de varianza. Para cada una de las 66 variables se calcula su estadístico F, definido como la proporción entre la varianza de los valores medios de una característica de imagen para cada una de las clases de exceso de aire, y la varianza de los valores de dicha característica a través de todas las clases de exceso de aire. A partir de este cálculo se confirmó que todas las propiedades visuales extraídas dependen del exceso de aire, y se eligieron las diez variables con un mayor estadístico F para alimentar los modelos predictivos. Las precisiones de validación de dichos modelos se muestran en la Figura 21.

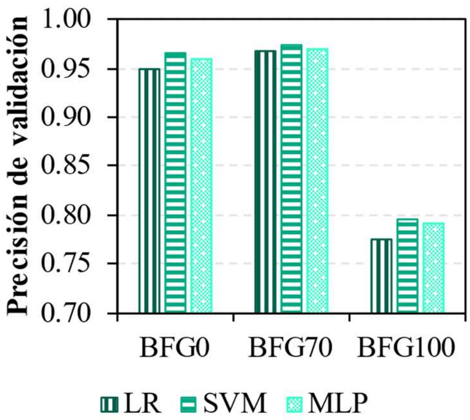

Figura 21. Precisiones de los modelos predictivos durante su validación para escala de laboratorio.

Los modelos predictivos alcanzaron precisiones de validación de 0.88 ± 0.09, que se incrementaron hasta 0.96 ± 0.01 para las mezclas BFG0 y BFG70. Estos modelos consiguen predecir variaciones del exceso de aire más pequeñas que las monitorizadas en trabajos anteriores, consiguiendo una precisión similar en la identificación de las clases [54], [91]. En esta tarea de clasificación, los distintos tipos de algoritmo considerados no afectan significativamente a la precisión de los modelos, teniendo una desviación máxima del 3 %. Para estudiar más en detalle la precisión de los modelos según la clase del exceso de aire, se calcularon sus matrices de confusión (Figura 22).

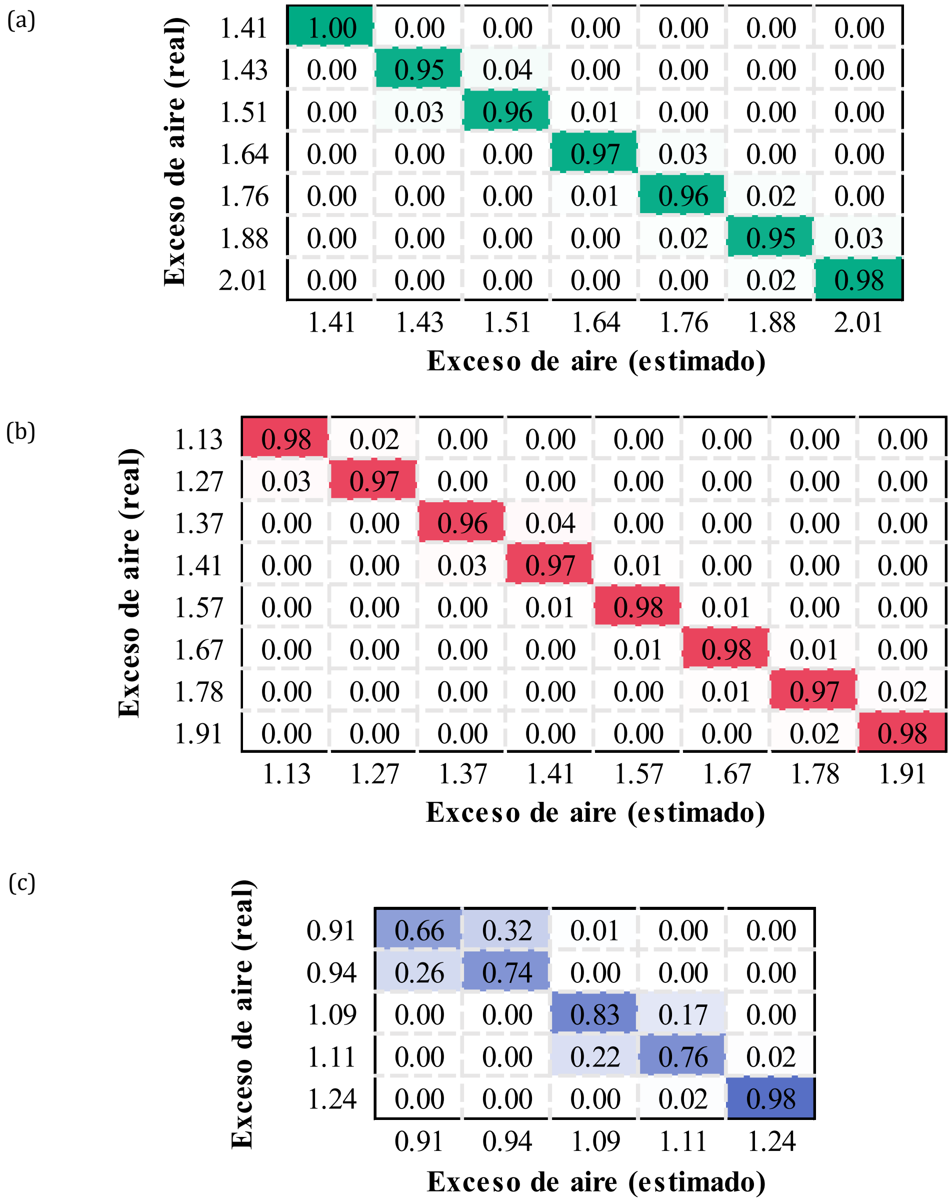

Figura 22. Matrices de confusión de los modelos predictivos basados en el algoritmo de SVM, durante su validación en laboratorio para las mezclas de combustible (a) BFG0, (b) BFG70 y (c) BFG100.

Los modelos para las mezclas BFG0 y BFG70 alcanzaron una precisión similar, independientemente de la clase del exceso de aire considerada. En el caso de BFG100, se observa que los errores se incrementan al predecir clases del exceso de aire con diferencias inferiores a 0.04. No obstante, para la mezcla BFG0 se consiguió una mayor precisión en la detección de estados con pequeñas diferencias (1.41 y 1.43). Este comportamiento podría ser debido a la menor estabilidad (menor poder calorífico) de la mezcla BFG100. Para esta mezcla también se observó que la precisión aumentó con el incremento del exceso de aire, que también puede relacionarse con el aumento de estabilidad [84].

1.4.2.2. Escala semiindustrial

Los resultados obtenidos en laboratorio proporcionan una base sobre la que continuar la investigación a escala semiindustrial, que se analiza a continuación.

En la primera campaña experimental a escala semiindustrial se adquirieron imágenes de llama, de las que la Figura 23 incluye unas muestras para la mezcla BFG70 y distintos valores de $[O_2]_{fg}$.

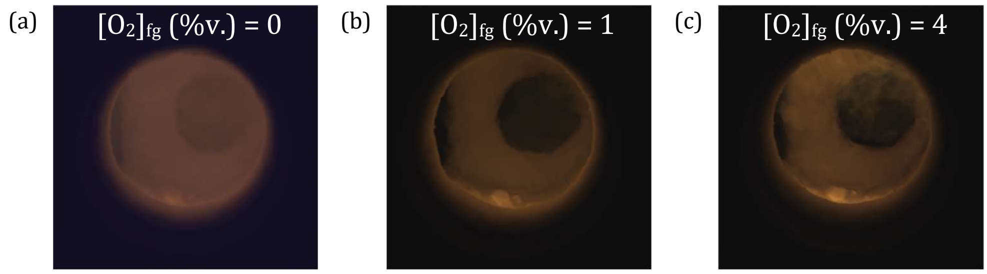

Figura 23. Imágenes de llama para la mezcla BFG70 en las pruebas iniciales semiindustriales.

De las características de imagen extraídas, la asimetría en el canal azul (Figura 24) tenía una mayor dependencia con la concentración de oxígeno en gases de combustión para las tres mezclas de combustible. La detección de esta relación sirve de confirmación preliminar de la viabilidad de los métodos utilizados para la monitorización en escala semiindustrial.

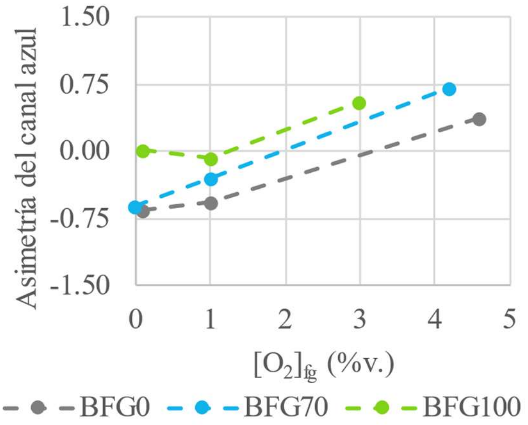

Figura 24. Característica de imagen de la asimetría azul frente a $[O_2]_{fg}$.

La segunda campaña experimental en escala semiindustrial permitió profundizar en el estudio de la combustión con la adquisición de un mayor volumen de imágenes. También se utilizó un sistema de visión introducido dentro del horno, que incrementó el campo de visión de la cámara y la información capturada. De esta manera se facilitó la monitorización visual de la combustión.

La Figura 25 muestra las imágenes de llama adquiridas en condiciones estacionarias para las mezclas de combustible BFG0, BFG70 y BFG80, con distintas concentraciones de oxígeno en los gases de combustión. En el caso de la mezcla BFG70, el régimen transitorio también se analizó (Figura 26).

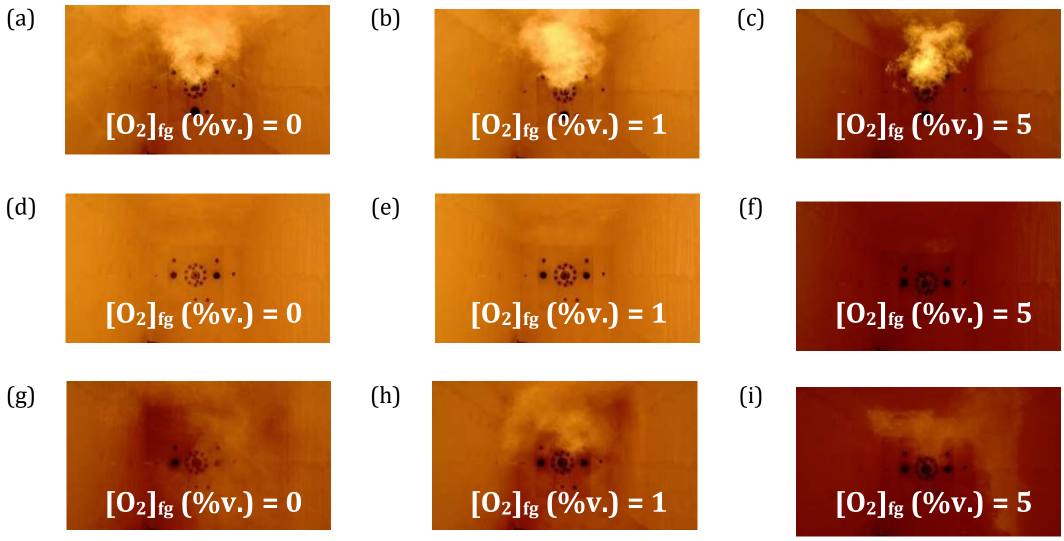

Figura 25. Imágenes de llama capturadas para la escala semiindustrial, en condiciones estacionarias y con las mezclas de combustibles (a, b, c) BFG0, (d, e, f) BFG70 y (g, h, i) BFG80.

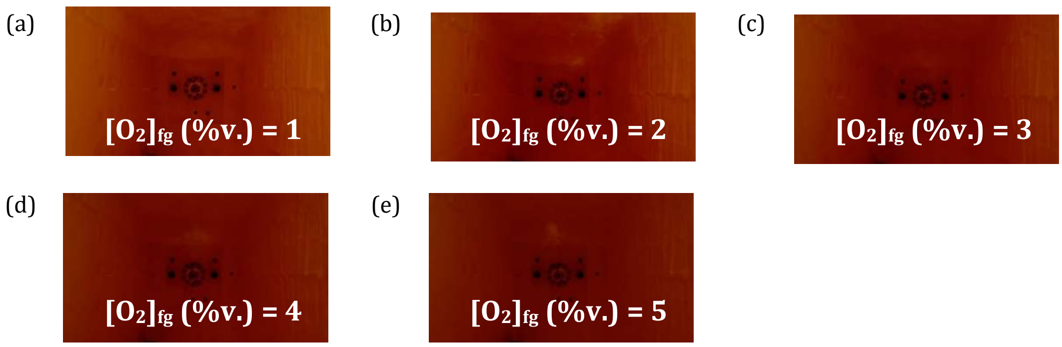

Figura 26. Imágenes de llama capturadas para la escala semiindustrial, en condiciones transitorias, con la mezcla de combustible BFG70 y $[O_2]_{fg}$ de (a) 1, (b) 2, (c) 3, (d) 4 y (e) 5 %v.

En las imágenes predominan las tonalidades anaranjadas, propias de las llamas de difusión y las emisiones del hollín [92]. Las partículas de hollín emiten radiación similar a la de cuerpo negro [18], cuya intensidad incrementa con la temperatura según la ley de Planck [93]. Esto permite, por ejemplo, la estimación de la temperatura del hollín a través de imágenes de llama [94]. En las imágenes de llama se observa un incremento de la luminosidad al reducir la proporción de gas de alto horno en la mezcla, y al acercarse a condiciones estequiométricas. Estas variaciones de operación se relacionan con un aumento de la temperatura de la cámara de combustión (Figura 27), confirmando el comportamiento descrito por la ley de Planck.

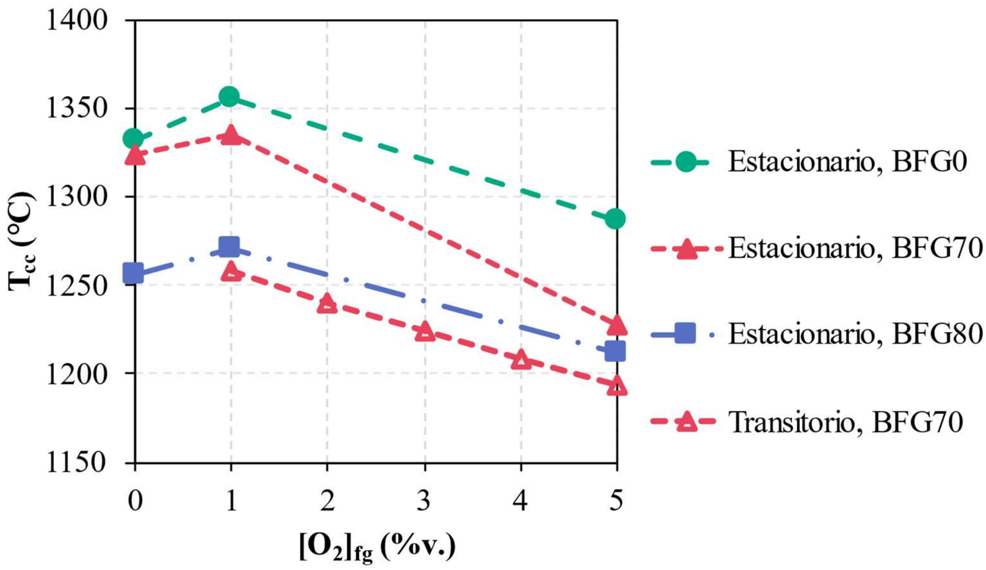

Figura 27. T_{cc} en los ensayos semiindustriales.

La composición del combustible y el exceso de aire afectan más al color de las llamas de premezcla respecto a las de difusión [19]. No obstante, las imágenes capturadas permiten detectar estas variaciones incluso para las llamas de difusión. La menor visibilidad de las llamas para las mezclas BFG70 y BFG80 se debe a la elevada proporción de gases inertes en el combustible, con aproximadamente 35 %v de N_2 y 15 %v de CO_2. En un trabajo previo [18] se observó un comportamiento similar al incrementar la dilución con N_2 de llamas de difusión y metano, lo que redujo el pico de quimioluminiscencia de OH*.

Mediante el análisis de varianza, se concluye que todas las propiedades visuales calculadas dependían de las clases de la concentración de oxígeno en gases de salida. A modo de ejemplo, la Figura 28 muestra la media de los valores píxel del canal rojo, cuyo comportamiento sigue las tendencias observadas previamente para la luminosidad de las imágenes y la temperatura de la cámara de combustión (Figura 27).

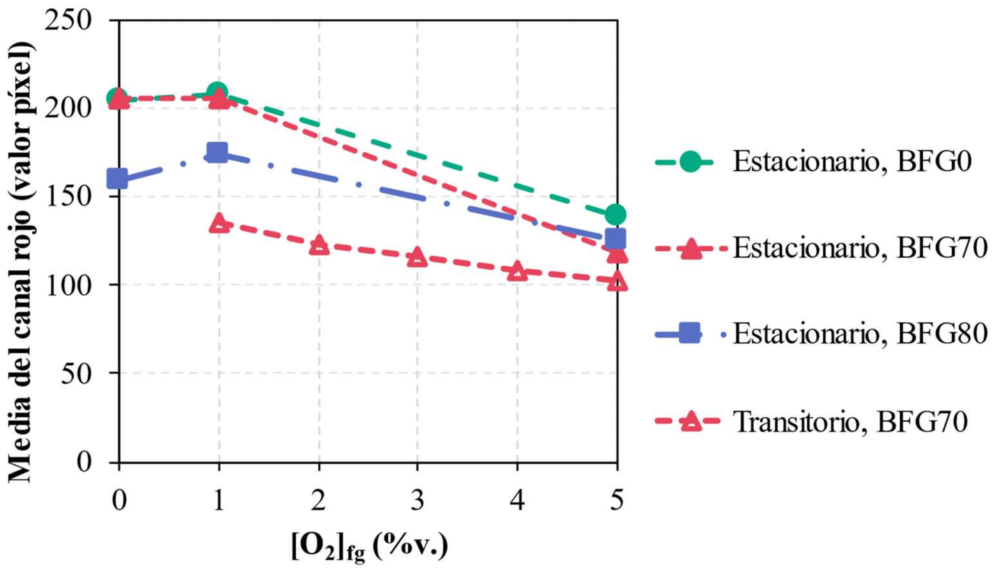

Figura 28. Media de la intensidad para el canal rojo frente a $[O_2]_{fg}$ en los ensayos semiindustriales.

El conjunto de las diez características de imagen con un mayor estadístico F se utilizó como entrada para los modelos predictivos, que alcanzaron una precisión de validación en torno a 0.995, reducida a 0.960 para la mezcla BFG70 en condiciones estacionarias (Tabla 8).

Tabla 8. Precisiones de validación de los modelos predictivos en la estimación de $[O_2]_{fg}$ en escala semiindustrial.

Serie de ensayos	SE1	SE2	SE3	SE4
Régimen	Estacionario	Estacionario	Estacionario	Transitorio
Mezcla de combustible	BFG0	BFG70	BFG80	BFG70
LR (precisión)	0.9920	0.9666	0.9970	0.9998
SVM (precisión)	0.9936	0.9671	0.9980	0.9999
MLP (precisión)	0.9866	0.9640	0.9962	0.9998

Los tres algoritmos de aprendizaje automático proporcionaron resultados similares, aunque la SVM alcanzó la mayor precisión en todos los casos, superando a las redes neuronales. Este comportamiento también se observó en la escala de laboratorio y en un trabajo previo [91].

Los modelos predictivos se integraron en un programa informático para monitorizar el proceso de combustión en tiempo real y facilitar su uso en la industria (Figura 29). La aplicación analiza imágenes de llama y genera sus ventanas de visualización cada 0.35 segundos. Este periodo de muestreo proporciona una monitorización continua y detallada del proceso de combustión, cuyas emisiones tienen una dinámica cuatro órdenes de magnitud más lenta que el programa (tiempo de estabilización de media hora).

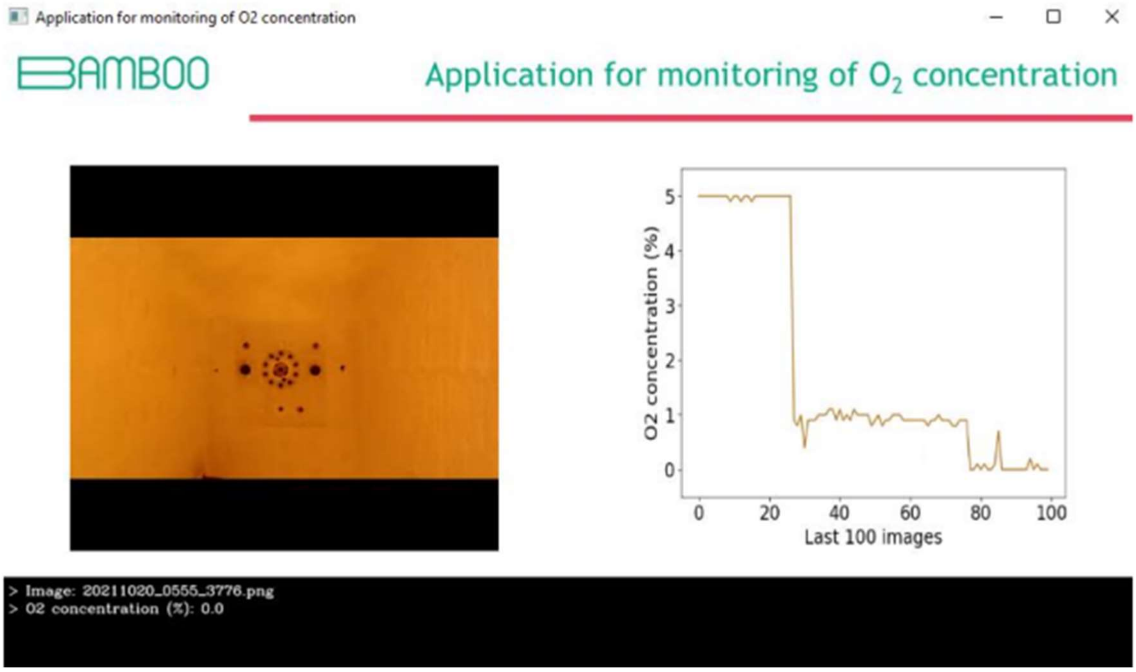

Figura 29. Ventana del programa informático para la monitorización en tiempo real de $[O_2]_{fg}$.

1.4.2.3. Validación del desarrollo

Las diferencias entre las fases de desarrollo del sistema de monitorización se pueden agrupar en tres clases: escala (laboratorio o semiindustrial), quemador (premezcla o difusión) y posición del sistema respecto a la cámara de combustión (exterior o interior).

La Figura 30 muestra imágenes de llama obtenidas en distintas fases de desarrollo para la mezcla de combustible BFG70 y valores similares de concentración de oxígeno en gases de combustión. Las llamas de laboratorio tenían un contorno definido, mientras que su geometría era difusa en escala semiindustrial. No obstante, la variación de la concentración de oxígeno en los gases de salida afectaba a las imágenes en ambos casos. Por lo tanto, la cámara de color se validó como un sensor de imagen adecuado para la monitorización de la combustión con BFG para quemadores de premezcla y difusión.

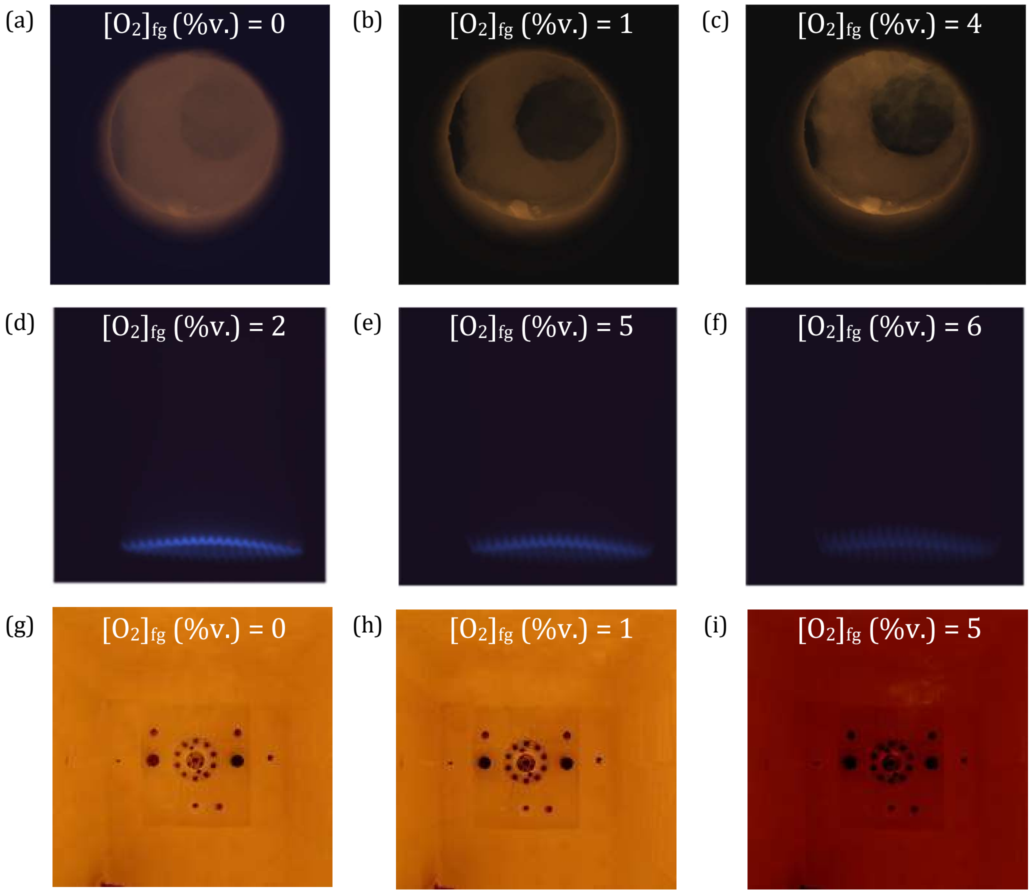

Figura 30. Imágenes de llama para la mezcla de combustible BFG70 y distintos valores de $[O_2]_{fg}$ y fases de desarrollo: escala semiindustrial con (a, b, c) ubicación exterior e (g, h, i) interior, y (d, e, f) escala de laboratorio con ubicación exterior.

Las características extraídas de las imágenes se relacionaron con las condiciones de combustión en todas las fases del desarrollo. A modo de ejemplo, la Figura 31.a recoge el comportamiento de la media de la intensidad para el canal rojo y la mezcla BFG70, cuya tendencia es similar en todos los escenarios. Los modelos predictivos alcanzaron una alta precisión, tanto para escala de laboratorio como semiindustrial (Figura 31.b), obteniéndose valores superiores a 0.95 excepto para las pruebas de BFG100 en laboratorio, con una precisión de 0.80. Según estos resultados, las características de imagen calculadas y los modelos predictivos entrenados se validaron para la monitorización de llamas de alta y baja visibilidad en escala de laboratorio y semiindustrial.

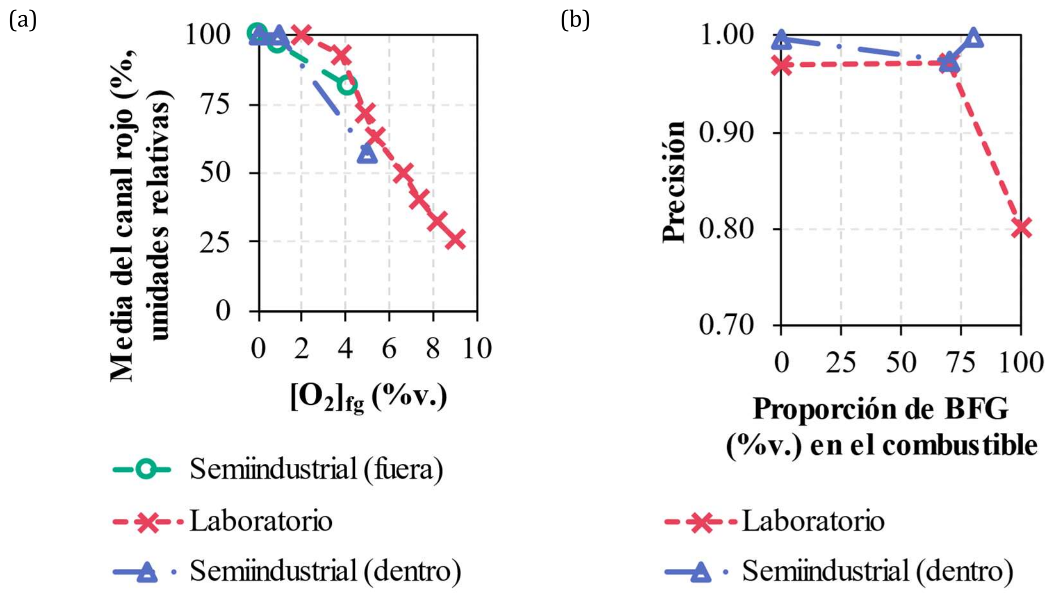

Figura 31. (a) Media de la intensidad para el canal rojo frente a $[O_2]_{fg}$ para la mezcla BFG70, durante distintas fases de desarrollo, y (b) precisiones de los modelos predictivos para los grupos de prueba de distintas mezclas de combustible y fases de desarrollo.

2. Publicaciones

2.1. Artículo I

Optical analysis of blast furnace gas combustion in a laboratory premixed burner. P. Compais, J. Arroyo, A. González-Espinosa, M. A. Castán-Lascorz, A. Gil. **ACS Omega** (2022); Vol. 7, pp. 24498-24510.

ACS OMEGA

http://pubs.acs.org/journal/acsodf Article

Optical Analysis of Blast Furnace Gas Combustion in a Laboratory Premixed Burner

Pedro Compais, Jorge Arroyo,* Ana González-Espinosa, Miguel Ángel Castán-Lascorz, and Antonia Gil

Cite This: ACS Omega 2022, 7, 24498−24510 Read Online

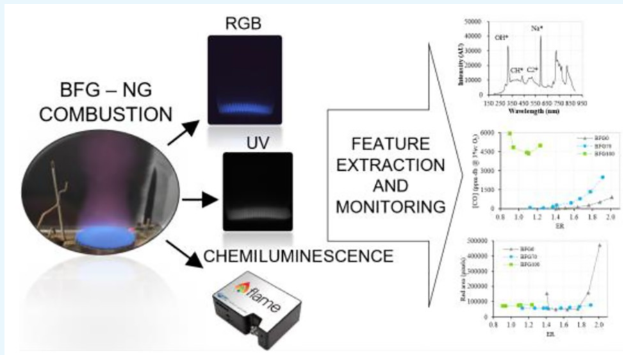

ABSTRACT: The use of blast furnace gas (BFG) as a fuel provides an alternative for waste stream valorization in the steel industry, enhancing the sustainability and decarbonization of its processes. Nevertheless, the implementation of this solution on an industrial scale requires a continuous control of the combustion due to the low calorific value of BFG. This work analyzes the combustion behavior and monitoring of BFG/CH_4 blends in a laboratory premixed fuel burner. We evaluate several stable combustion conditions by burning different BFG/CH_4 mixtures at a constant power rate over a wide range of air/fuel equivalence ratios. In addition, relevant image features and chemiluminescence emission spectra have been extracted from flames, using advanced optical devices. BFG combustion causes an increase in CO_2 and CO emissions, since those fuels are the main fuel components of the mixture. On the other hand, NO_x emissions decreased because of the low temperature of combustion of the BFG and its mixtures. Chemiluminescence shows that, in the case of CH_4 combustion, peaks associated with hydrocarbons are present, while during the substitution of CH_4 by BFG those peaks are attenuated. Image flame features extracted from both ultraviolet and visible bandwidths show a correlation with the fuel blend and air/fuel equivalence ratio. In the end, methodologies developed in this work have been proven to be valuable alternatives with a high potential for the monitoring and control of BFG cofiring for the steel industry.

1. INTRODUCTION

Currently, energy-intensive industries are directing their processes toward more sustainable models. Thus, industrial processes can increase their efficiency and reduce pollutant emissions. In order to meet these objectives, several strategies are being promoted, such as waste heat recovery,[1] waste stream valorization,[2] and electrical flexibility.[3] In the case of the steel industry, multiple waste gas streams with calorific value are produced. One of these streams is blast furnace gas (BFG), a byproduct of the chemical reduction of iron ore developed in blast furnaces. BFG can be valorized through combustion for different processes, such as gas turbines, steelmaking−annealing lines, or reheating of furnaces.[4−6] Among all these applications, the steel industry is highly interested in BFG valorization within the same facility where it is produced. Nevertheless, the combustion of BFG in steelmaking processes faces several drawbacks. Due to the large concentration of inert gases in its composition, blast furnace gas does not provide enough thermal energy to meet the temperature requirements of steelmaking processes.[7] Several strategies have been used to overcome this, such as preheated combustion air and a higher calorific gas as a support fuel. In Europe, BFG is usually mixed with natural gas (NG), while in other regions, such as Brazil, India, and China, BFG is blended with other fuels, such as fuel oil.[8] Furthermore, the low calorific value of the BFG also results in more unstable combustion,[6,7] which may move the operation toward suboptimal conditions and even produce flame extinction. Therefore, BFG combustion needs to be monitored and controlled to correct suboptimal conditions. Traditional sensors can be used to monitor the fuel and airflow of each furnace burner. However, the high number of burners in industrial furnaces increases the cost of this alternative and limits its application. Therefore, the steel industry has searched for novel combustion monitoring systems based on optical techniques, which have been scarcely reported in the open literature on industrial-level applications.[9] Implementing such monitoring systems on such a large scale requires a complex development with extensive studies at laboratory, semi-industrial, and industrial scales. In this aspect, studies of the different scales have not been previously considered.

Received: April 5, 2022
Accepted: June 23, 2022
Published: July 7, 2022

https://doi.org/10.1021/acsomega.2c02103
ACS Omega 2022, 7, 24498−24510

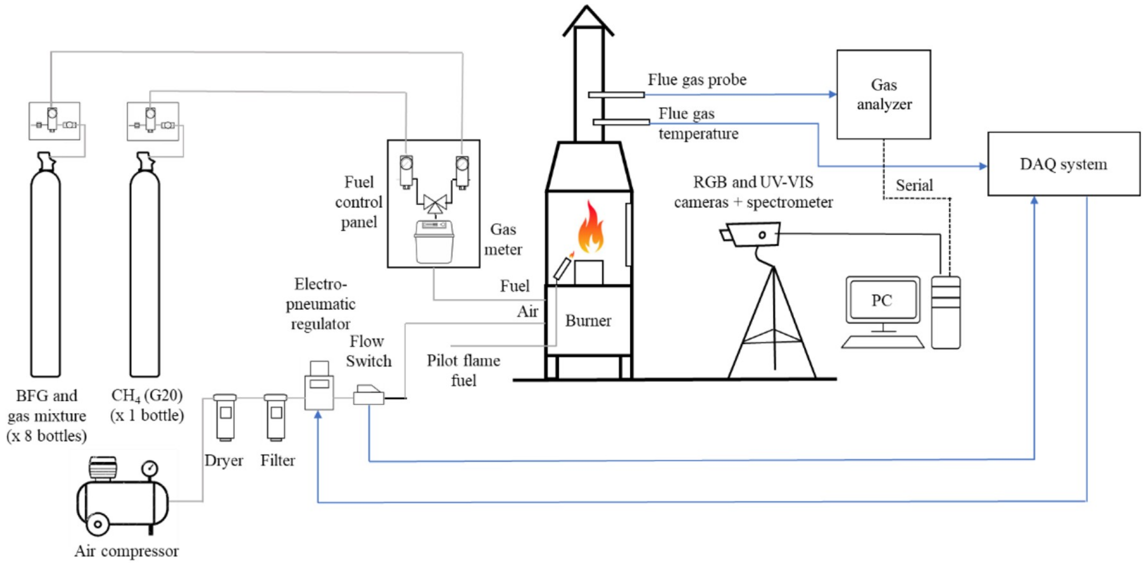

Figure 1. Scheme of the experimental facility.

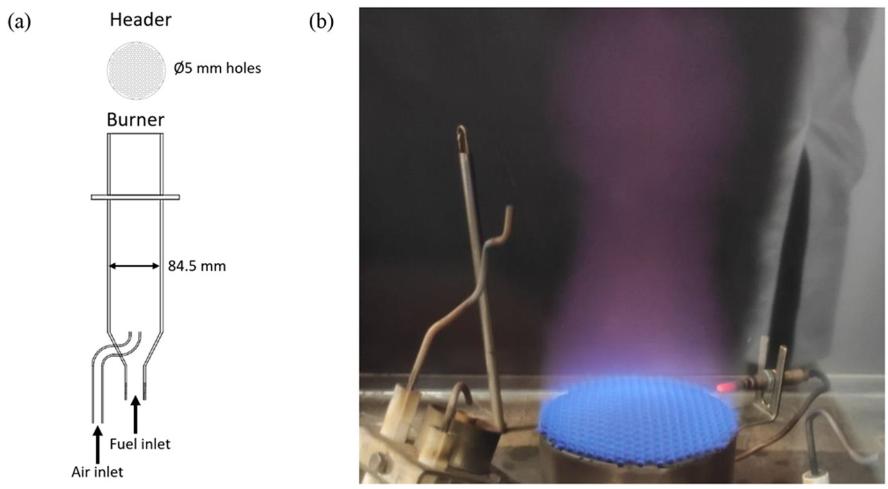

Figure 2. (a) Scheme of the premixed gas fuel burner and (b) example of a flame generated in the test combustion chamber.

Several advanced optical techniques have been used to monitor and control the combustion process. They involve analyzing energy radiated by the flames, which depends on various combustion factors. For diffusion flames, energy emission is dominated by continuous radiation (black-body emission) related to soot production.[10,11] In contrast, the emission of premixed flames is mainly characterized by multiple emissions in discrete wavelengths, related to the transition of intermediate combustion radicals from excited to ground states, known as chemiluminescence,[10] which is affected by the reactant composition and equivalence ratio.[10,12]

In order to study the chemiluminescence phenomenon, optical instruments, such as spectrometers and cameras, have been extensively employed to capture spectra and flame images, respectively. In most cases, a huge amount of collected information needs to be processed to extract specific features to characterize flames for different fuel blends,[13] air or fuel flows,[13,14] air swirls,[15] and temperatures.[16]

First, spectrometers capture chemiluminescence emissions from the ultraviolet (UV) to the infrared (IR) ranges, associating specific wavelengths with the reaction of chemical species. Combustion studies are typically focused on detecting combustion radicals such as OH*, CH*, C_2*, and CO_2*. On one hand, OH*, CH*, and C_2* provide narrow-band emissions at around 310 nm (OH*),[17−23] 430 nm (CH*),[17−23] 470 nm (C_2*),[17,19,21] and 515 nm (also C_2*).[17−21,23] On the other hand, CO_2* is related to broad-band emissions from approximately 350 to 610 nm.[17,18,20,21]

Second, research on combustion chemiluminescence can also be developed with imaging techniques. For that purpose, cameras for UV, visible (vis), and IR ranges are set up with narrow-band filters to only measure light emissions related to the relevant radicals.[22,24−26] For example, the measurement of OH* emissions with imaging techniques enables the characterization of premixed flame fronts.[22,26,27] In addition, hyperspectral cameras can also be used to measure light emissions of several radicals simultaneously.[28]

Finally, cameras without narrow-band filters can also be used to characterize flame radiation, usually measuring the VIS range. Most studies use statistical characteristics of the image pixel values,[13−16,29−32] which are related to the intensity of light emissions. Additionally, other methods can also compute

https://doi.org/10.1021/acsomega.2c02103
ACS Omega 2022, 7, 24498−24510

texture[14,33] and geometrical characteristics[15,31,34−36] and flame speeds.[37,38] Before the characteristics are extracted from the image, several preprocessing techniques are used. These preprocessing techniques include the averaging of image sequences,[29,30,32] flame segmentation with thresholding,[13,15,16] noise filters,[14] color space conversions to grayscale,[15] and finally hue, saturation, and intensity (HSI).[31,36]

The present research aims to characterize the combustion of BFG for the partial replacement of CH_4 in a premixed laboratory-scale burner. For that purpose, three optical devices are simultaneously employed to provide a more complete and robust insight into the combustion process. Flame emissions are measured by a spectrometer, a UV−vis camera with a narrow-band filter, and a vis camera. Spectra and image features are analyzed for different fuel blends, air/fuel equivalence ratios, and flue gas compositions. Furthermore, this research constitutes the first step toward the development of a novel combustion monitoring system based on optical techniques to enable BFG cofiring with NG in steelmaking furnaces.

2. MATERIALS AND METHODS

The present section describes the methodology used in the research. The final aim of the work is the the diagnosis of combustion on the basis of flame optical parameters, and it is mainly intended for industrial furnaces. The experimental procedures have been defined similarly to those of an industrial environment, where the level of tunability and configuration of the commercial burners is limited. This way, by defining a similar procedure for laboratory and industrial scales, the methodology developed in the laboratory can be implemented in industry with lower barriers.

2.1. Experimental Setup. Tests were carried out in a customized combustion chamber equipped with a 20 kWth premixed gas fuel burner, designed to enable extensive visual characterization and flue gas measurements. Figure 1 shows the overall scheme of the facility. The fuel and air enter the premixed gas fuel burner through two separate inlets (25 and 10 mm diameters, respectively) (Figure 2a). The fuel/air mixture leaves the burner via a 100 mm diameter header and a pattern of holes of 5 mm, as shown in Figure 2a. Although different headers can be used for each fuel in order to optimize the working conditions in this research, the same header has been used. This way, standard procedures are simulated on an industrial scale. The flame generated is enclosed in a sealed combustion chamber with a width and depth of 65 cm and a height of 90 cm (see Figure 2b). The chamber is equipped with both quartz and glass inspection windows in order to enable energy transmission in the UV and VIS ranges, respectively. A pilot flame is used to start the combustion, which increases the facility's safety by burning the remaining fuel from previous operations.

The burner is fed with bottles of gaseous fuels whose mixtures are blended by a gas supplier. The gaseous fuels feed the burner via two independent gas lines designed to admit gaseous fuels of highly different heating values. For CH_4, one line with a batch of one bottle is used. For the BFG and mixtures, a line connected to a batch of eight bottles is employed, which allows carrying out the tests continuously, despite the high consumption of fuel. The amount of gas fed to the burner is measured by a volumetric flow meter. The facility also has a safety system to stop the fuel supply when leakages are detected.

The combustion air is supplied by a compressor, whose pressure (and thus flow rate) is controlled by an SMC ITV2000 electropneumatic regulator. Before burner connection, the airflow rate is measured by an IFM SD6000 flow switch, with a repeatability of ±1.5% and an accuracy of ±(3% reading + 0.3% full scale). The electropneumatic regulator and flow switch communicate with a computer through a data acquisition system, which also collects the flue gas temperature measured by a thermocouple. Since flue gas temperatures were measured at the exhaust duct of the test rig, they are only qualitative measurements. Thus, these flue gas temperatures are not representative of the combustion and product behavior.

Furthermore, exhaust gas emissions were measured with an MRU Vario Plus Industrial gas analyzer. Concentrations of O_2, CO, CO_2, NO_x, and CH_4 in the combustion gases were measured with the a analyzer, whose measurement principles, ranges of measurement, and accuracies are summarized in Table 1.

Table 1. Specifications of the Gas Analyzer

gas	measurement principle	range	accuracy
O_2	electrochemical	0−21.0 %v	±0.2 %v abs
CH_4	nondispersive infrared (NDIR)	0−10000 ppm	±60 ppm or 5% reading
CO	NDIR	0−10000 ppm	±40 ppm or 5% reading
CO_2	NDIR	0−30 %v	±0.5% or 3% reading
NO	electrochemical	0−1000 ppm (up to 5000 ppm)	±5 ppm or 5% reading ≤1000 ppm
			10% reading >1000 ppm
NO_2	electrochemical	0−200 ppm (up to 1000 ppm)	±5 ppm or 5% reading ≤200 ppm
			10% reading >200 ppm

Three optical devices were employed to characterize the combustion: a spectrometer (Ocean Optics Flame-S Miniature), an electron multiplying charge-coupled device (EMCCD) camera for the UV−visible (UV−vis) range (Raptor Photonics Falcon Blue), and a red/green/blue (RGB) camera (The Imaging Source DFK 33GX174). The spectrometer and UV−vis and RGB cameras included a Sony ILX511B sensor with 2048 pixels of resolution, a Texas Instruments TC285SPD sensor (1.0 megapixels), and a Sony IMX174LQJ sensor (2.3 megapixels), respectively. The UV−vis camera was set with a narrow-band optical filter (310 ± 10 nm, ASAHI). In the case of the RGB camera, the sensitivity of its color channels is maximized for the approximate ranges of 580−800 nm (red channel), 475−600 nm (green channel) and 400−500 nm (blue channel).

Experimental tests were carried out for three different fuel gases, defined according to the industrial interest in the substitution of NG by BFG, to increase the efficiency of the processes. Higher percentages of BFG help to reduce NG consumption and, consequently, fossil fuel emissions. However, blends with a high percentage of BFG, which has a low heating value, limit the maximum temperature inside the combustion chamber and result in some operational problems associated with the high gas flow needed to satisfy the furnaces' demand.[4] Consequently, the amount of BFG in the mixture is limited and some NG is needed to reach the temperatures needed for the steel production processes.[6] For example, in a study by Zheng et al.,[6] the adiabatic flame temperature is increased between 10% and 20% by increasing the CH_4 share in the BFG blend from 0 to 15 %v.

In the present research, a 70 %v BFG gaseous mixture (BFG70) was chosen, since it contains the minimum amount of CH_4 required to reach the steel processing temperatures (1100−1300 °C) in industrial reheating furnaces.[4] On the other hand, pure BFG (BFG100) and G20 CH_4 (BFG0) have been defined as baseline fuels for the tests.

The compositions of the fuel blends and their lower heating values (LHV) are collected in Table 2. BFG0, BFG70, and BFG100 were fed at manometric pressures of 10, 86, and 82 mbar, respectively.

Table 2. Fuel Blend Composition

	fuel blend		
	BFG0	BFG70	BFG100
$[CH_4]$ (%v)	100	28	
$[H_2]$ (%v)		3	4
[CO] (%v)		16	22
$[CO_2]$ (%v)		16	22
$[N_2]$ (%v)		37	52
LHV (MJ/kg)	50.0	10.8	2.8

2.2. Methods. In order to analyze the combustion behavior of the premixed flames when the fuel blend and air/fuel ratio were varied, we carried out an extensive experimental campaign where several operation points were obtained at different airflow rates. Combustion regimes for each operation point were characterized by calculating their air/fuel equivalence ratio (ER), computed as the fraction between the actual and stoichiometric air/fuel ratios. Consequently, an ER higher (or lower) than 1 implies fuel-lean and air-rich (or fuel-rich and air-lean) combustion. The limits of the airflow rates were defined according to the flame stability of each fuel blend. On one side, a reduced airflow caused the flashback of the flame inside the burner mixture chamber, because of the low mixture velocities. On the other side, the highest air flows produced instability and extinction of the flame when the combustion approached its lean operation limits. Since the configuration of the burner was kept for the different blends, similarly to the industrial case, the velocities of the air/fuel mixtures are different. Thus, the ERs are limited by the burner geometry and the amount of BFG of the blend. In this way, the burner is forced to operate near its extinction and flashback working points, acquiring samples of inefficient operation conditions, whose analysis is relevant for their detection at a larger scale. With the current burner, the studied ERs vary from 1.4 to 2.0, from 1.1 to 1.9, and from 0.9 to 1.2 for BFG0, BFG70, and BFG100 fuel mixtures, respectively (see Table 3).

The burner power was fixed at 5.5 kWth for each test, independently of the fuel blend and airflow rate. Before each test set, the burner was started up for 1 h to reach a steady temperature. These temperatures were controlled on the surface of the combustion chamber with a thermocouple. Once the warming up was finished, the same procedure was followed for each combustion test. First, the fuel and air flows were adjusted. Second, chamber gases near the flame were measured and compared with the flue gases reported. Steady conditions were reached when the chamber gases and the flue gas measurements presented similar values. At this point, the spectra and images were acquired for 6 min.

Table 3. Main Characteristics of the Test Campaign

test set	BFG0	BFG70	BFG100
ER	1.4−2.0	1.1−1.9	0.9−1.2
no. of tests	7	8	5

According to previous works, the experiment duration can significantly vary between 5 and 180 s.[15,16] Thus, a conservative approach was followed to select the test period, defining it to be higher than previous references, with a value of 6 min (360 s). This way, a higher number of measurements were acquired, reducing the effect of abnormal and spurious data.

The fuel flow rate, air flow rate, and exhaust gas analyzer measurements were averaged per test. Furthermore, exhaust gas concentrations detected by the gas analyzer were corrected to 3 %v O_2. The CH_4 concentration in flue gases was measured in order to detect operation points in which unburned fuel fractions could arise from incomplete combustion.

The spectrometer and the UV−vis camera were both set in front of the quartz glass of the combustion chamber, allowing the acquisition of the flame radiation in the UV bandwidth. On the other hand, the RGB camera was installed in front of the ceramic glass to measure only the visible range. This way, the three optical devices collected spectra and images simultaneously under ambient conditions of dark lighting.

The integration time of the spectrometer and the exposure times of the cameras were selected by preliminary tests according to optimum criteria. At first, longer times are desirable to increase the signal provided by the optical devices. Nevertheless, higher exposure times may saturate sensor pixels and provide inadequate measurements. Thus, the optimum criteria were the maximizations of the integration and exposure times up to their saturation limits. Since the saturation limits of each optical device are originally unknown for an analysis of the flames, preliminary trials were performed to define them by burning BFG0 and BFG100. Furthermore, to compare measures of the same optical device between different tests and fuel blends, fixed integration and exposure times were used for all the tests. In that aspect, the integration and exposure times were defined by the tests that provide higher flame radiation, related to lower airflow rates. Consequently, the tests with lower airflow rates for BFG0 and BFG100 were carried out. Therefore, the integration and exposure times were set to 1000, 540, and 30 ms for the spectrometer and UV−vis and RGB cameras, respectively. Their values appear in Table 4, together with sampling rates, the number of samples (spectra or images) per test, and the optical device. Finally, the configuration of the spectrometer was completed by selecting a slit width of 200 μm.

Table 4. Acquisition Parameters of the Optical Devices

	optical device		
	spectrometer	UV−vis camera	RGB camera
exposure time (ms)	1000	540	30
sampling rate (Hz)	1	1.4	12
samples per test	360	504	4320

As in previous works, combustion diagnosis was performed on the basis of flame characteristics obtained by processing spectra and images of the flame. For each optical device,

https://doi.org/10.1021/acsomega.2c02103
ACS Omega 2022, 7, 24498−24510

different processing operations were defined. Previously, the signals and images were submitted to an operation based on the subtraction of the dark signals from the captured spectra and images to remove sensor electrical noise.[27,30,32]

In the case of the spectrometer, measured spectra were averaged for each test to easily characterize them through a visual representation. Nevertheless, a high amount of information is lost with this operation, since the number of spectra per test is reduced from 360 to 1. Thus, each measured spectrum was also computed individually to provide a more detailed analysis. For that purpose, a wavelength segmentation was applied, with a range of 20 nm centered at each radical wavelength being selected. Within this study, OH*, CH*, and C_2* were studied by considering their wavelengths of 310, 430, and 515 nm,[17−21] respectively, and an additional wavelength of 470 nm for C_2*.[17,19,21] CO_2* was also characterized using a wavelength of 410 nm,[18] which was contained within the CO_2* broad-band emission and was unrelated to those of other radical species. After the wavelength segmentation, 278 wavelength intensities were obtained. Finally, wavelength intensities were downsampled from 278 to 56 to reduce redundant information. The whole series of 278 wavelength intensities were split into groups of 5 wavelength intensities. Therefore, 55 groups of 5 wavelength intensities were obtained, together with a group of 3 wavelength intensities. For each one of these groups, only the first wavelength intensity was used. In this way, the wavelength resolution of the intensities was reduced from approximately 0.4 to 2 nm.

For the UV−vis and RGB images, the processing methodology was similar. On one hand, Otsu's thresholding segmentation was applied to detect flame pixels in each image channel. Otsu's method selects the threshold that maximizes the variance between the two-pixel classes, the variance being computed from the image histogram.[15,16,39] After Otsu's thresholding segmentation, the features of statistic mean[13−16,29−32] and Haralick's texture information measure of the correlation I (IMC1)[14,40,41] were computed from flame pixels. The mean is the averaged intensity value of the flame pixels, which is related to the combustion characteristics of flame brightness. On the other hand, texture features such as IMC1 are more complex to interpret in comparison to the other image features. Thus, their theoretical relationships with combustion characteristics may be unknown beforehand. Nevertheless, IMC1 has been used together with other color and texture features to characterize primary air flow and secondary air to territory air split.[14] Furthermore, other Haralick features have been used to characterize O_2 and NO_x content in flue gases.[33] In this way, dependences between the combustion characteristics and IMC1 (or other related texture features) have been empirically reported. When Otsu's thresholding segmentation is applied, a small number of flame pixels could be separated from the main contour of the flame and distort the values of the geometrical features. In order to discard these pixels, the morphological transformation of erosion was applied using a kernel of 3 × 3 pixels.[42]

Next to morphological erosion, the features of the geometrical area and centroid vertical coordinate were extracted from the binary images.[15,31,35,43] The area is the number of flame pixels related to the flame area. The centroid vertical coordinate is the vertical coordinate of the flame mass center. This feature is related to the distance between the burner and the flame and the flame length.

After the image features were computed, a total of 4 characteristics were obtained per image channel, resulting in 4 and 12 characteristics for the UV−vis and RGB cameras. Table 5 gathers the 4 channel characteristics and their mathematical

Table 5. Image Features Per Channel Considered

feature no.	type	feature	equation	ref
1	statistic	mean (μ)	$\frac{1}{P}\sum_{p=1}^{P} x(p)$	16, 29, 30
2	texture	information measure of correlation I (f_{12}, IMC1)	$\frac{HXY - HXY1}{\max(HX, HY)}$	40, 41
3	geometrical	area (a)	$\sum_{r=1}^{R}\sum_{c=1}^{C} b(c, r)$	15, 31
4	geometrical	centroid vertical coordinate (c_y)	$\frac{\sum_{r=1}^{R}\sum_{c=1}^{c} b(c, r)}{a}$	35, 43

expressions, referenced to a grayscale image of P pixels, with $x(p)$ denoting the grayscale value of the pixel p. For the texture IMC1, the element located in row i and column j of a normalized gray-level co-occurrence matrix (GLCM) is referred to as $p(i,j)$. The GLCM has N rows and N columns, where N is the number of distinct gray values in the grayscale image. Additional variables are used to compute the texture features, which appear in Table 6. In the case of the

Table 6. Additional Variables and Their Equations to Compute the Texture Image Features of IMC1

variable	equation	ref
$p_x(i)$	$\sum_{j=1}^{N} p(i, j)$	40, 41
HX	$-\sum_{i=1}^{N} p_x(i) \log p_x(i)$	
HY	$-\sum_{i=1}^{N} p_y(i) \log p_y(i)$	
HXY	$-\sum_{i=1}^{N} p(i, j) \log p(i, j)$	
$HXY1$	$-\sum_{i=1}^{N}\sum_{j=1}^{N} p(i, j) \log[p_x(i)p_y(j)]$	

geometrical features, the binary image also has P pixels (with R rows and C columns), and the binary value (0 or 1) of a pixel p located in column c and row r is denoted $b(c,r)$.

In order to compute the processing operations for the spectra and images of the tests, a specific code was developed using the programming language of Python (version 3.7). Furthermore, the developed code also used the libraries of OpenCV, NumPy, SciPy, Mahotas, and Pandas. An additional code was written to automatically read the spectra and images acquired during the experimental campaign, which filtered them according to the characteristics of the tests.

https://doi.org/10.1021/acsomega.2c02103
ACS Omega 2022, 7, 24498−24510

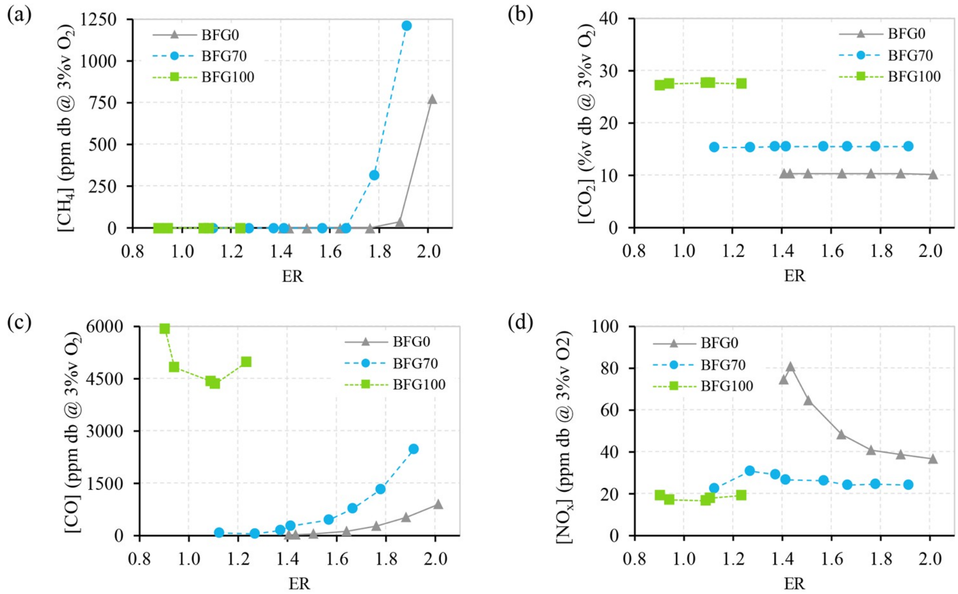

Figure 3. Concentration in the flue gases of (a) CH_4, (b) CO_2, (c) CO, and (d) NO_x, for the fuel blends BFG0, BFG70, and BFG100.

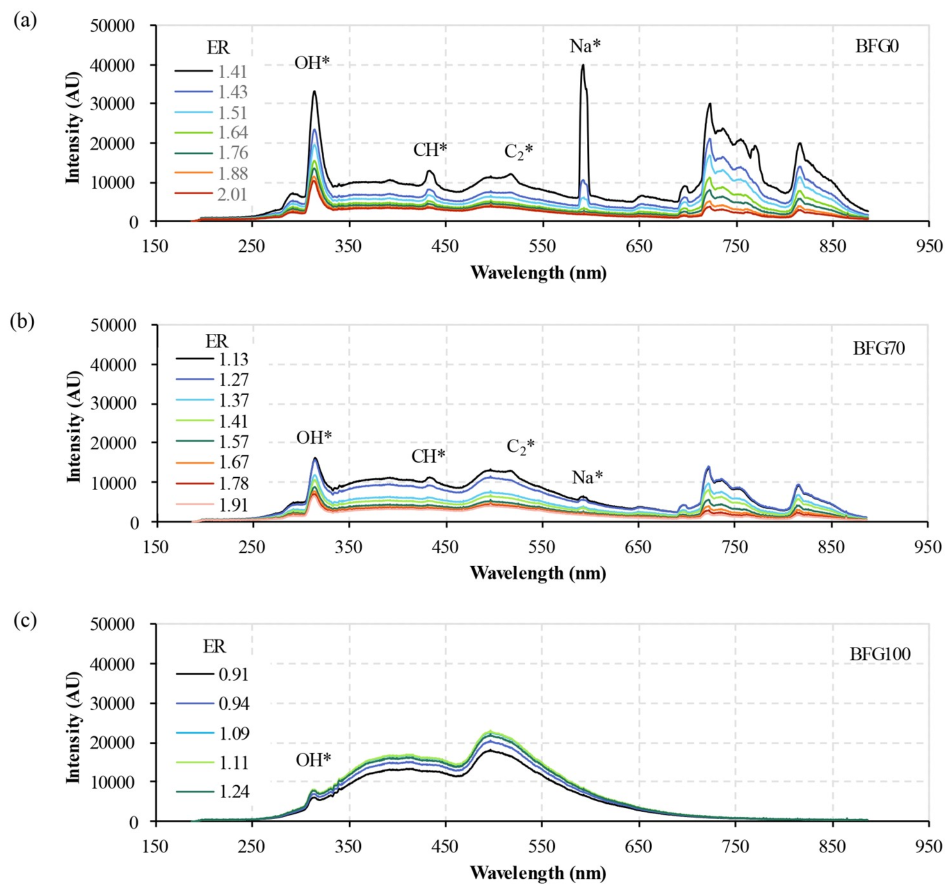

Figure 4. Average spectra for the fuel blends (a) BFG0, (b) BFG70, and (c) BFG100, with different ERs.

3. RESULTS AND DISCUSSION

3.1. Analysis of Pollutant Emissions.

The first analysis of the test data is focused on the pollutant emissions of CH_4, CO_2, CO, and NO_x, whose trends are shown in Figure 3.

Complete combustion is achieved for most BFG0 and BFG70 operation points, since no CH_4 is measured in flue gases (Figure 3a). However, a non-negligible CH_4 concentration is detected at higher ERs (over 1.7) for these fuel blends, most probably caused by unburned CH_4, a constituent of BFG0 and BFG70. Additionally, CH_4 emissions are higher for BFG70 than for pure CH_4. In these cases, the test burner presents some combustion instability due to the higher velocity

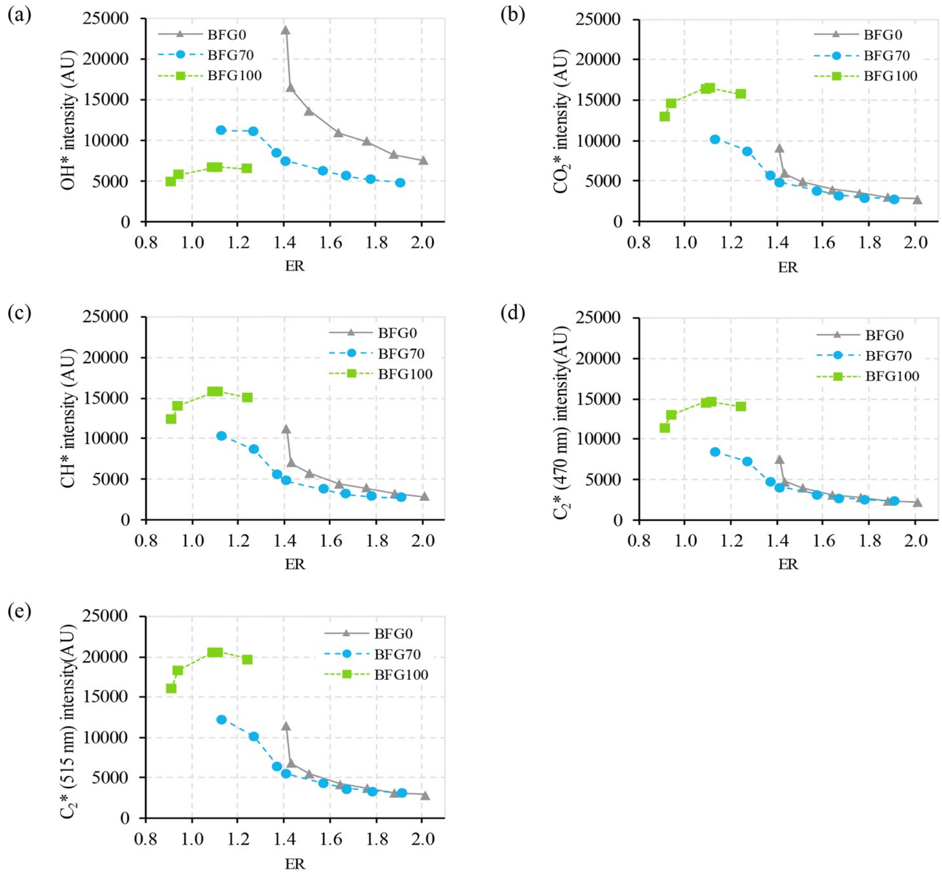

Figure 5. Intensities of (a) OH*, (b) CO_2*, and (c) CH* and of C_2* at (d) 470 nm and (e) 515 nm versus ER, for the fuel blends BFG0, BFG70, and BFG100.

of the air/fuel mixture, which prevents the proper burning of the fuel.

Figure 3b shows CO_2 emissions for the different operation points. These emissions have different sources depending on the fuel blend. In the case of BFG0, CO_2 emissions correspond to the completely oxidated CH_4. For BFG100, CO_2 emissions have two sources: the combustion of CO and the original CO_2 included in the fuel blend. Finally, the mixture BFG70 presents CO_2 emissions originating from the three previous sources (combustion of CH_4 and CO and CO_2 from fuel).

In this way, the effect of each source is modified with different BFG shares in the fuel blend. With an increase in BFG share in the fuel blend, higher CO_2 emissions are generated from CO combustion and the CO_2 composition of the fuel. At the same time, lower CO_2 emissions originate from CH_4 combustion. According to BFG measurements, total CO_2 emissions are higher when the share rises from 0 to 70 %v. Consequently, CO combustion and CO_2 composition of the fuel exceed the effect of CH_4 combustion in CO_2 emissions. As expected, a constant trend is observed when CO_2 emissions of the same fuel blend are compared for different ERs, due to the operation with a fixed thermal power for all of the tests.

The CO concentration in the exhaust gases is included in Figure 3c. In general, CO emissions are increased when the BFG share of the fuel blend is raised. This effect is due to a higher CO content in the fuel blend, higher air/fuel velocities, and lower calorific value (higher inert content). For each fuel blend, lower CO emissions are obtained at points closer to the stoichiometric point. The conditions of fuel excess (ER < 1) led to an increase in CO emissions because part of the fuel is not burned due to the absence of O_2. In the same way, high ER conditions generate combustion instability because of the air dilution. Part of the CH_4 of BFG0 is unburned and part of the CO of BFG100 and BFG70 is unburned, causing an increase in CO emissions.

Trends of NO_x emissions are included in Figure 3d. NO_x emissions are highly dependent on the flame temperature and the availability of N_2 to be oxidized.[44] Higher shares of CH_4 in the fuel blend increase the adiabatic flame temperature over 1800 K, for which the Zeldovich mechanism dominates NO_x emissions, where the flame temperature and residence time are important factors.

On the other hand, a fuel blend of BFG without CH_4 (such as BFG0) does not reach 1800 K, and NO_x emissions are reduced. This behavior is also reported in the work of Zheng et al.[6]

In addition to previous effects, NO_x emissions are decreased in the combustion of BFG0 for higher ERs, since the air acts as a diluent. The effect of the dilution is significant in the case of pure CH_4, which implies a significant reduction in NO_x at high equivalence ratios.[45] However, the mixtures BFG70 and BFG100 have high concentrations of diluents such as CO_2 and N_2, which receive part of the energy of the combustion. This effect causes lower combustion temperatures, and therefore, the concentration of NO_x in the flue gases is significantly lower and the effect of the increase of air is not significant.[4]

3.2. Analysis of Chemiluminescence Spectroscopy. An analysis with chemiluminescence spectroscopy was performed to compare intensities and wavelengths of the energy radiated by the premixed flame radicals. The spectrometer captured the radiant energies emitted by the flame, which were averaged for each test. Figure 4 presents the averaged spectra of BFG0, BFG70, and BFG100 for different ERs.

The BFG0 spectra, measured as a reference, show their signature shape, with the intensity peaks of OH*, CH*, and C_2* at 310, 430, and 470−515 nm, respectively. Nevertheless, other patterns of high intensities appear in the mean spectrum. The peak at around 589 nm is the typical emission band of Na*, which in previous works has been linked to the combustion of impurities from traces.[19,46,47] Also, several peaks above 700 nm (visible and infrared range) could be related to the emission of the burner surface,[17] HNO* (between 650 and 900 nm),[45,46] and vibrational−rotational transitions of diatomic molecules with hydrogen, as CH (from 813 to 847 nm), OH (from 834 to 845 nm), or H_2O (from 892 to 967 nm).[46] Additionally, the peaks measured between 700 and 800 nm are similar to the results of Parameswaran et al. for hydrocarbon flames with a premixed burner.[48]

On the other hand, flame spectra obtained with BFG100 have a higher and dominant contribution from the broad-band CO_2* emission due to the CO_2 content of the BFG. Since the BFG composition does not include CH_4, CH* (430 nm) and C_2* (470 and 515 nm) peaks are not detected. Nonetheless, the peak of OH* (310 nm) is still detected due to the H_2 content in the BFG, but its intensity is lower than that for BFG0. This trend is also reported in the work of Zheng et al.,[6] in which the OH concentration is increased when CH_4 is added to BFG.

The spectra of BFG70 contains characteristics of the other two fuel blends. The BFG in the fuel blend provides a broad-band CO_2* emission of intensity lower than that in the case of BFG100 due to the higher concentration of BFG. CH* and C_2* peaks are detected due to the CH_4 of BFG70, and the measured peak of OH* is related to both CH_4 and H_2. These narrow-band emissions show intensities lower than those in the case of BFG0 due to the lower concentration of CH_4 in the fuel blend.

For each fuel type, the intensity throughout the whole bandwidth depends on the air/fuel ratio (ER). For BFG0 and BFG70, whose conditions are fuel-lean (air-rich), the emission intensity increases as the combustion air decreases. For BFG100, higher intensities are measured at medium air/fuel ratios. Nevertheless, these trends of the emission intensities with the air/fuel ratio for the three fuel blends can be described together using the ER values. For the three fuel blends, the maximum emission intensity could be measured at an ER around 1.0 (stoichiometric conditions), as in the case of BFG100, which has a maximum intensity for the ER of 1.1. Consequently, the emission intensity is reduced with an increase in the difference between the actual ER and the ER of 1.1 for BFG100. This relationship is also repeated for BFG0 and BFG70, where the emission intensity increases as the difference between the actual ER and the ER of 1.1 is reduced.

The intensities of OH*, CO_2*, CH*, and C_2* are shown in Figure 5 for BFG0, BFG70, and BFG100. The general trend detected in the average spectra is repeated by the radical emissions, which increase when the ER approaches 1.1. In particular, these behaviors of the OH* and CO_2* intensities around an ER of 1.0 have also been reported in previous studies. In the work of Ahmadi et al.,[49] the OH* emission intensity had a maximum at an ER of 0.8 for NG flames in a premixed burner of domestic heating boilers. Related to the work of Ahmadi et al.,[49] the Soltanian et al.[17] detected a peak of the intensities of OH* and CO_2* at an ER of 0.8 for NG flames and a premixed gas boiler burner. Additionally, Ding et al.[50] detected a maximum of OH* intensity at an ER of 1.0 for flames of different fuel blends (pure CH_4 and mixtures of CH_4 with N_2, CO_2, H_2, and C_3H_8) in a burner similar to those in the studies referenced above.

All of the radical intensities of BFG0 are slightly higher than those of BFG70 at similar ERs. The addition of CO_2 in BFG70 increases the broad-band CO_2* emission with respect to the BFG0 case due to the increase in the BFG share. However, the reduction of the CH_4 concentration decreases the emission intensity of OH*, CH*, and C_2* (at both 470 and 515 nm). When the concentration of BFG in the fuel blend is increased to 100%, the broad-band CO_2* emission also increases, increasing the intensities radiated in its range (between 350 and 600 nm). This behavior matches with the trends shown for the intensities of CO_2*, CH*, and C_2*, which are higher for BFG100 than for BFG70, at similar ERs. The emission intensity of OH* is not affected by the increase of broad-band CO_2* emission, since 310 nm is not in the range between 350 and 600 nm. In particular, the emission intensity of OH* was reduced for BFG100 with regard to BFG70 at similar ERs, showing a trend in contrast with the rest of the radicals due to the different compositions of the fuel blends. In this study, the intensity of OH* is related to the reaction of CH_4 and H_2 (included in the composition of the BFG). While BFG70 includes both CH_4 and H_2, BFG100 has a higher concentration of H_2 but no CH_4. This higher concentration of H_2 does not balance the lack of CH_4, providing a lower emission at 310 nm in comparison to that for BFG70.

OH* measurements are also related to CO and CO_2 emissions through the reaction CO + OH = CO_2 + H, fundamental for CO oxidation.[51] With this reaction, if the OH concentration is decreased, CO emissions are expected to increase. This behavior is shown by comparing parts a and c of Figure 5, in which OH* radiation and CO emissions are inversely proportional.

3.3. Analysis of the Flame Images. After the spectral features were studied, images acquired with the cameras were analyzed. Figure 6 shows different flames captured for the three fuels with the UV−vis and RGB cameras under similar conditions.

Features extracted from the 310 nm images show dependences on the fuel blend and ER, independent of the feature type (statistical, texture, or geometrical), which can be seen in Figure 7. Among the 310 nm image features, the statistical mean has a stronger dependence on the combustion regimes for BFG0 and BFG70.

The mean is reduced with an increase in the BFG (reduction of CH_4) share in the fuel blend. In the tests, there are two sources for OH*: CH_4 hydrocarbons and BFG hydrogen. Since the substitution of CH_4 with BFG reduces the average combustion radiation, CH_4 hydrocarbons may make a greater contribution than BFG hydrogen. Furthermore, the mean increases for the same fuel blend when the ER approaches 1.1. Similar behavior has also been shown in previous works.[17,48,49]

Despite the different natures between the mean (statistical) and IMC1 (texture), the overall trends highlighted for the

https://doi.org/10.1021/acsomega.2c02103
ACS Omega 2022, 7, 24498−24510

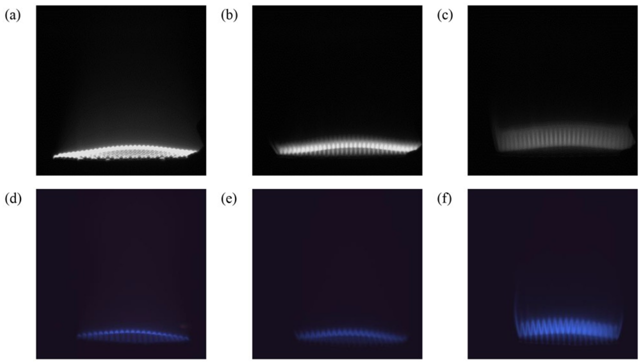

Figure 6. Sample images captured by the UV−vis camera with the 310 nm filter for (a) BFG0, (b) BFG70 and (c) BFG100 and by the RGB camera for (d) BFG0, (e) BFG70, and (f) BFG100, with ERs of 1.2 and 1.4 (fuel-lean and air-rich).

mean are shared for the IMC1. Thus, the flame texture is also related to the BFG share in the fuel blend and the ER.

Finally, the centroid vertical coordinate is increased by raising the BFG share in the fuel blend. The increase in BFG share increases the length of the flame front, and thus, higher centroid vertical coordinates are measured. The increase in the flame front length may be caused by the higher fuel flows used when the BFG share is increased. Within the same fuel, similar behavior is found when the ER is increased. This effect could be related to the air flow increase, which extends the flame front. In addition, the geometrical vertical coordinate of the centroid (c_y) has a higher relevance for the classification of the fuel blends, since most values of the feature are only related to one specific fuel blend, independently of the ER. For example, a flame image with an unknown ER could be related to BFG0 (if c_y is higher than or equal to 835-pixel rows), BFG70 (c_y between 835- and 790-pixel rows) or BFG 100 (if c_y is equal to or lower than 790-pixel rows).

A similar study was carried out for the RGB images. For the 310 nm images, the statistical mean and geometrical area show trends with the fuel blend and ER. In addition, these dependences can be observed independently of the color channel, and some features such as the statistical mean share its behavior for the three channels (Figure 8).

The mean values are higher for the blue channel and lower for the red channel, while the green channel presents intermediate values. This trend is due to the radiation differences in the spectral sensitivity of each color channel. Nevertheless, the mean shows the same behavior with respect to fuel blend and ER, independently of the color channel. BFG0 and BFG70 have similar values, and therefore, the flame intensity does not differ significantly. For BFG100, the mean (and thus, the flame intensity) is higher due to the significant contribution of the broad-band CO_2* emission. With regard to the behavior of the mean with the ER, the mean increases when the ER approaches 1.1, as for the 310 nm images.

The areas are similar for the green and blue channels, but it differs for the red channel. As with the mean, these variations between channels are related to the different spectral sensitivities of the color channels. The area for the red channel shows almost no dependence on the fuel blend and ER; only extreme ERs of the BFG0 show significant differences. With those ERs, the length of the red flame is increased, and thus, the area as well. For the green and blue channels, an increase in the BFG share increases the flame length, due to a higher fuel flow. For each fuel, higher ERs result in higher areas since the fuel flow is constant and the airflow is increased. Notable exceptions are lower ERs of BFG0, for which the flame length is slightly increased. Among all image features, the geometrical area of the blue channel is of greater interest due to its stronger relationship with the fuel blends and combustion regimes, as seen in Figure 8f.

3.4. Coupled Analysis of the Optical Devices. Chemiluminescence spectra, UV filtered images, and color

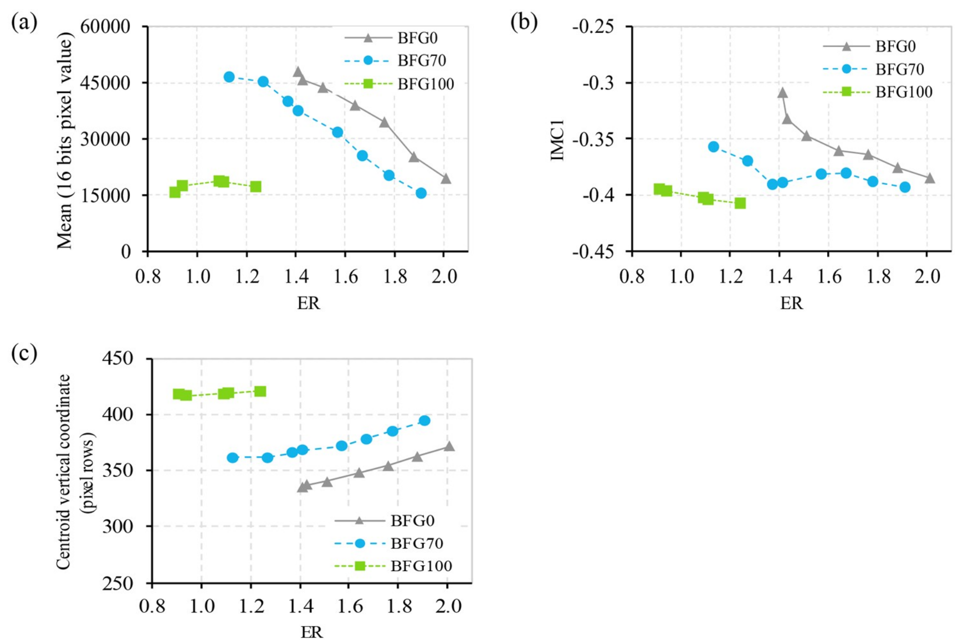

Figure 7. Image features of (a) statistical mean, (b) texture IMC1, and (c) geometrical centroid vertical coordinate versus ER, for the 310 nm (OH*) images of BFG0, BFG70, and BFG100.

https://doi.org/10.1021/acsomega.2c02103
ACS Omega 2022, 7, 24498−24510

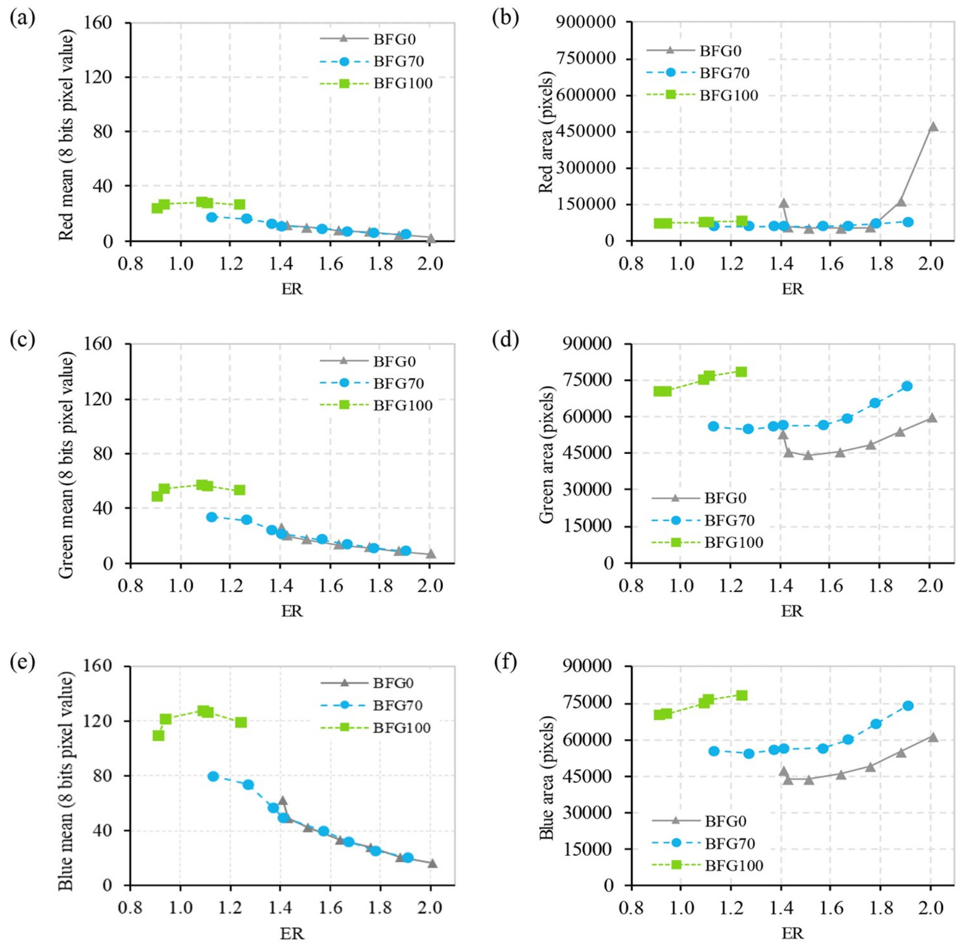

Figure 8. Image features of (a) red statistical mean, (b) red geometrical area, (c) green statistical mean, (d) green geometrical area, (e) blue statistical mean, and (f) blue geometrical area versus ER, for the RGB images of BFG0, BFG70, and BFG100.

images were processed to extract different features. The relationships of these features with the combustion characteristics were analyzed in previous sections. Now, features measured with different optical devices are compared together to study their correlations.

First, chemiluminescence spectra and UV filtered images were studied. The OH* spectral intensity (Figure 5a) and image mean (Figure 7a) share similar trends with regard to the fuel composition and ER. In the captured trends, the feature values decrease when the ER is increased for BFG0 and BFG70, and higher values are measured at equal ERs for lower shares of BFG in the fuel blend. This behavior is expected for the OH* spectral intensity and image mean, since they are related to the same combustion characteristic (magnitude of the flame radiated energy). On the other hand, the image IMC1 (Figure 7b) and centroid vertical coordinate (Figure 7c) characterize the spatial texture and geometry of the flame radiated energy, instead of its magnitude. In this way, these features could have different trends with the combustion characteristics. Nevertheless, the image IMC1 also shows a similar trend with the fuel composition and ER. In addition, the image centroid vertical coordinate (Figure 7c) has an inverse relationship with the fuel composition and ER with respect to previous optical features.

Color images capture flame radiated energy in broad-band ranges instead of the narrow-band range used by the UV filtered images. These broad-band ranges are 580−800 nm (red channel), 475−600 nm (green) and 400−500 nm (blue). Spectral intensities (Figure 4) and image means (Figure 8a,c,e) characterize the magnitude of the flame radiated energy. Trends of these features with combustion characteristics differ from previous trends. While the feature values still decrease with an ER increase, similar values are measured at equal ERs for BFG0 and BFG70.

Moreover, the values for BFG100 are higher than those for BFG0 and BFG70. This behavior is due to the measurement of the radiation in broad-band instead of narrow-band ranges. The three color channels capture broad-band CO_2* radiation, emitted between 350 and 610 nm. This radiation is increased with an increase in the BFG share in the fuel blend, which increases the CO_2 fraction. Consequently, feature values for BFG70 and BFG100 are increased. On the other hand, image areas show inverse trends with respect to the previous features. These relationships with combustion characteristics are shared with the image area of the UV filtered images.

4. CONCLUSIONS

In this work, BFG, CH_4, and a mixture with 70% of BFG and 30% of CH_4 have been tested in a laboratory burner at different air/fuel equivalence ratios, at a fixed thermal power of 5.5 kW. An analysis of chemiluminescence spectra, filtered UV images, and color images enables the extraction of relevant features from the flames. These parameters can be used to

https://doi.org/10.1021/acsomega.2c02103
ACS Omega 2022, 7, 24498−24510

characterize aspects of the combustion in terms of fuel mixture, ER, and flue gas composition.

The main conclusions from the results of this work are as follows.

- Together with the mixture and air/fuel equivalence ratio, the test burner used during the tests strongly influenced the pollutant emissions. The use of fuels with significant differences in their calorific value and the same ducts and burner header produced different velocities of the air/fuel mixture and thus affected the quality of the mixture. This caused in some cases, with high velocities, the mixture left the combustion chamber without being burned. As a result, the CO concentration in flue gases increased at high air equivalence ratios for all of the fuel blends and the CH_4 concentration also increased for BFG0 and BFG70. When the combustion conditions were more favorable, pollutant concentrations exhibited the expected trends with ER.
- Chemiluminescence spectroscopy revealed that BFG100 shows a signature spectrum with the primary broad-band emission of CO_2* due to the higher CO_2 concentration of the fuel, whereas BFG0 spectra agree with the classical spectra reported in the literature. The partial substitution of CH_4 with BFG provides a hybrid spectrum between BFG100 and BFG0. For all of the fuel blends, spectrumal intensities increased with ERs of closer to 1.1. The dilution caused by the excess air for BFG0 and BFG70 caused a decrease in the spectral intensity, and the different peaks associated with the combustion radicals were attenuated.
- The extracted image features show trends with fuel blends and ERs that coincide with the spectroscopy results for the same range of wavelengths. All types of image features considered (statistical, geometrical, and texture) show relationships with the combustion conditions, and some of them share a stronger dependence, such as statistical mean, texture IMC1, and geometrical vertical coordinate of the centroid.
- The images captured with the RGB camera also showed trends similar to those of spectroscopy and UV filtered images. As with the UV filtered images, color image features of statistical, texture, and geometrical types show dependences on the BFG concentration and ER. Furthermore, these relationships are provided by all the color channels, highlighting the strong dependences of the statistical mean and geometrical area.

The current study has addressed uncertainties and challenges related to the innovation of the considered BFG valorization. The results have shown strong dependences of the computed spectra and image features related to intensity, texture, and geometry on the BFG concentration and ER. Thus, promising alternatives have been provided for the monitoring and control of BFG cofiring, allowing further research in applications, with the adaptation and optimization of artificial intelligence techniques to develop predictive combustion models.

AUTHOR INFORMATION

Corresponding Author

Jorge Arroyo − *CIRCE, 50018 Zaragoza, Spain;* orcid.org/0000-0003-3157-6267; Phone: +34 976 976 859; Email: jarroyo@fcirce.es

Authors

Pedro Compais − *CIRCE, 50018 Zaragoza, Spain*

Ana González-Espinosa − *CIRCE, 50018 Zaragoza, Spain*

Miguel Ángel Castán-Lascorz − *CIRCE, 50018 Zaragoza, Spain*

Antonia Gil − *Department of Mechanical Engineering, University of Zaragoza, 50018 Zaragoza, Spain*

Complete contact information is available at: https://pubs.acs.org/10.1021/acsomega.2c02103

Notes

The authors declare no competing financial interest.

ACKNOWLEDGMENTS

This work has been supported by the European Union's Horizon 2020 Research and Innovation Programme under Grant Agreement No. 820771 (BAMBOO project).

ABBREVIATIONS

AU, arbitrary units; BFG, blast furnace gas; DAQ, data acquisition; EMCCD, electron multiplying charge-coupled device; ER, equivalence ratio; GLCM, gray level co-occurrence matrix; HSI, hue. saturation, and intensity; IMC1, information measure of correlation I; IR, infrared; LHV, lower heating value; NDIR, nondispersive infrared; NG, natural gas; RGB, red−green−blue; UV, ultraviolet; vis, visible

REFERENCES

(1) Larrinaga, P.; Campos-Celador, A.; Legarreta, J.; Diarce, G. Evaluation of the Theoretical, Technical and Economic Potential of Industrial Waste Heat Recovery in the Basque Country. *J. Clean. Prod.* **2021**, *312*, 127494.

(2) Wang, X.; Li, C.; Lam, C. H.; Subramanian, K.; Qin, Z. H.; Mou, J. H.; Jin, M.; Chopra, S. S.; Singh, V.; Ok, Y. S.; Yan, J.; Li, H. Y.; Lin, C. S. K. Emerging Waste Valorisation Techniques to Moderate the Hazardous Impacts, and Their Path towards Sustainability. *J. Hazar. Mater.* **2022**, *423*, 127023.

(3) Pierri, E.; Hellkamp, D.; Thiede, S.; Herrmann, C. Enhancing Energy Flexibility through the Integration of Variable Renewable Energy in the Process Industry. *Proc. CIRP* **2021**, *98*, 7−12.

(4) Cuervo-Piñera, V.; Cifrián-Riesgo, D.; Nguyen, P. D.; Battaglia, V.; Fantuzzi, M.; della Rocca, A.; Ageno, M.; Rensgard, A.; Wang, C.; Niska, J.; Ekman, T.; Rein, C.; Adler, W. Blast Furnace Gas Based Combustion Systems in Steel Reheating Furnaces. *Energy Procedia* **2017**, *120*, 357−364.

(5) Zheng, W.; Pang, L.; Liu, Y.; Xie, F.; Zeng, W. Effects of Initial Condition and Fuel Composition on Laminar Burning Velocities of Blast Furnace Gas with Low Heat Value. *Fuel* **2021**, *289*, 119775.

(6) Zheng, W.; Pang, L.; Liu, Y.; Xie, F.; Zeng, W. Effects of Methane Addition on Laminar Flame Characteristics of Premixed Blast Furnace Gas/Air Mixtures. *Fuel* **2021**, *302*, 121100.

(7) Zhang, L.; Xie, W.; Ren, Z. Combustion Stability Analysis for Non-Standard Low-Calorific Gases: Blast Furnace Gas and Coke Oven Gas. *Fuel* **2020**, *278*, 118216.

(8) Caillat, S. Burners in the Steel Industry: Utilization of by-Product Combustion Gases in Reheating Furnaces and Annealing Lines. *Energy Procedia* **2017**, *120*, 20−27.

(9) European Commission, Directorate-General for Research and Innovation; Battaglia, V.; Niska, J.; Cuervo Piñera, V., et al. *High Efficiency Low NOX BFG Based Combustion Systems in Steel Reheating Furnaces (HELNOx-BFG)*: Final Report, 2018.

(10) Huang, H. W.; Zhang, Y. Digital Colour Image Processing Based Measurement of Premixed CH 4 + Air and C2H4 + Air Flame Chemiluminescence. *Fuel* **2011**, *90* (1), 48−53.

(11) He, L.; Guo, Q.; Gong, Y.; Wang, F.; Yu, G. Investigation of OH* Chemiluminescence and Heat Release in Laminar Methane-

Oxygen Co-Flow Diffusion Flames. *Combust. Flame* **2019**, *201*, 12−22.

(12) Tripathi, M. M.; Krishnan, S. R.; Srinivasan, K. K.; Yueh, F. Y.; Singh, J. P. Chemiluminescence-based multivariate sensing of local equivalence ratios in premixed atmospheric methane-air flames. *Fuel* **2012**, *93*, 684−691.

(13) González-Espinosa, A.; Gil, A.; Royo-Pascual, L.; Nueno, A.; Herce, C. Effects of Hydrogen and Primary Air in a Commercial Partially-Premixed Atmospheric Gas Burner by Means of Optical and Supervised Machine Learning Techniques. *Int. J. Hydrogen Energy* **2020**, *45* (55), 31130−31150.

(14) Bai, X.; Lu, G.; Hossain, M. M.; Szuhánszki, J.; Daood, S. S.; Nimmo, W.; Yan, Y.; Pourkashanian, M. Multi-Mode Combustion Process Monitoring on a Pulverised Fuel Combustion Test Facility Based on Flame Imaging and Random Weight Network Techniques. *Fuel* **2017**, *202*, 656−664.

(15) Katzer, C.; Babul, K.; Klatt, M.; Krautz, H. J. Quantitative and Qualitative Relationship between Swirl Burner Operating conditions and Pulverized Coal Flame Length. *Fuel Process. Technol.* **2017**, *156*, 138−155.

(16) Mathew, A. P.; Asokan, A.; Batri, K.; Sivakumar, D. Comparative Analysis of Flame Image Features for Combustion Analysis. *Indian J. Sci. Technol.* **2016**, *9* (6), 1−11.

(17) Soltanian, H.; Targhi, M. Z.; Pasdarshahri, H. Chemiluminescence Usage in Finding Optimum Operating Range of Multi-Hole Burners. *Energy* **2019**, *180*, 398−404.

(18) Quintino, F. M.; Trindade, T. P.; Fernandes, E. C. Biogas Combustion: Chemiluminescence Fingerprint. *Fuel* **2018**, *231*, 328−340.

(19) Chong, C. T.; Hochgreb, S. Flame Structure, Spectroscopy and Emissions Quantification of Rapeseed Biodiesel under Model Gas Turbine Conditions. *Appl. Energy* **2017**, *185*, 1383−1392.

(20) Merotto, L.; Sirignano, M.; Commodo, M.; D'Anna, A.; Dondè, R.; de Iuliis, S. Experimental Characterization and Modeling for Equivalence Ratio Sensing in Non-Premixed Flames Using Chemiluminescence and Laser-Induced Breakdown Spectroscopy Techniques. *Energy Fuels* **2017**, *31* (3), 3227−3233.

(21) Giassi, D.; Cao, S.; Bennett, B. A. v.; Stocker, D. P.; Takahashi, F.; Smooke, M. D.; Long, M. B. Analysis of CH* Concentration and Flame Heat Release Rate in Laminar Coflow Diffusion Flames under Microgravity and Normal Gravity. *Combust. Flame* **2016**, *167*, 198−206.

(22) Guiberti, T. F.; Durox, D.; Schuller, T. Flame Chemiluminescence from CO_2- and N_2-Diluted Laminar CH_4/Air Premixed Flames. *Combust. Flame* **2017**, *181*, 110−122.

(23) Huang, H. W.; Zhang, Y. Imaging Based Chemiluminescence Characterisation of Partially Premixed Syngas Flames through DFCD Technique. *Int. J. Hydrogen Energy* **2013**, *38* (11), 4839−4847.

(24) Deng, K.; Zhong, Y.; Wang, M.; Zhong, Y.; Luo, K. H. Effects of Acoustic Excitation on the Combustion Instability of Hydrogen-Methane Lean Premixed Swirling Flames. *ACS Omega.* **2020**, *5*, 8744−8753.

(25) Huang, M.; Xiao, Y.; Zhang, Z.; Shao, W.; Xiong, Y.; Liu, Y.; Liu, Z.; Lei, F. Effect of Air/Fuel Nozzle Arrangement on the MILD Combustion of Syngas. *Appl. Therm. Eng.* **2015**, *87*, 200−208.

(26) Liu, Y.; Tan, J.; Wan, M.; Zhang, L.; Yao, X. Quantitative Measurement of OH* and CH* Chemiluminescence in Jet Diffusion Flames. *ACS Omega.* **2020**, *5*, 15922−15930.

(27) Wang, J.; Chang, M.; Zhang, M.; Li, G.; Chen, S.; Huang, Z. Flame front identification and its effect on turbulent premixed flames topology at high pressure. *Exp. Therm Fluid Sci.* **2019**, *107*, 107−117.

(28) Wu, R.; Xie, F.; Wei, J.; Song, X.; Yang, H.; Lv, P.; Yu, G. Study on Soot Emission Characteristics of Methane/Oxygen Inverse Diffusion Flame. *ACS Omega.* **2021**, *6*, 23191−23202.

(29) González-Cencerrado, A.; Peña, B.; Gil, A. Experimental Analysis of Biomass Co-Firing Flames in a Pulverized Fuel Swirl Burner Using a CCD Based Visualization System. *Fuel Process. Technol.* **2015**, *130*, 299−310.

(30) González-Cencerrado, A.; Gil, A.; Peña, B. Characterization of PF Flames under Different Swirl Conditions Based on Visualization Systems. *Fuel* **2013**, *113*, 798−809.

(31) Sun, D.; Lu, G.; Zhou, H.; Li, X.; Yan, Y. A Simple Index Based Quantitative Assessment of Flame Stability. *2013 IEEE Int. Conf. Imaging Syst. Technol. Proc. (IST)* **2013**, 190−193.

(32) González-Cencerrado, A.; Peña, B.; Gil, A. Coal Flame Characterization by Means of Digital Image Processing in a Semi-Industrial Scale PF Swirl Burner. *Appl. Energy* **2012**, *94*, 375−384.

(33) Yang, G.; He, Y.; Li, X.; Liu, H.; Lan, T. Gabor-GLCM-Based Texture Feature Extraction Using Flame Image to Predict the O_2 Content and NO_x. *ACS Omega* **2022**, *7*, 3889−3899.

(34) Liu, Y.; Xue, Q.; Zuo, H.; Yang, F.; Peng, X.; Wang, J. Effects of CH_4 and N_2 Dilution on the Combustion Characteristics of H_2/CO Mixture in a Turbulent, Partially Premixed Burner. *ACS Omega* **2021**, *6*, 15651−15662.

(35) Hanuschkin, A.; Zündorf, S.; Schmidt, M.; Welch, C.; Schorr, J.; Peters, S.; Dreizler, A.; Böhm, B. Investigation of Cycle-to-Cycle Variations in a Spark-Ignition Engine Based on a Machine Learning Analysis of the Early Flame Kernel. *Proc. Combust. Inst.* **2021**, *38*, 5751−5759.

(36) Sun, D.; Lu, G.; Zhou, H.; Yan, Y.; Liu, S. Quantitative Assessment of Flame Stability Through Image Processing and Spectral Analysis. *IEEE Trans. Instrum. Meas.* **2015**, *64* (12), 3323−3333.

(37) Luo, C.; Yu, Z.; Wang, Y.; Ai, Y. Experimental Investigation of Lean Methane-Air Laminar Premixed Flames at Engine-Relevant Temperatures. *ACS Omega* **2021**, *6*, 17977−17987.

(38) Vargas, A. C.; García, A. M.; Arrieta, C. E.; Del Rio, J. S.; Amell, A. Burning Velocity of Turbulent Methane/Air Premixed Flames in Subastmospheric Environments. *ACS Omega* **2020**, *5*, 25095−25103.

(39) Otsu, N. A Threshold Selection Method from Gray-Level Histograms. *IEEE Trans. Syst. Man Cybern.* **1979**, *9* (1), 62−66.

(40) Haralick, R. M.; Shanmugam, K.; Dinstein, I. Textural Features for Image Classification. *IEEE Trans. Syst. Man Cybern.* **1973**, *SMC-3* (6), 610−621.

(41) Brynolfsson, P.; Nilsson, D.; Torheim, T.; Asklund, T.; Karlsson, C. T.; Trygg, J.; Nyholm, T.; Garpebring, A. Haralick Texture Features from Apparent Diffusion Coefficient (ADC) MRI Images Depend on Imaging and Pre-Processing Parameters. *Sci. Rep.* **2017**, *7* (1), 4041.

(42) Sreedhar, K. Enhancement of Images Using Morphological Transformations. *Int. J. Comput. Sci. Inf. Technol.* **2012**, *4* (1), 33−50.

(43) Zhao, Z.; Hui, M.; Liu, M.; Dong, L.; Liu, X.; Zhao, Y. Centroid Shift Analysis of Microlens Array Detector in Interference Imaging System. *Opt. Commun.* **2015**, *354*, 132−139.

(44) Blauwens, J.; Smets, B.; Peeters, J. Mechanism of "Prompt" NO Formation in Hydrocarbon Flames. *Symp. (Int.) Combust.* **1977**, *16* (1), 1055−1064.

(45) Cho, E. S.; Chung, S. H. Numerical evaluation of NOx mechanisms in methane-air counterflow premixed flames. *J. Mech. Sci. Technol.* **2009**, *23*, 659−666.

(46) Sheehe, S. L.; Jackson, S. I. Identification of Species from Visible and Near-Infrared Spectral Emission of a Nitromethane-Air Diffusion Flame. *J. Mol. Spectrosc.* **2019**, 364.

(47) Toro, C.; Torres, S.; Parra, V.; Fuentes, R.; Castillo, R.; Díaz, W.; Reyes, G.; Balladares, E.; Parra, R. On the Detection of Spectral Emissions of Iron Oxides in Combustion Experiments of Pyrite Concentrates. *Sensors* **2020**, *20*, 1284.

(48) Parameswaran, T.; Gogolek, P.; Hughes, P. Estimation of combustion air requirement and heating value of fuel gas mixtures from flame spectra. *Appl. Therm. Eng.* **2016**, *105*, 353−361.

(49) Ahmadi, Z.; Zabetian Targhi, M. Thermal performance investigation of a premixed surface flame burner used in the domestic heating boilers. *Energy* **2021**, *236*, 121481.

(50) Ding, Y.; Durox, D.; Darabiha, N.; Schuller, T. Chemiluminescence based operating point control of domestic gas boilers with variable natural gas composition,. *Appl. Therm. Eng.* **2019**, *149*, 1052−1060.

(51) Glassman, I. *Combustion*; Elsevier: 1996. DOI: 10.1016/B978-0-12-285852-9.X5000-0.

2.2. Artículo II

Detection of slight variations in combustion conditions with machine learning and computer vision. P. Compais, J. Arroyo, M. A. Castán-Lascorz, J. Barrio, A. Gil. **Engineering Applications of Artificial Intelligence** (2023); Vol. 126, 106772.

Engineering Applications of Artificial Intelligence 126 (2023) 106772

Contents lists available at ScienceDirect

Engineering Applications of Artificial Intelligence

journal homepage: www.elsevier.com/locate/engappai

Detection of slight variations in combustion conditions with machine learning and computer vision

Pedro Compais [a], Jorge Arroyo [a,*], Miguel Ángel Castán-Lascorz [a], Jorge Barrio [a], Antonia Gil [b]

[a] CIRCE Technology Center, Parque Empresarial Dinamiza Avenida Ranillas, 3D 1ª Planta, 50018, Zaragoza, Spain
[b] Universidad de Zaragoza, IUI mixto CIRCE, Campus Rio Ebro, Mariano Esquillor Gómez, 15, 50018, Zaragoza, Spain

ARTICLE INFO

Keywords:
Combustion monitoring
Slight variation
Machine learning
Computer vision
Color image

ABSTRACT

When monitoring combustion conditions, detecting minor variations, which may be complex even for the human eye, is critical for providing a fast response and correcting deviations. The aim of this study is to detect slight variations in combustion conditions by developing a flame monitoring system using machine learning and computer vision techniques applied to color images. Predictive models are developed for fuel blends with different heating values. The predictive models classify the combustion equivalence ratio based on multiple conditions, using a mean step size of 0.10 between states, a lower value than previously reported in related studies. Three machine learning algorithms are used for each fuel blend: logistic regression, support vector machine, and artificial neural network (multilayer perceptron). These models are fed the statistical, geometrical, and textural features extracted from the color images of the flames. The classification achieves accuracies from 0.78 to 0.97 in the detection of slight variations in the combustion conditions for all heating values. Thus, the monitoring system developed in this study is a promising alternative for implementation on an industrial scale and quick detection of changes in combustion conditions.

1. Introduction

Combustion disturbances may shift controlled combustion conditions towards abnormal operation regimes, leading to flashback or extinction of the flame in the worst-case scenario. Measuring minor deviations in combustion conditions from standard combustion operations can enable an early detection of abnormal operation regimes. This early detection is necessary to quickly adjust the process, thereby reducing the operating time under suboptimal conditions and other efficiency problems. Machine learning (ML) techniques can be used to enable advanced combustion monitoring.

Currently, ML techniques are employed in many fields, such as agriculture (Lawal, 2021), surveillance (Matkvoic et al., 2022), biochemical engineering (Mowbray et al., 2021; Roy, 2022), heat pipes (Wang et al., 2021), power systems (Vaish et al., 2021), control systems (Singer and Cohen, 2021), and combustion engines (Aliramezani et al., 2022). ML techniques are employed to analyze data for obtaining insights and achieving higher levels of automation in data analysis. Thus, ML provides powerful tools for analyzing large datasets and addressing problems that are extremely complex or unviable with traditional data analytics. Within the field of combustion, ML has been recently used to optimize the trade-off between emissions and efficiency (Cheng et al., 2018) and to predict multiple characteristics, such as dynamic and steady behavior (Jung et al., 2023), emissions (González-Espinosa et al., 2020; Park et al., 2022), fuel oil viscosity (Ibargüengoytia et al., 2013), and long-term furnace temperature (Quesada et al., 2021). Flame images have been used to predict the operating conditions related to the air–fuel equivalence ratio (ER), such as the air ratio (Bai et al., 2017), O_2 concentration (Yang et al., 2022), and combustion regimes (Abdurakipov et al., 2018; Han et al., 2020, 2021). Combustion conditions were examined in discrete ranges at different values (steps). Mean step widths (step size) of 0.20 (Han et al., 2020) and 0.35 (Abdurakipov et al., 2018) were used to evaluate the influence of the ER on combustion performance. However, the ER can be measured with a higher level of detail by increasing the number of steps (i.e., reducing the step size).

Several ML algorithms have been used to predict combustion conditions, such as logistic regression (LR) (Abdurakipov et al., 2018; Han et al., 2021; Hanuschkin et al., 2021), Gaussian processes (Han et al., 2021), decision trees (Han et al., 2021; Hanuschkin et al., 2021), *k*-nearest neighbor (Bai et al., 2017; Abdurakipov et al., 2018),

Abbreviations: ANN, artificial neural network; ANOVA, analysis of variance; BFG, blast furnace gas; CV, cross-validation; DL, deep learning; ER, equivalence ratio; GLCM, grey level co-occurrence matrix; IF, image feature; LHV, low heating value; LR, logistic regression; ML, machine learning; MLP, multilayer perceptron; PCA, principal component analysis; SVM, support vector machine

* Corresponding author.
E-mail address: jarroyo@fcirce.es (J. Arroyo).

https://doi.org/10.1016/j.engappai.2023.106772
Received 21 December 2022; Received in revised form 23 May 2023; Accepted 4 July 2023
Available online 21 July 2023

linear discriminant analysis (González-Espinosa et al., 2020), support vector machines (SVMs) (Bai et al., 2017; Abdurakipov et al., 2018; Han et al., 2020, 2021), and artificial neural networks (ANNs) (Bai et al., 2017; Abdurakipov et al., 2018; González-Espinosa et al., 2020; Han et al., 2020, 2021; Hanuschkin et al., 2021; Yang et al., 2022). Predictive models are typically fed with relevant features obtained from flame images, which correlate with the combustion variables. Many of these features are extracted from flame images by using computer vision techniques. Features are typically based on statistical (González-Cencerrado et al., 2012, 2013; Sun et al., 2013; González-Cencerrado et al., 2015; Sun et al., 2015; Mathew et al., 2016; Bai et al., 2017; Katzer et al., 2017; González-Espinosa et al., 2020; Compais et al., 2022a,b; Zhu et al., 2023), geometrical (Sun et al., 2013, 2015; Katzer et al., 2017; Hanuschkin et al., 2021; Liu et al., 2021; Compais et al., 2022a), and textural measures (Bai et al., 2017; Compais et al., 2022a; Yang et al., 2022).

Owing to the many available features, most applications choose a limited data subset tailored to the case study. To compress and visualize feature information, some researchers have employed principal component analysis (PCA) (Bai et al., 2017; Abdurakipov et al., 2018; Hanuschkin et al., 2021; Yang et al., 2022). However, PCA does not consider the relevance of features for predicting a target. Thus, other techniques are preferred because PCA is not recommended for addressing overfitting (Hanuschkin et al., 2021; Yang et al., 2022). After the predictive models are developed, their performance is usually evaluated using accuracy, F1-score or R^2 metrics, and training-test split and cross-validation (CV) methods. However, predictive models may suffer from overfitting and provide overly optimistic performance results. Several alternatives, such as feature selection, regularization term, and CV, can be used to address overfitting and obtain more robust measures (Bai et al., 2017; Abdurakipov et al., 2018; Han et al., 2020, 2021; Hanuschkin et al., 2021; Quesada et al., 2021). Features can be manually or automatically selected by using other techniques, such as Pearson's correlation coefficient or analysis of variance (ANOVA). CV can be employed for model evaluation and hyperparameter tuning. However, using a unique CV for both tasks may result in overfitting (Cawley and Talbot, 2010). Two different CVs can address this risk: one for hyperparameter tuning and the other for performance evaluation (Cawley and Talbot, 2010; Hanuschkin et al., 2021). Thus, the CV for hyperparameter tuning (inner CV) is nested under the CV for performance evaluation (outer CV), resulting in a nested CV. Owing to model overfitting, using a non-nested CV instead of a nested CV may provide overly optimistic results for model performance. For example, a 13% accuracy reduction was reported in classification models using nested CV instead of non-nested CV (Abdulaal et al., 2018). Thus, the validation procedures used should be considered when comparing quantitative results from other studies. However, nested and non-nested CVs generally result in the selection of the same model for prediction applications (Wainer and Cawley, 2018).

This study presents an advanced monitoring system based on ML and computer vision to detect minor variations in the combustion conditions. Several ML models are developed and tested on a laboratory-scale burner using different proportions of pure methane (CH_4), a baseline fuel, and blast furnace gas (BFG), a lean fuel. BFG, which is a by-product of the integrated steelmaking sector and decreases the low heating value (LHV) of the gas mixture, thereby leading to different burner behaviors under premixed combustion conditions. Using BFG as fuel in the steel sector is encouraged to improve energy efficiency and reduce fossil fuel consumption and global CO_2 emissions (Cuervo-Piñera et al., 2018). Thus, advanced combustion monitoring systems based on image sensors are helpful tools for this purpose.

This work presents the development of predictive models for ER classification with a significantly high level of detail, using a mean step size of 0.10 between consecutive combustion conditions. This accuracy exceeds the human eye's sensibility and implies accurate control of combustion processes (Bai et al., 2017). The methodology includes three characteristics that had not been implemented together before and whose separate use is scarcely reported in the field of combustion monitoring. First, whereas most combustion studies only include one or two image features (IFs), in this work, statistical, geometrical, and textural IF are extracted to achieve a complete combustion characterization. Second, ANOVA F-tests are performed to automatically select IFs for training predictive models. This approach is implemented to overcome the potential issue of overfitting, which is a significant obstacle to minor ER changes.

Finally, while other studies involved the use of less robust methods, such as a unique CV for model evaluation and hyperparameter turning or no CV at all, we use nested CV for model evaluation and hyperparameter tuning. Here, the hyperparameters for predictive models are automatically defined with the nested CV. The model accuracy is measured for each hyperparameter combination in the inner CV, and the combination with the highest accuracy is selected for the outer CV. The objective of implementing a nested CV is the same as that of the ANOVA F-tests: the reduction of overfitting in detecting slight ER variations. Predictive models are developed using three different ML algorithms: LR, SVM, and ANNs with multilayer perceptron (MLP). The performance of the predictive models is evaluated to study their behavior and compare the differences between the models, ML algorithms, ER classes, and fuel blends.

2. Material and methods

2.1. Experimental setup

Experimental tests were performed in a combustion chamber equipped with a premixed gas fuel burner with a maximum power of 20 kW_{th}. Fig. 1 shows a schematic of the experimental setup. The burner comprised two separate fuel and air inlets with diameters of 25 mm and 10 mm. Air and fuel were premixed in a plenum inside the burner, and the mixture left through a 100-mm-diameter header and a pattern of 5-mm-diameter holes.

The burner was fed from bottles of gaseous fuel through two independent lines. Each line was designed to feed gaseous fuel with different heating values. The fuel mixtures were prepared by using a gas supplier based on the composition and quality requirements. A compressor supplied the combustion air, and an ITV2000 electropneumatic regulator (SMC España S.A., Spain) controlled the pressure (and thus the airflow rate). The airflow rate was measured before burner connection using an SD6000 airflow switch (IFM Electronic GmbH, Germany). The pressure control and airflow rate were digitized using a data acquisition system and computer. Flame color images were acquired by using a DFK 33GX174 color camera (The Imaging Source Europe GmbH, Germany) with a IMX174LQJ sensor (Sony Europe, Netherlands) of 2.3 MP.

Three fuel blends with different LHV values (Table 1) were tested during the experiment. Fuels were selected based on interest in using BFG, a low-calorific power gas, in the steel sector. Blends with a high percentage of BFG led to increased combustion instability owing to the composition of the inert gases. Pure CH_4 was employed as the baseline for combustion with the highest LHV (MIX1). In contrast, the pure BFG exhibited the lowest LHV (MIX3). Finally, a fuel blend composed of 30% vol. CH_4 and 70% vol. BFG was studied as an intermediate LHV scenario (MIX2). The latter is relevant in the steel industry for the valorization of BFG in reheating furnaces (Caillat, 2017; Cuervo-Piñera et al., 2017). For each fuel blend, the combustion conditions were modified by changing the airflow rate and operating with different ERs at a fixed power of 5.5 kW_{th}. Further details regarding the experimental procedure can be found in Compais et al. (2022a).

2.2. Methods

Here, predictive models focused on the innovative detection of minor ER variations, providing greater detail in estimating the ER than

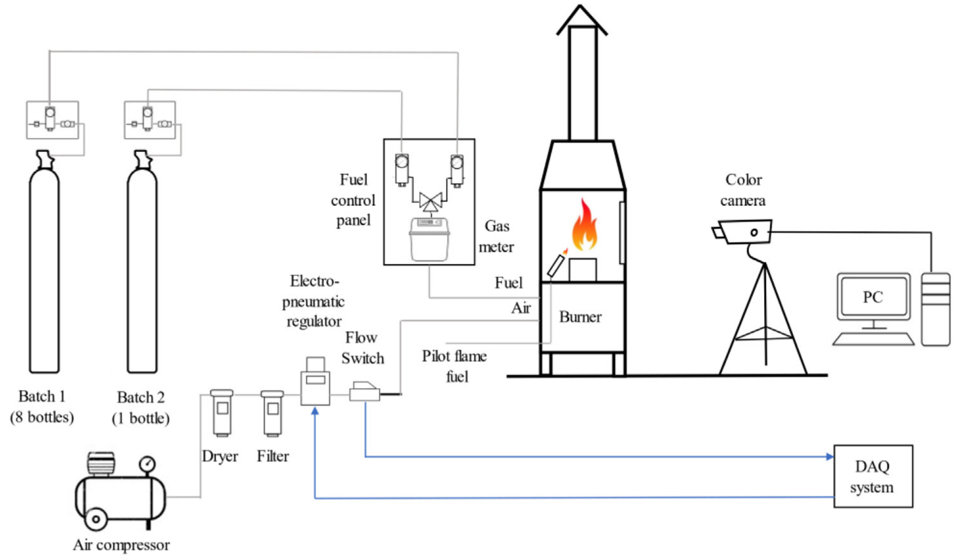

Fig. 1. Scheme of the combustion laboratory. DAQ: data acquisition.

Table 1
Composition of fuel blends (Compais et al., 2022a).

Fuel blend	MIX1	MIX2	MIX3
[CH_4] (%vol.)	100	28	–
[H_2] (%vol.)	–	3	4
[CO] (%vol.)	–	16	22
[CO_2] (%vol.)	–	16	22
[N_2] (%vol.)	–	37	52
LHV (MJ/kg)	50.0	10.8	2.8

Table 2
Summary of the experimental tests.

Test	MIX1	MIX2	MIX3
ER_1	1.41	1.13	0.91
ER_2	1.43	1.27	0.94
ER_3	1.51	1.37	1.09
ER_4	1.64	1.41	1.11
ER_5	1.76	1.57	1.24
ER_6	1.88	1.67	–
ER_7	2.01	1.78	–
ER_8	–	1.91	–

in previous studies. Combustion measurements from the experiment conducted by Compais et al. (2022a) were used as input to develop the predictive models. The ER was computed as the ratio between the actual and stoichiometric air–fuel ratios. The mean ER step sizes were 0.10. The ER range was defined for each fuel blend based on its specific flame stability. For example, an ER of 2.01 was achieved for MIX1 but not for MIX2 or MIX3, owing to the extinction of the flame. Table 2 presents the ERs tested for each fuel blend. ERs range from 1.41 to 2.01 (MIX1), 1.13 to 1.91 (MIX2), and 0.91 to 1.24 (MIX3).

The camera acquired the flame images for 6 min after reaching steady conditions for each test (ER class). The camera achieved a frame rate of 12 fps, capturing 4320 images per test. Figs. 2, 3 and 4 show sample images of the combustion regimes for MIX1, MIX2, and MIX3. The ER variations in the flames were so small that they were not visible to the naked human eye. This effect was attributed to using a mean step size of 0.10 ER. Although slight image variations might seem irrelevant at a lab scale, they might result in high volumes of natural gas that were not burned on an industrial scale. In this respect, fine detection of these slight variations could provide energy savings to the steel industry.

Flame images captured during the tests were processed to extract their features. Although all the main feature types for flame images

Table 3
Statistical IF extracted from flame pixels of each color channel.

Feature magnitude	Equation
Mean (μ)	$\frac{1}{P}\sum_{p=1}^{P} x(p)$
Standard deviation (σ)	$\sqrt{\frac{1}{P}\sum_{p=1}^{P}(x(p)-\mu)^2}$
Skewness (s)	$\frac{\frac{1}{P}\sum_{p=1}^{P}(x(p)-\mu)^3}{\sigma^3}$
Kurtosis (k)	$\frac{\frac{1}{P}\sum_{p=1}^{P}(x(p)-\mu)^4}{\sigma^4}$

(statistical, geometrical, and textural) were not included in most combustion studies, they were integrated for comparison in this study. Four statistical features (mean, standard deviation, skewness, and kurtosis), 13 textural features (selected from Haralick et al., 1973), and five geometrical features (area, centroid horizontal coordinate, centroid vertical coordinate, width, and height) were computed. Processing was applied to each color channel to obtain 22 IF per color channel, for 66 IF per color image. Tables 3, 4, and 5 list the selected IFs with their formulations. The equations of the statistical features were referred to as monochrome images of P pixels, where $x(p)$ was the value of pixel p. In textural features, $p(i,j)$ referred to elements in row i and column j of a normalized GLCM. The GLCM had N rows and N columns, where N was defined as the number of gray values in the monochrome image. Geometrical features were computed for binary images of P pixels (with R rows and C columns), with $b(c,r)$ as the binary value (zero or one) of pixel p located in column c and row r. Moreover, C_s and R_s were the horizontal and vertical coordinates of the pixels with binary values of one, respectively.

Before the IF was extracted, the flame images were preprocessed. First, to remove sensor electrical noise, the dark camera signal was subtracted from the flame images (González-Cencerrado et al., 2012, 2013; Huang et al., 2015). The flame pixels were then segmented using thresholding (Mathew et al., 2016; Katzer et al., 2017). The threshold was automatically selected by applying Otsu's method to maximize the variance between the two-pixel classes (Otsu, 1979). The statistical and textural features were extracted. Using Otsu's thresholding, a reduced number of image pixels that were distant from the main flame body were erroneously classified as flame pixels. Although they barely affected the statistical and textural characteristics, these pixels significantly influenced the calculation method for the geometrical features. Therefore, the morphological transformation of erosion (Sreedhar and

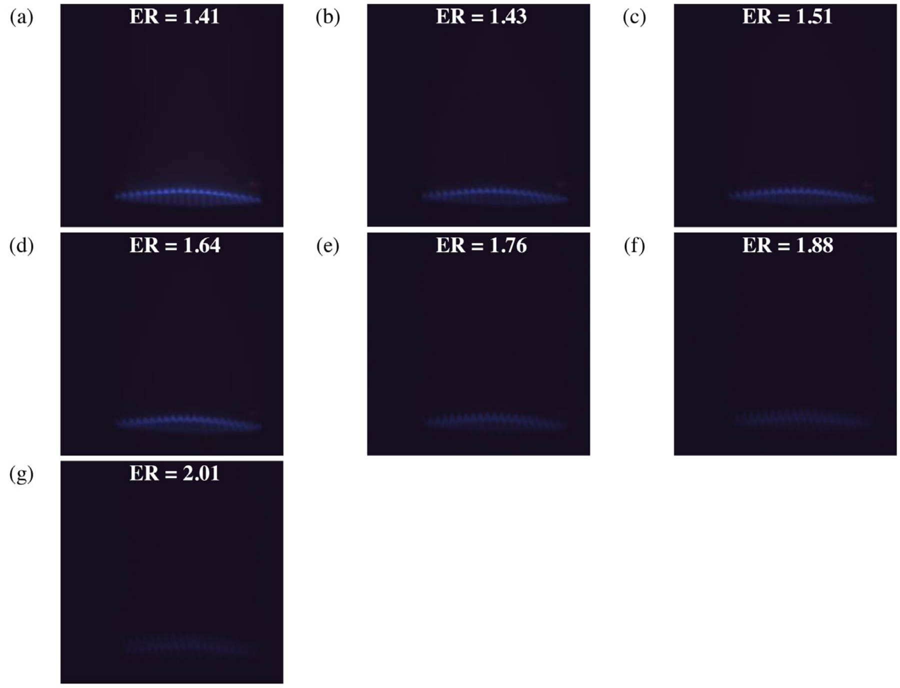

Fig. 2. Sample images of flames for MIX1 and ERs of (a) 1.41, (b) 1.43, (c) 1.51, (d) 1.64, (e) 1.76, (f) 1.88, and (g) 2.01.

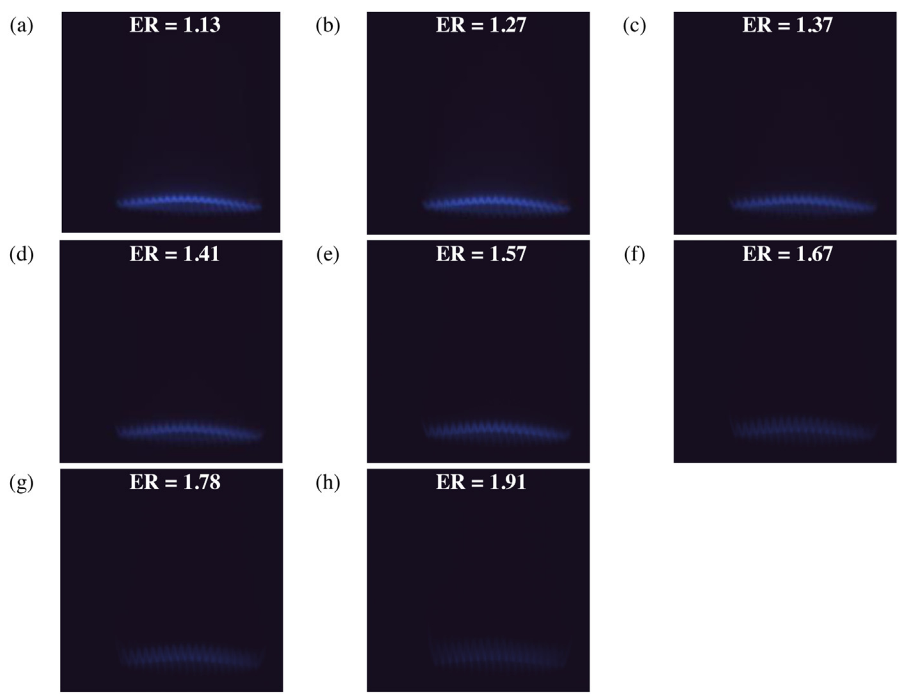

Fig. 3. Sample images of flames for MIX2 and ERs of (a) 1.13, (b) 1.27, (c) 1.37, (d) 1.41, (e) 1.57, (f) 1.67, (g) 1.78, and (h) 1.91.

Panlal, 2012) was used to discard them. Erosion was applied using a 3×3-pixel kernel. Finally, geometrical features were extracted.

Based on the same methodology, different predictive models were developed to detect slight ER variations in three fuel blends (MIX1, MIX2, and MIX3). Each image was labeled with its corresponding fuel blend and ER. Flame color images, fuel blends, and ER labels were used as the datasets. Each fuel blend was tested for a discrete group of ERs and predictive models were developed to classify each ER label. These predictive models estimated the ERs related to the images based on the extracted IF. The behavior of several ML algorithms was analyzed for the ER classification of fuel blends. Predictive models were developed using ML algorithms with different characteristics, namely LR, SVM, and ANN. An MLP with a unique hidden layer of 100 neurons was used for the latter. The ML methodology in this study for each fuel blend is shown in Fig. 5.

The overall ML process for the dataset of a fuel blend is summarized as follows, and specific steps of the method are described in more detail. The dataset of each fuel blend was randomly shuffled and split into training and test sets with 70% and 30% of the samples, respectively. These sets were stratified to include a similar proportion of the ER classes. Each IF's mean and standard deviation in the training set were computed to standardize the dataset. Based on those values,

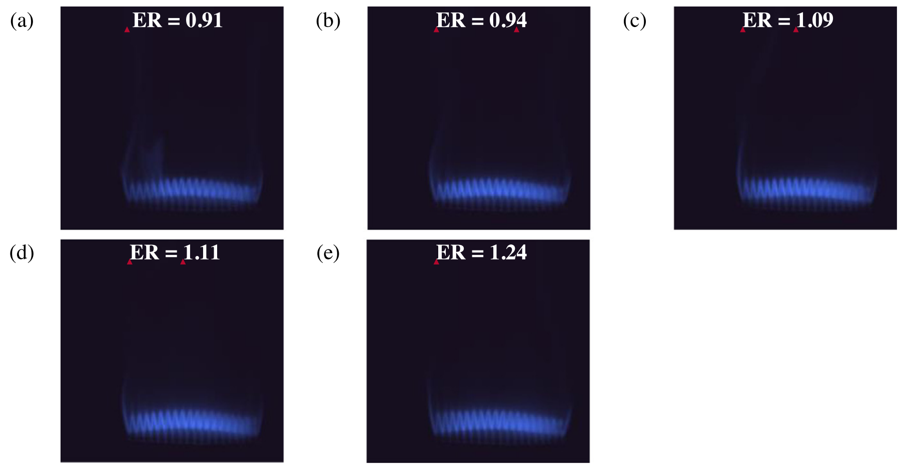

Fig. 4. Sample images of flames for MIX3 and ERs of (a) 0.91, (b) 0.94, (c) 1.09, (d) 1.11, and (e) 1.24.

Table 4
Textural IF extracted from flame pixels of each color channel.

Feature magnitude	Equation
Angular second moment (f_1, energy)	$\sum_{i=1}^{N}\sum_{j=1}^{N} p(i,j)^2$
Contrast (f_2)	$\sum_{i=1}^{N}\sum_{j=1}^{N} (i-j)^2\, p(i,j)$
Correlation (f_3)	$\sum_{i=1}^{N}\sum_{j=1}^{N} \frac{(ij)p(i,j)-\mu_x\mu_y}{\sigma_x\sigma_y}$
Sum of squares (f_4, variance)	$\sum_{i=1}^{N}\sum_{j=1}^{N} \left(i-\mu_x\right)^2 p_{ij}$
Inverse difference moment (f_5)	$\sum_{i=1}^{N}\sum_{j=1}^{N} \frac{p_{ij}}{1+\lvert i-j\rvert}$
Sum average (f_6)	$\sum_{k=2}^{2N} k p_{x+y}(k)$
Sum variance (f_7)	$\sum_{k=2}^{2N} \left(k-\mu_{x+y}\right)^2 p_{x+y}(k)$
Sum entropy (f_8)	$-\sum_{k=2}^{2N} p_{x+y}(k)\log p_{x+y}(k)$
Entropy (f_9)	$-\sum_{i=1}^{N}\sum_{j=1}^{N} p(i,j)\log p(i,j)$
Difference variance (f_{10})	$\sum_{k=0}^{N-1} \left(k-\mu_{x-y}\right)^2 p_{x-y}(k)$
Difference entropy (f_{11})	$-\sum_{k=0}^{N-1} p_{x-y}(k)\log p_{x-y}(k)$
Information measure of correlation I (f_{12}, IMC1)	$\frac{HXY-HXY1}{max(HX,HY)}$
Information measure of correlation II (f_{13}, IMC2)	$\sqrt{1-\exp\left[-2(HXY2-HXY)\right]}$

Table 5
Geometrical IF extracted from flame pixels of each color channel.

Feature magnitude	Equation
Area (a)	$\sum_{r=1}^{R}\sum_{c=1}^{C} b(c,r)$
Centroid horizontal coordinate (c_x)	$\frac{\sum_{r=1}^{R}\sum_{c=1}^{C} cb(c,r)}{a}$
Centroid vertical coordinate (c_y)	$\frac{\sum_{r=1}^{R}\sum_{c=1}^{C} rb(c,r)}{a}$
Width (w)	$\max\left(C_s\right)-\min\left(C_s\right)$
Height (h)	$\max\left(R_s\right)-\min\left(R_s\right)$

training and test sets were standardized. To tackle the overfitting of the predictive models, the training set was analyzed by ANOVA F-tests. The ten IFs with the best variance results were selected and employed as input for predictive models for both training and test sets. Three nested CVs (one per ML algorithm) tuned the hyperparameters and evaluated the performance of each ML algorithm, selecting the best alternative in the end. The chosen ML algorithm was trained with the selected hyperparameters and the training set, and its performance was analyzed, computing its accuracy for the test set. Accuracy was defined as the ratio of the number of correct predictions to the total number of predictions. PCA was not used in the ML method because training time and storage limitations were not critical in this study.

Regarding the ANOVA F-tests, the selected IFs were the ten variables with the highest variance for the ER classes of each fuel blend in the training set. F-tests use a Fisher–Snedecor distribution, and in the case of the ANOVA F-tests, the hypothesis was the dependence of an image feature on the ER class for a specific fuel blend. A confidence level of 0.05 was selected to evaluate this hypothesis, and the F-values, critical F-values, and p-values of the 66 IFs were computed and compared. In the ANOVA F-test of an IF, the hypothesis was supported if its F-value was higher than the critical F-value for the specific fuel blend and the p-value was lower than the confidence level.

Nested CVs were applied with stratification to the training set, with an outer and inner CV of ten and five folds, respectively. The outer CV split the training set into ten training- and validation-subset pairs. Fig. 6 summarizes the ML method for a split i of an outer CV.

For a training subset, an inner CV was applied to define the hyperparameters of the predictive model. Next, the model was trained with the training subset, and its performance was evaluated by calculating its training and validation accuracies, learning curve, and validation confusion matrix. Training and validation accuracies were measured for different subset sizes to compute the learning curves. These sizes were defined as 1%, 25%, 50%, 75%, and 100% of the samples in the outer CV fold. After the ten splits were evaluated, their metrics were averaged, and the mean accuracy was used to select the ML algorithm. The inner CV split each training subset into another five pairs of training and validation subsets. For each pair, every combination of hyperparameters was evaluated. The procedure for the split j and the combination of hyperparameters k is shown in Fig. 7.

For an inner CV split j and a combination of hyperparameters k, the predictive model was trained with the training subset j, and its accuracy was computed for the validation subset j. Values for the five splits were averaged to define the combination of hyperparameters with the highest accuracy. Three values of the regularization term (0.1, 1, and 10) were tested for the three ML algorithms to address the overfitting problem. Moreover, for the SVM, three different kernels were tested (linear, polynomial, and radial basis functions).

The specific code to extract the IF and develop predictive models was developed using Python as the programming language (version 3.7). Several libraries were used for the code: OpenCV, Scikit-learn, NumPy, SciPy, Mahotas, and Pandas.

3. Results and discussion

Several comparative analyses were performed to evaluate the detection of slight ER variations using predictive models. First, the variance of IF with the ER classes was analyzed using the ANOVA F-tests. This assessment compared the subsets of the IF automatically selected for each fuel blend. Apart from the specific IF that formed each subset, the relevance of each subset's color channels, and feature types was checked. Next, the validation accuracy achieved by the predictive models and the effects of the ML algorithm were tested against other related

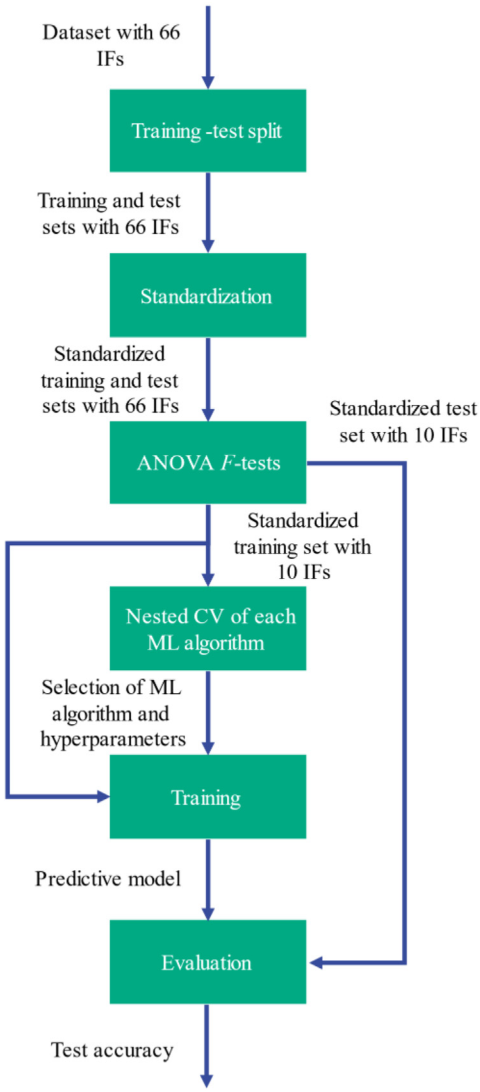

Fig. 5. ML method for each fuel blend.

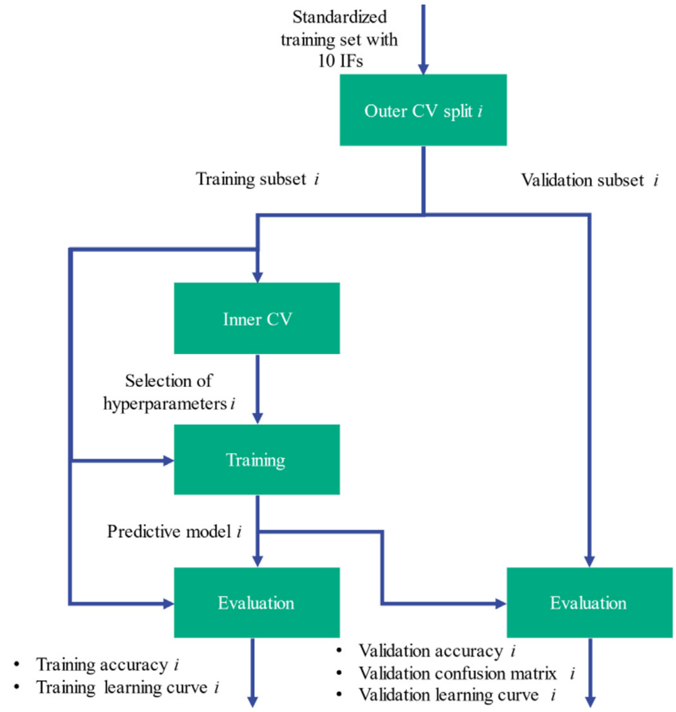

Fig. 6. ML method for the split i of an outer CV.

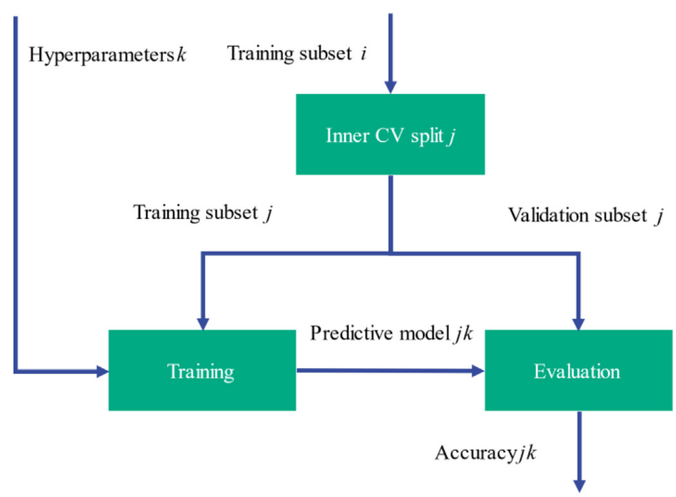

Fig. 7. ML method for the split j of an inner CV and the combination of hyperparameters k.

studies. Also, confusion matrices were computed to evaluate the effect of ER class on the prediction models. Finally, the fit of the predictive models was analyzed using learning curves and by comparing the training, validation, and test accuracies.

3.1. Variance of the IF with the ER classes

The first analysis measured the variance of IF with the ER classes using the ANOVA F-test. The critical F-value was computed for each fuel blend, with a confidence level of 0.05. Fuel blends had critical F-values of 2.10 (MIX1), 2.01 (MIX2), and 2.37 (MIX3). All IF had F-values that were at least two orders of magnitude higher than the critical F-value of the fuel blend. Also, all p-values were lower than the confidence level. Thus, the mean values of each IF were affected by the ER class regardless of the fuel heating value. IF were ordered based on their F-values, and the subset of the 10 IF with the highest F-values was selected to develop the predictive models. The chosen IF are indicated with checkmarks (Tables 6, 7, and 8).

Three subsets of 10 IF were selected, with one subset for each fuel blend. Some visual characteristics were repeated between subsets. In particular, the IF group formed by the three subsets included only 24 different IF from a total computed of 66. The subsets for MIX1 and MIX2 shared four IF: the standard deviation of the green and blue channels, difference entropy of the green channel, and centroid vertical coordinate of the blue channel, which was a feature shared for all fuel blends. The number of IF was computed for each color channel (Fig. 8[a]) and feature types (Fig. 8[b]). The subsets of IF depended on the fuel blend.

For MIX1, only the IF from the green and blue channels were selected. However, in the cases of MIX2 and MIX3, the IFs from the three-color channels were included. Moreover, three feature types were included in selecting IF for MIX1 and MIX2. Nevertheless, only the textural and geometrical features were chosen for MIX3.

3.2. Prediction of slight variations in the ER

After analyzing the variance of the IF with the ER, for each fuel blend, a subset of ten features was selected, which were used for the

Table 6
IF selected from the red color channel for each fuel blend.

Feature type	Feature magnitude	MIX1	MIX2	MIX3
Statistical	Standard deviation (σ)		✓	
Textural	Contrast (f_2)		✓	
Geometrical	Area (a)			✓
Geometrical	Centroid vertical coordinate (c_y)			✓

Table 7
IF selected from the green color channel for each fuel blend.

Feature type	Feature magnitude	MIX1	MIX2	MIX3
Statistical	Standard deviation (σ)	✓	✓	
Textural	Contrast (f_2)		✓	
Textural	Correlation (f_3)			✓
Textural	Sum of squares (f_4, variance)		✓	
Textural	Inverse difference moment (f_5)	✓		
Textural	Difference entropy (f_{11})	✓	✓	
Textural	Information Measure of Correlation II (f_{13}, IMC2)			✓
Geometrical	Area (a)			✓
Geometrical	Centroid vertical coordinate (c_y)	✓		✓

Table 8
IF selected from the blue color channel for each fuel blend.

Feature type	Feature magnitude	MIX1	MIX2	MIX3
Statistical	Standard deviation (σ)	✓	✓	
Statistical	Skewness (s)	✓		
Textural	Contrast (f_2)		✓	
Textural	Correlation (f_3)			✓
Textural	Sum of squares (f_4, variance)		✓	
Textural	Inverse difference moment (f_5)	✓		
Textural	Difference entropy (f_{11})	✓		
Textural	Information Measure of Correlation I (f_{12}, IMC1)	✓		
Textural	Information Measure of Correlation II (f_{13}, IMC2)			✓
Geometrical	Area (a)			✓
Geometrical	Centroid vertical coordinate (c_y)	✓	✓	✓

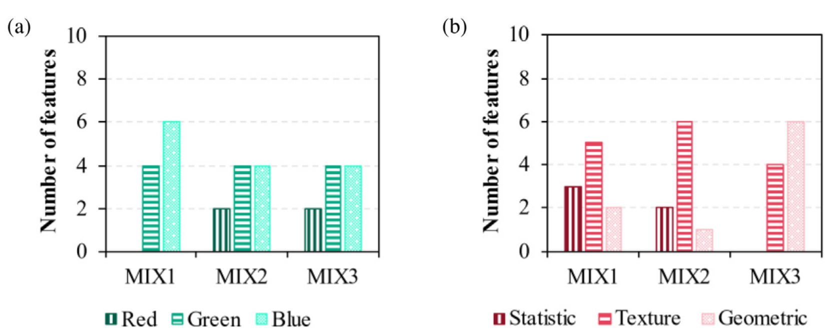

Fig. 8. Number of IF selected for fuel blend, based on (a) their color channel and (b) their feature type.

input and development of predictive models. Three predictive models were developed for each fuel blend using different ML algorithms (LR, SVM, and MLP), and were trained and validated using nested CV. The hyperparameters of the ML algorithms were tuned in this nested CV. The validation accuracies of the predictive models were averaged over the nested CV, and Fig. 9 shows the results.

The predictive models showed similar results for MIX1 and MIX2 expression. ER was estimated using classes with a mean step size of 0.10 (MIX1) and 0.11 (MIX2), achieving validation accuracies between 0.95 and 0.97. In contrast, the ER steps for MIX3 had a lower mean step size (0.08), and validation accuracies of approximately 0.78 were achieved. In summary, the validation accuracies ranged between 0.78 and 0.97, which are typical values for classification models related to ER conditions. For example, Bai et al. (2017) measured accuracies between 0.75 and 0.93 to predict air ratios. However, Han et al. (2021) achieved accuracies of between 0.96 and 1.00 and 0.65 and 0.99 (Han et al., 2020) for the classification of combustion states. Also, Abdurakipov et al. (2018) reported accuracies of 0.89 and 0.98.

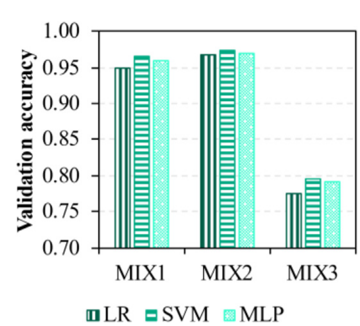

Fig. 9. Validation accuracy of the predictive models developed with different algorithms.

The results were compared in more detail with those of works on similar classification tasks based on combustion conditions with different ER. Han et al. (2020) and Abdurakipov et al. (2018) used mean step sizes of 0.20 and 0.35, respectively, whereas the present work predicted ER conditions using a mean step size of 0.10, which is at least two times lower. The use of larger mean step sizes facilitates the image classification task because image flames present significant differences that could be perceived by the human eye, as shown when analyzing figures in their works. However, the classification task in this work is more difficult because of the smaller mean step size, which provided image differences hardly perceived by the human eye. To address this challenge, we proposed a novel methodology for previous combustion studies. In summary, using smaller ER steps and a nested CV, the current study predicted ER conditions with a considerably high level of detail, with accuracies like previous studies.

3.3. Effect of the ML algorithm

Results (Fig. 9) show that using a different ML algorithm barely affected the validation accuracy of the predictive models regardless of the fuel blend. LR, SVM, and MLP models achieved validation accuracies with a maximum deviation of 3%. SVM provided the highest accuracies for the three fuel blends (0.967, 0.973, and 0.795). Previous studies measured variations in accuracy below 2% between SVM and ANN (Bai et al., 2017) and LR and SVM (Abdurakipov et al., 2018). In the work of Han et al. (2020), the highest accuracy was achieved by SVM compared with ANN. Nevertheless, high deviations (< 19%) between LR, SVM, and ANN have been reported in some cases (Bai et al., 2017; Abdurakipov et al., 2018; Han et al., 2020). Moreover, ANN achieved better results than SVM in the studies by Bai et al. (2017) and Abdurakipov et al. (2018). Therefore, the behavior of the ML algorithms may be dependent on the case conditions, and the current research achieved similar results to those of previous studies.

3.4. Effect of the ER class

As Fig. 9 shows, the validation accuracy decreased significantly for MIX3. To analyze this behavior in detail, the confusion matrixes of the predictive models were analyzed. Results are shown (Fig. 10) for the SVM model, which provided the highest validation accuracy.

For MIX1 and MIX2, confusion matrixes showed similar results. Regardless of the ER class, the predictive models correctly estimated the ER value for most samples (95% at minimum). Incorrect classifications occurred only for a few samples with consecutive ER classes, such as 1.43 and 1.51 in the case of MIX1 (Fig. 10[a]). However, the behavior of the predictive model was different for MIX3, where the ER estimation exhibited lower accuracies when distinguishing between class pairs of 0.91–0.94 and 1.09–1.11 (Fig. 10[c]). These conditions had the smallest ER variations (0.03 and 0.02), together with 1.41–1.43 for MIX1. However, the latter case was more accurate despite its low ER variation. Due to the lower combustion stability caused by its lower heating value, the classification could be more complex for MIX3 than for MIX1. Also, it is observed that when the ER increased between 0.91 and 1.24, the validation accuracy for MIX3 was higher. These variations could be related to combustion stability changes, as reported by Zheng et al. (2021).

3.5. Fit of the predictive models

To evaluate the predictive models in more detail, learning curves were computed. Fig. 11 shows the learning curves for the predictive models developed using the SVM, which provided the highest accuracies.

For each fuel blend, the validation accuracy increased with increasing subset size, approaching the same value as the training accuracy. This behavior is considered a good fit for the predictive models, which did not suffer from underfitting or overfitting. Furthermore, as the predictive models were stable at a subset size of 25%, similar results

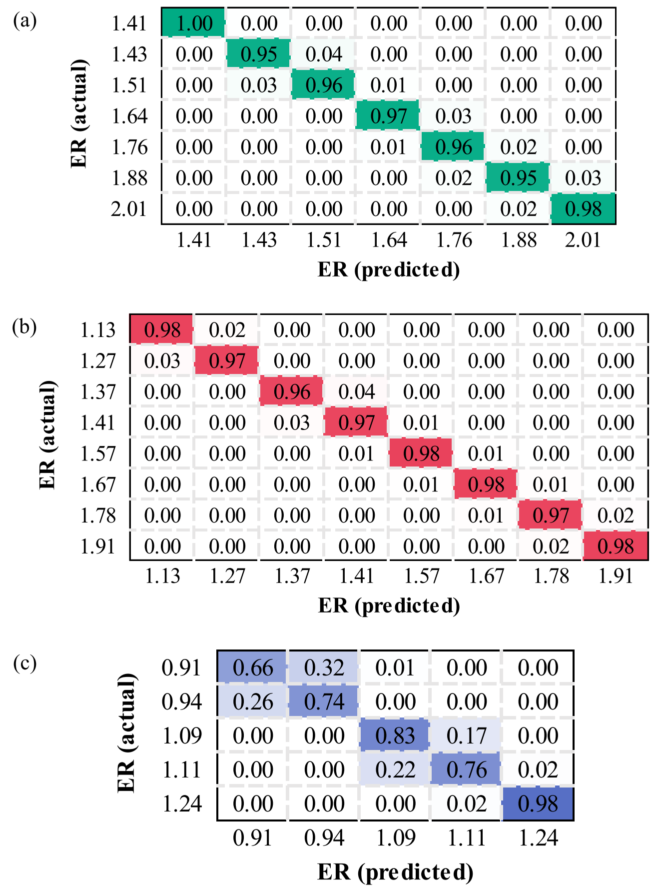

Fig. 10. Confusion matrixes of the predictive models developed with the SVM algorithm for (a) MIX1, (b) MIX2, and (c) MIX3.

could be achieved by acquiring only 1080 images per class, reducing the test duration from 360 s (Compais et al., 2022a) to 90 s, or the frame rate from 12 (Compais et al., 2022a) to 3 fps.

To provide a final test for the ER classification, predictive models with the best results were trained with the entire training set and evaluated with the test set, which had not been used to develop the predictive models. Only the SVM models were evaluated in this step, as they achieved the highest accuracy. The hyperparameters of the SVM models were defined based on the best results obtained in the hyperparameter tuning: a regularization term of 10 for the three fuel blends, radial basis function kernel for MIX1 and MIX3, and linear kernel for MIX 2. Their accuracies were computed to evaluate the SVM models using the test set. Fig. 12 shows the accuracies for the SVM model, including the previous training and validation accuracies and the new test accuracies.

The accuracies achieved using the test set were like those of the training and validation sets. Therefore, the SVM models exhibited acceptable behavior for previously unseen flame images.

4. Conclusions

This paper presented a novel methodology for detecting slight variations in combustion conditions. The fuel blends used here are pure CH_4, 30% vol. CH_4/70% vol. BFG, and pure BFG. The combustion was analyzed using a laboratory-premixed burner at a fixed thermal power of 5.5 kW. The developed methodology was based on extracting statistical, geometrical, and textural features from flame images, their automatic selection with ANOVA F-tests, the automatic selection of hyperparameters, and the robust performance evaluation for predictive

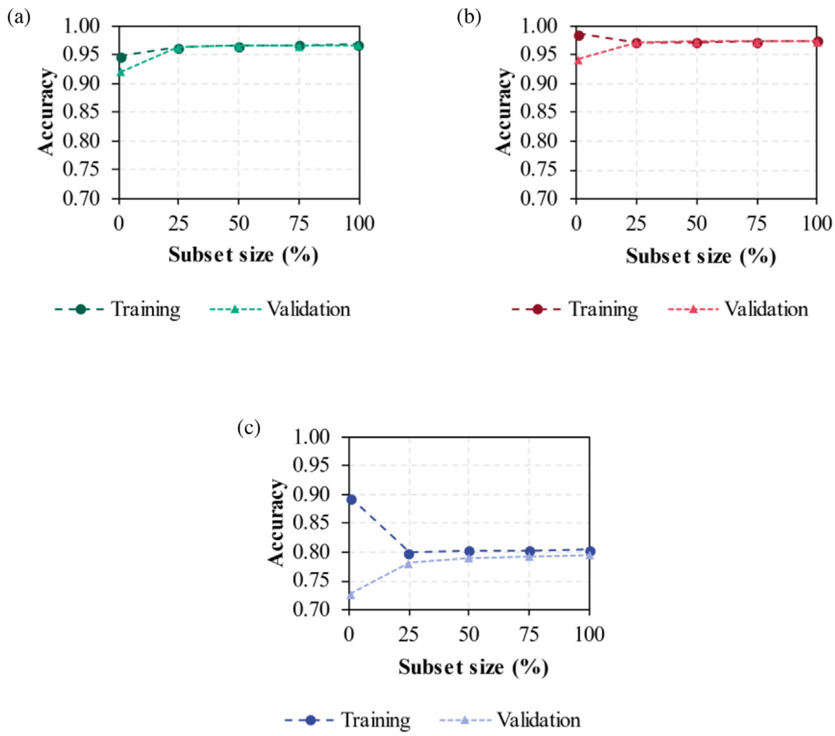

Fig. 11. Learning curves of the SVM model for (a) MIX1, (b) MIX2, and (c) MIX3.

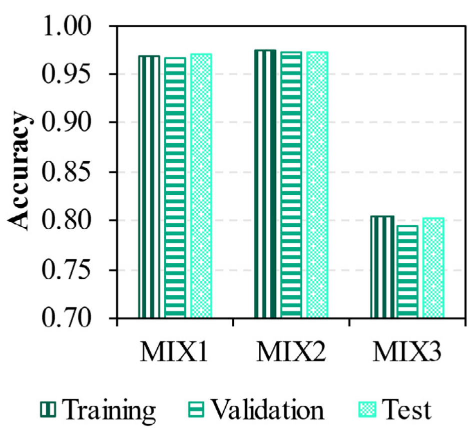

Fig. 12. Training, validation, and test accuracies of the SVM model for MIX1, MIX2, and MIX3.

models using nested CV. This methodology aimed to reduce overfitting, which was critical for the current application. Predictive models were developed for the ER classification of each fuel blend using three ML algorithms (LR, SVM, and ANN [MLP]). The performance of the predictive models was evaluated using a training–test split and nested CV within the training set by computing their accuracy, confusion matrices, and learning curves.

The model developed in this work allowed the prediction of the ER using a mean step size of 0.10, which in the case of the selected fuel mixtures, implied differences that would be difficult to be perceived by the human eye. The detection of slight changes in the combustion conditions allowed for the correction of deviated parameters, helping to optimize the processes and avoid the appearance of critical instabilities.

It was confirmed that the computed IFs used were affected by the ER class regardless of the fuel heating value. However, the subset of IFs with the highest variances depended on the fuel heating value. The subsets for the first and second mixtures shared three IFs: the standard deviation of the green and blue channels and the difference entropy of the green channel. The subsets of the three fuel blends shared only one IF, the centroid vertical coordinate of the blue channel. Moreover, the subsets of IF for all heating values included textural and geometrical features from the green and blue channels.

For the different fuel heating values, using different ML algorithms (LR, SVM, and ANN [MLP]) had no significant effect on accuracy. Nevertheless, the SVM models always provided the best results. Predictive models showed a relevant decrease in accuracy for the conditions with the lower fuel heating value (MIX3), reducing its value from 0.95–0.97 to 0.78. Considering SVM models, significant misclassifications for MIX3 occurred for consecutive ER classes with the smallest step sizes (0.02–0.03). However, for the conditions with a higher fuel heating value (MIX1), the predictive models obtained a higher accuracy when predicting consecutive ER classes with a step size of 0.03.

The SVM models showed a satisfactory fit to the data without underfitting or overfitting. The models achieved stability with only 25% of the flame images. Therefore, the test duration or frame rate could be reduced. Finally, the accuracy of the SVM models was measured again using a test set with previously unused flame images. The SVM models showed similar values to previous accuracies; thus, they performed well with unseen flame images.

The decreased accuracy reported for the fuel blend with the lower heating value could be used to propose future studies focused on monitoring fuel blends with low heating values to increase prediction accuracy. The current research sets the stage for automated monitoring of minor variations in the combustion of gaseous fuels.

Finally, the current research results, carried out at a laboratory level, would enable the development of these systems for their final implementation in industrial furnaces of the steel sector, where the mixtures used in this work present an alternative for fossil fuel substitution and, thus, for their decarbonization.

Funding

This work was supported by the European Union's Horizon 2020 Research and Innovation Programme under grant agreement No. 820771 (BAMBOO project) and 869939 (RETROFEED project).

CRediT authorship contribution statement

Pedro Compais: Conceptualisation, Methodology, Software, Formal Analysis, Investigation, Data curation, Writing – original draft, Writing – review & editing, Visualisation. **Jorge Arroyo:** Conceptualisation, Methodology, Validation, Investigation, Resources, Writing – review & editing, Supervision, Project Administration. **Miguel Ángel Castán-Lascorz:** Software, Data curation, Writing – review & editing. **Jorge Barrio:** Software, Data curation, Writing – review & editing. **Antonia Gil:** Writing – review & editing, Supervision.

Declaration of competing interest

The authors declare the following financial interests/personal relationships which may be considered as potential competing interests: Jorge Arroyo reports financial support was provided by European Commission.

Data availability

The data that has been used is confidential.

References

Abdulaal, M.J., Casson, A.J., Gaydecki, P., 2018. Performance of nested vs. non-nested SVM cross-validation methods in visual BCI: Validation study. In: European Signal Processing Conference. Vol. 2018, pp. 1680–1684. http://dx.doi.org/10.23919/EUSIPCO.2018.8553102.

Abdurakipov, S.S., Gobyzov, O.A., Tokarev, M.P., Dulin, V.M., 2018. Combustion regime monitoring by flame imaging and machine learning. Optoelectron. Instrument. Data Process 54, 513–519. http://dx.doi.org/10.3103/S875669901805014X.

Aliramezani, M., Koch, C.R., Shahbakhti, M., 2022. Modeling, diagnostics, optimization, and control of internal combustion engines via modern machine learning techniques: A review and future directions. Prog. Energy Combust. Sci. 88, 100967. http://dx.doi.org/10.1016/j.pecs.2021.100967.

Bai, X., Lu, G., Hossain, M.M., Szuhánski, J., Daood, S.S., Nimmo, W., Yan, Y., Pourkashanian, M., 2017. Multi-mode combustion process monitoring on a pulverised fuel combustion test facility based on flame imaging and random weight network techniques. Fuel 202, 656–664. http://dx.doi.org/10.1016/j.fuel.2017.03.091.

Caillat, S., 2017. Burners in the steel industry: Utilization of by-product combustion gases in reheating furnaces and annealing lines. Energy Procedia 120, 20–27. http://dx.doi.org/10.1016/j.egypro.2017.07.152.

Cawley, G.C., Talbot, N.L.C., 2010. On over-fitting in model selection and subsequent selection bias in performance evaluation. J. Mach. Learn. Res. 11, 2079–2107.

Cheng, Y., Huang, Y., Pang, B., Zhang, W., 2018. ThermalNet: A deep reinforcement learning-based combustion optimization system for coal-fired boiler. Eng. Appl. Artif. Intell. 74, 303–311. http://dx.doi.org/10.1016/j.engappai.2018.07.003.

Compais, P., Arroyo, J., González-Espinosa, A., Castán-Lascorz, M.Á., Gil, A., 2022a. Optical analysis of blast furnace gas combustion in a laboratory premixed burner. ACS Omega 7, 24498–24510. http://dx.doi.org/10.1021/acsomega.2c02103.

Compais, P., Arroyo, J., González-Espinosa, A., Gonzalo-Tirado, C., Castán-Lascorz, M.A., Barrio, J., Cuervo-Piñera, V., 2022b. Experimental analysis of blast furnace gas co-firing in a semi-industrial furnace using colour images. In: Proceedings of the 7th World Congress on Momentum, Heat and Mass Transfer, Apr. 2022, Paper No. CSP 117. http://dx.doi.org/10.11159/csp22.117.

Cuervo-Piñera, V., Cifrián-Riesgo, D., Battaglia, V., Fantuzzi, M., Della-Rocca, A., Ageno, M., Rensgard, A., Wang, C., Niska, J., Ekman, T., Rein, C., Nguyen, P.D., 2018. High Efficiency Low NOX BFG Based Combustion Systems in Steel Reheating Furnaces (HELNOx-BFG). final report, Publications Office, European Commission, Directorate-General for Research and Innovation.

Cuervo-Piñera, V., Cifrián-Riesgo, D., Nguyen, P.D., Battaglia, V., Fantuzzi, M., Della Rocca, A., Ageno, M., Rensgard, A., Wang, C., Niska, J., Ekman, T., Rein, C., Adler, W., 2017. Blast furnace gas based combustion systems in steel reheating furnaces. Energy Procedia 120, 357–364. http://dx.doi.org/10.1016/j.egypro.2017.07.215.

González-Cencerrado, A., Gil, A., Peña, B., 2013. Characterization of PF flames under different swirl conditions based on visualization systems. Fuel 113, 798–809. http://dx.doi.org/10.1016/j.fuel.2013.05.077.

González-Cencerrado, A., Peña, B., Gil, A., 2012. Coal flame characterization by means of digital image processing in a semi-industrial scale PF swirl burner. Appl. Energy 94, 375–384. http://dx.doi.org/10.1016/j.apenergy.2012.01.059.

González-Cencerrado, A., Peña, B., Gil, A., 2015. Experimental analysis of biomass co-firing flames in a pulverized fuel swirl burner using a CCD based visualization system. Fuel Process. Technol. 130, 299–310. http://dx.doi.org/10.1016/j.fuproc.2014.10.041.

González-Espinosa, A., Gil, A., Royo-Pascual, L., Nueno, A., Herce, C., 2020. Effects of hydrogen and primary air in a commercial partially-premixed atmospheric gas burner by means of optical and supervised machine learning techniques. Int. J. Hydrogen Energy 45, 31130–31150. http://dx.doi.org/10.1016/j.ijhydene.2020.08.045.

Han, Z., Hossain, M.M., Wang, Y., Li, J., Xu, C., 2020. Combustion stability monitoring through flame imaging and stacked sparse autoencoder based deep neural network. Appl. Energy 259, 114159. http://dx.doi.org/10.1016/j.apenergy.2019.114159.

Han, Z., Li, J., Zhang, B., Hossain, M.M., Xu, C., 2021. Prediction of combustion state through a semi-supervised learning model and flame imaging. Fuel 289, 119745. http://dx.doi.org/10.1016/j.fuel.2020.119745.

Hanuschkin, A., Zündorf, S., Schmidt, M., Welch, C., Schorr, J., Peters, S., Dreizler, A., Böhm, B., 2021. Investigation of cycle-to-cycle variations in a spark-ignition engine based on a machine learning analysis of the early flame kernel. Proc. Combust. Inst. 38, 5751–5759. http://dx.doi.org/10.1016/j.proci.2020.05.030.

Haralick, R.M., Shanmugam, K., Dinstein, I., 1973. Textural features for image classification. IEEE Trans. Syst. Man Cybern. SMC-3, 610–621. http://dx.doi.org/10.1109/TSMC.1973.4309314.

Huang, M., Xiao, Y., Zhang, Z., Shao, W., Xiong, Y., Liu, Y., Liu, Z., Lei, F., 2015. Effect of air/fuel nozzle arrangement on the MILD combustion of syngas. Appl. Therm. Eng. 87, 200–208. http://dx.doi.org/10.1016/j.applthermaleng.2015.04.076.

Ibargüengoytia, P.H., Delgadillo, M.A., García, U.A., Reyes, A., 2013. Viscosity virtual sensor to control combustion in fossil fuel power plants. Eng. Appl. Artif. Intell. 26, 2153–2163. http://dx.doi.org/10.1016/j.engappai.2013.05.004.

Jung, M.Y., Chang, J.H., Oh, M., Lee, C., 2023. Dynamic model and deep neural network-based surrogate model to predict dynamic behaviors and steady-state performance of solid propellant combustion. Combust. Flame 250, 112649. http://dx.doi.org/10.1016/j.combustflame.2023.112649.

Katzer, C., Babul, K., Klatt, M., Krautz, H.J., 2017. Quantitative and qualitative relationship between swirl burner operating conditions and pulverized coal flame length. Fuel Process. Technol. 156, 138–155. http://dx.doi.org/10.1016/j.fuproc.2016.10.013.

Lawal, M.O., 2021. Tomato detection based on modified YOLOv3 framework. Sci. Rep. 11, 1447. http://dx.doi.org/10.1038/s41598-021-81216-5.

Liu, Y., Xue, Q., Zuo, H., Yang, F., Peng, X., Wang, J., 2021. Effects of CO_2 and N_2 dilution on the combustion characteristics of H_2/CO mixture in a turbulent, partially premixed burner. ACS Omega 6, 15651–15662. http://dx.doi.org/10.1021/acsomega.1c00534.

Mathew, A.P., Asokan, A., Batri, K., Sivakumar, D., 2016. Comparative analysis of flame image features for combustion analysis. Indian J. Sci. Technol. 9, 1–11. http://dx.doi.org/10.17485/ijst/2016/v9i6/79904.

Matkvoic, F., Ivasic-Kos, M., Ribaric, S., 2022. A new approach to dominant motion pattern recognition at the macroscopic crowd level. Eng. Appl. Artif. Intell. 116, 105387. http://dx.doi.org/10.1016/j.engappai.2022.105387.

Mowbray, M., Savage, T., Wu, C., Song, Z., Cho, B.A., Del Rio-Chanona, E.A., Zhang, D., 2021. Machine learning for biochemical engineering: A review. Biochem. Eng. J. 172, 108054. http://dx.doi.org/10.1016/j.bej.2021.108054.

Otsu, N., 1979. A threshold selection method from gray-level histograms. IEEE Trans. Syst. Man Cybern. SMC-9, 62–66. http://dx.doi.org/10.1109/TSMC.1979.4310076.

Park, M., Hur, J., Lee, W., 2022. Prediction of oil-fired boiler emissions with ensemble methods considering variable combustion air conditions. J. Clean. Prod. 375, 134094. http://dx.doi.org/10.1016/j.jclepro.2022.134094.

Quesada, D., Valverde, G., Larrañaga, P., Bielza, C., 2021. Long-term forecasting of multivariate time series in industrial furnaces with dynamic Gaussian Bayesian networks. Eng. Appl. Artif. Intell. 103, 104301. http://dx.doi.org/10.1016/j.engappai.2021.104301.

Roy, A.M., 2022. Adaptive transfer learning-based multiscale feature fused deep convolutional neural network for EEG MI multiclassification in brain–computer interface. Eng. Appl. Artif. Intell. 116, 105347. http://dx.doi.org/10.1016/j.engappai.2022.105347.

Singer, G., Cohen, Y., 2021. A framework for smart control using machine-learning modeling for processes with closed-loop control in Industry 4.0. Eng. Appl. Artif. Intell. 102, 104236. http://dx.doi.org/10.1016/j.engappai.2021.104236.

Sreedhar, K., Panlal, B., 2012. Enhancement of images using morphological transformations. Int. J. Comp. Sci. Inf. Technol. 4, 33–50. http://dx.doi.org/10.5121/ijcsit.2012.4103.

Sun, D., Lu, G., Zhou, H., Li, X., Yan, Y., 2013. A simple index based quantitative assessment of flame stability. In: 2013 IEEE International Conference on Imaging Systems and Techniques. IST, Vol. 2013, pp. 190–193. http://dx.doi.org/10.1109/IST.2013.6729689.

Sun, D., Lu, G., Zhou, H., Yan, Y., Liu, S., 2015. Quantitative assessment of flame stability through image processing and spectral analysis. IEEE Trans. Instrum. Meas. 64, 3323–3333. http://dx.doi.org/10.1109/TIM.2015.2444262.

Vaish, R., Dwivedi, U.D., Tewari, S., Tripathi, S.M., 2021. Machine learning applications in power system fault diagnosis: Research advancements and perspectives. Eng. Appl. Artif. Intell. 106, 104504. http://dx.doi.org/10.1016/j.engappai.2021.104504.

Wainer, J., Cawley, G., 2018. Nested cross-validation when selecting classifiers is overzealous for most practical applications. http://dx.doi.org/10.48550/arXiv.1809.09446, arXiv:1809.09446.

Wang, Z., Zhao, X., Han, Z., Luo, L., Xiang, J., Zheng, S., Liu, G., Yu, M., Cui, Y., Shittu, S., Hu, M., 2021. Advanced big-data/machine-learning techniques for optimization and performance enhancement of the heat pipe technology – a review and prospective study. Appl. Energy 294, 116969. http://dx.doi.org/10.1016/j.apenergy.2021.116969.

Yang, G., He, Y., Li, X., Liu, H., Lan, T., 2022. Gabor-GLCM-based texture feature extraction using flame image to predict the O_2 content and NO_x. ACS Omega 7, 3889–3899. http://dx.doi.org/10.1021/acsomega.1c03397.

Zheng, W., Pang, L., Liu, Y., Xie, F., Zeng, W., 2021. Effects of methane addition on laminar flame characteristics of premixed blast furnace gas/air mixtures. Fuel 302, 121100. http://dx.doi.org/10.1016/j.fuel.2021.121100.

Zhu, J., Wang, Z., Li, R., Liu, S., Hua, Y., 2023. Experimental study and prediction model of combustion stability and combustion mode variation of burning methanol/biodiesel blends for diesel engines. Fuel 335, 127038. http://dx.doi.org/10.1016/j.fuel.2022.127038.

2.3. Artículo III

Flame monitoring system based on images for steel reheating furnaces: a case study of validation from laboratory to semi-industrial scales. P. Compais, J. Arroyo, V. Cuervo-Piñera, A. Gil. *Proceedings of the 18th Conference on Sustainable Development of Energy, Water and Environment Systems* (2023), Dubrovnik (Croatia).

Flame Monitoring System Based on Images for Steel Reheating Furnaces: a Case Study of Validation from Laboratory to Semi-Industrial Scales

P. Compais*, J. Arroyo
CIRCE Technology Centre, Parque Empresarial Dinamiza Avenida Ranillas, 3D 1ª Planta, 50018, Zaragoza, Spain
e–mail: plcompais@fcirce.es, jarroyo@fcirce.es

V. Cuervo-Piñera
ArcelorMittal, PO Box 90, Avilés, 33480, Spain
e-mail: victor.cuervo@arcelormittal.com

A. Gil
Department of Mechanical Engineering
Universidad de Zaragoza. IUI mixto CIRCE. Campus Rio Ebro. Mariano Esquillor Gómez, 15, 50018 Zaragoza, Spain
e-mail: antgilma@unizar.es

ABSTRACT

The steel industry is searching for novel image systems to monitor multiple burners individually. Such a development is highly complex and requires studies on several scales. This work analyses the robustness of an imaging system in different scenarios, from the laboratory (design and development) and semi-industrial (implementation) stages, using 20 kW and 1.2 MW burners, respectively. The monitoring system predicts oxygen concentration in flue gases on both scales, achieving accuracies higher than 0.95 in most cases and 0.79 as a minimum. The vision system detects slight variations in combustion conditions and addresses differences among development phases, including burner typologies and system placements. This study leads flame monitoring systems based on images toward their final development on an industrial scale.

KEYWORDS

Flame monitoring, system validation, computer vision, machine learning, steel reheating furnace, blast furnace gas

INTRODUCTION

Energy-intensive industries continue searching for alternatives to increase their efficiency and sustainability. The steel industry demands high-temperature processes, mainly by the combustion of solid, liquid, or gaseous fuels. Monitoring systems can enhance the control and performance of such combustion processes, reducing fuel consumption, emissions, and costs, to reach European targets for carbon emissions by 2030.

Industrial furnaces are usually equipped with several groups of burners, and the furnace operation is evaluated by analysing global combustion parameters. Monitoring air-fuel flows and flue gas emissions for each burner could detect individual malfunctions to raise the efficiency of the process. Still, this alternative is not feasible by the high cost of individual monitoring with traditional sensors. Thus, novel systems are searched to monitor multiple burners individually. In this context, image systems equipped with computer vision and

Machine Learning (ML) systems have a high potential, enabling the supervision of several burners by a single camera.

Cameras can be employed to evaluate the combustion [1] and compute quantitative characteristics such as the flame area [2]. These systems can be developed to predict the equivalence ratio [3] or different combustion conditions [4]. Computer vision algorithms usually use flame segmentation to compute image features from only flame pixels. However, flame segmentation could be complex or inaccurate for images without a clear flame body. Another alternative is the analysis of flame images without performing flame segmentation, extracting features for the whole image [5, 6]. Typical image features can be split into statistical, textural, and geometrical. Statistical and textural features can be extracted from images with and without flame segmentation. Nevertheless, geometrical features need flame segmentation to define the flame body and compute characteristics such as the flame length.

Developing advanced image systems for industrial scale is challenging and needs studies at several scales. However, most research works in the open literature focus on a single scale, usually the laboratory scale. This work presents the validation or joint assessment for laboratory and semi-industrial scales of an advanced image system that automatically predicts oxygen (O_2) concentration in flue gases using an image sensor. The two-scale validation is a novelty concerning previous works focused on a single scale, enhancing the insight into sensitivity to changes and robustness of image systems for combustion monitoring. In this aspect, the system's image sensor, image processing, and predictive model were evaluated in different scenarios by comparing design, simulation, and implementation results. A combustion chamber with a 20-kW burner was used for the laboratory scale, while a 1.2 MW burner was employed for the semi-industrial scale furnace. The rated power of the large burner is higher than those used in previous industrial works [7]. Nevertheless, our case was defined as a semi-industrial scale because the furnace has only one burner, whereas, at the industrial scale, the furnace is equipped with multiple burners.

This work is focused on a specific case of the iron and steel industry. This industry is searching for novel systems [8] to individually monitor the multiple burners inside reheating furnaces [9]. Natural Gas (NG) and Blast Furnace Gas (BFG) are usually mixed to provide different fuel blends for these furnaces. The steel industry produces BFG as waste gas that can be valorised as fuel within the same facility [10-12]. Nevertheless, BFG has a low heating value and is prone to combustion instabilities [12, 13]. The temperature in the steel-making processes can be raised by increasing the NG share in the fuel blend with BFG. This strategy is used to meet temperature requirements when needed. In this work, the image system validation was focused on the fuel blends 100 %vol. NG, 30 %vol. NG and 70 %vol. BFG, 20 %vol. NG and 80 %vol. BFG and 100 %vol. BFG.

METHODS

The development stages of the monitoring system were discussed to identify changes in combustion conditions, mainly scales, burners, and camera set-up. Next, monitoring system fundaments (image sensor, image processing, and predictive models) were assessed in the different development stages, considering condition changes among them. The evaluation procedure is explained as follows.

- Image sensors were assessed by comparing flame images for different combustion conditions. In addition, the simulated and actual views of the furnace were analysed.
- Image processing effectiveness was assessed by analysing relationships between combustion conditions and extracted image features.

- Finally, the performance of predictive models was validated by comparing their accuracy values. Accuracy was defined as the number of correct predictions divided by the total number of predictions.

RESULTS AND DISCUSSION

Review of the development

The imaging system was evaluated in different scenarios during its development in order to assess its viability and robustness. Therefore, different scales, burner types, and camera locations were tested, while the imaging system shared several properties during the development stages. This approach differs from the usual validation of a burner, in which the burner typology and characteristics are constant.

A colour camera was employed as the image sensor. The processing algorithm extracted statistical features from the three colour channels of the flame images. In some cases, additional textural and geometrical characteristics were computed. A predictive model was tested to predict O_2 concentration in flue gases for each fuel blend, choosing between three different ML algorithms. A subset of image features was automatically selected to feed the predictive model of each fuel blend. The image sensor, image processing, and predictive model are described in more detail in the next sections. The development stages of the flame monitoring system are summarised in Table 1.

Table 1. Development stages of the flame monitoring system

Stage	Scale	Burner	Camera placement
Design	Semi-industrial	Diffusion	Outside
Development	Laboratory	Premixed	Outside
Implementation	Semi-industrial	Diffusion	Inside

The first stage included the design requirements for the monitoring system. With that purpose, an experimental campaign was performed at a semi-industrial scale with a diffusion burner of 1.2 MW. This type of burner is characterised by the production of soot and its continuous radiation (black-body emission) [14, 15]. The camera was set outside the furnace, aligned with a viewing port to acquire flame images. The experimental campaign and its results are presented in a previous work [16].

The second phase focused on developing the predictive model with an experimental campaign at the laboratory scale. A combustion chamber with a premixed burner of 20 kW was used in this stage. Premixed burners provide flames that mainly emit several discrete radiations due to chemiluminescence [15, 17]. The camera was placed outside the combustion chamber before an inspection window. The analysis of these image features is included in another work [18].

Lastly, in the implementation stage, a predictive model was developed for the semi-industrial scale performing another experimental campaign. As in the design phase, a diffusion burner of 1.2 MW was employed. However, the camera was set inside the furnace in this case.

Image sensor

Examples of flame images acquired during all the development stages are shown in Figure 1.

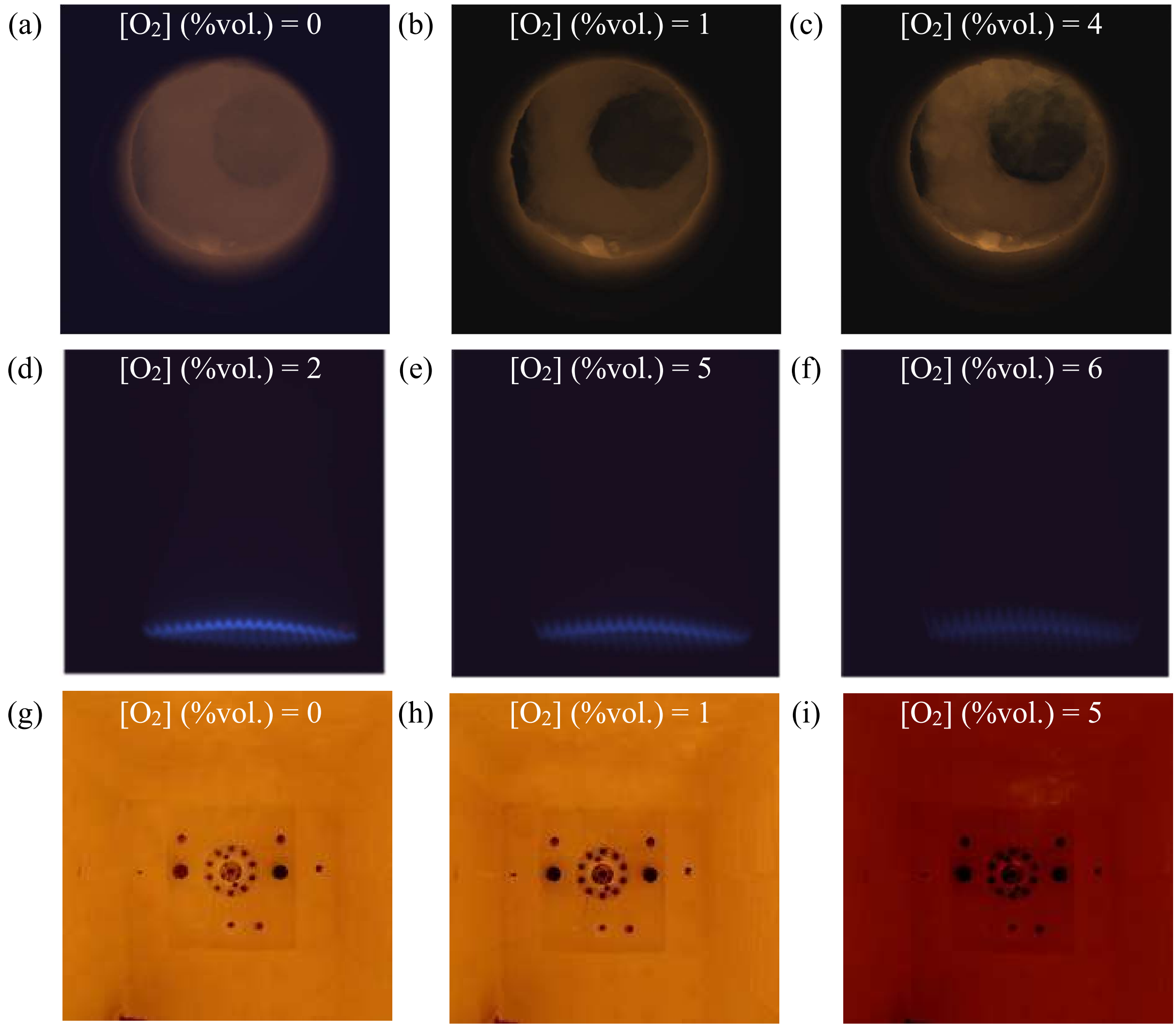

Figure 1. Examples of flame images for different O_2 concentrations in flue gases for semi-industrial and laboratory scales, with the fuel blend 70 %vol. BFG and 30 %vol. NG. For the semi-industrial scale, the ((a), (b), and (c)) outside and ((g), (h), and (i)) inside placements of the camera were used, while for laboratory scale, an ((d), (e) and (f)) outside set-up was employed

For the semi-industrial scale, flames had low visibility, but overall image characteristics were affected. For example, the brightness of the images was decreased by raising the O_2 concentration in flue gases with the outside and inside camera locations. At the laboratory scale, images captured a flame body and clear flame front for all combustion conditions. For both diffusion and premixed burners, the images differed depending on the combustion conditions. Therefore, the colour camera was validated as an image sensor for monitoring BFG combustion for diffusion and premixed burners.

At the semi-industrial scale, the burner typology (diffusion) was fixed, but the camera port used to visualize the flame differed. In the design stage, the small size of the viewing port and the outside location affected the camera view, and only part of the furnace inside was captured. For the implementation phase, the captured area of the furnace was maximised by placing the camera inside the furnace. This location was also simulated based on the camera placement and furnace geometry to check the field of view before the physical setup of the system, as seen in Figure 2. The simulation provided an accurate estimation of the captured area of the furnace.

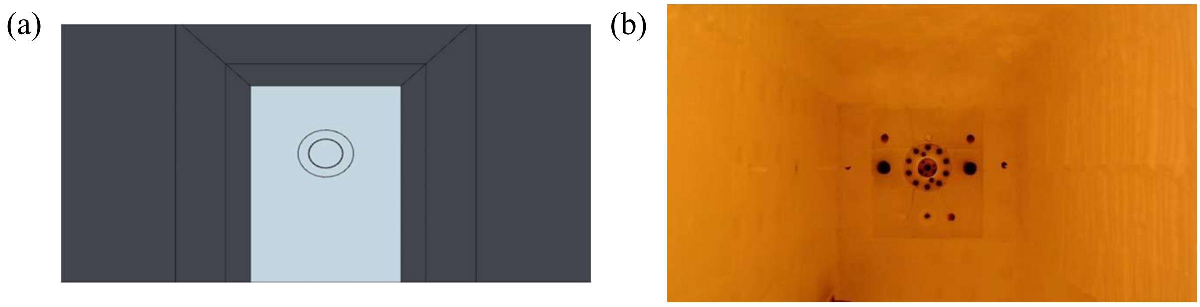

Figure 2. (a) Simulated and (b) actual views of the inside of the furnace at the semi-industrial scale for the image sensor set-up

Image processing

The same statistical features were extracted from the three colour channels of flame images for all the development stages. Textural and geometrical features were also computed from the three colour channels in some cases (Table 2).

Table 2. Summary of computed image characteristics

Stage	High flame visibility	Statistical features	Textural features	Geometrical features	Total image features
Design	-	Yes	-	-	12
Development	Yes	Yes	Yes	Yes	66
Implementation	-	Yes	Yes	-	51

First, flame segmentation was only applied to the laboratory scale due to the high visibility of the flame. Therefore, features were computed at the laboratory scale using only flame pixels, while at the semi-industrial scale, all the image pixels were processed. The same statistical features (mean, standard deviation, skewness, and kurtosis) were extracted for all the development stages. The textural features computed for laboratory and semi-industrial scales were based on thirteen selected characteristics [19]. The application of flame segmentation at the laboratory scale enabled the use of geometrical features from which flame area, centroid coordinates, width, and height were extracted. All the image features were computed for each colour channel, with 12, 66, and 51 features for each development phase. Figure 3 shows, as an example, the relationship between O_2 concentration in flue gases and the image feature of the red mean for the 70 %vol. BFG/30 %vol. NG fuel blend. This characteristic was selected as an illustrative example since it is extracted in all the development stages.

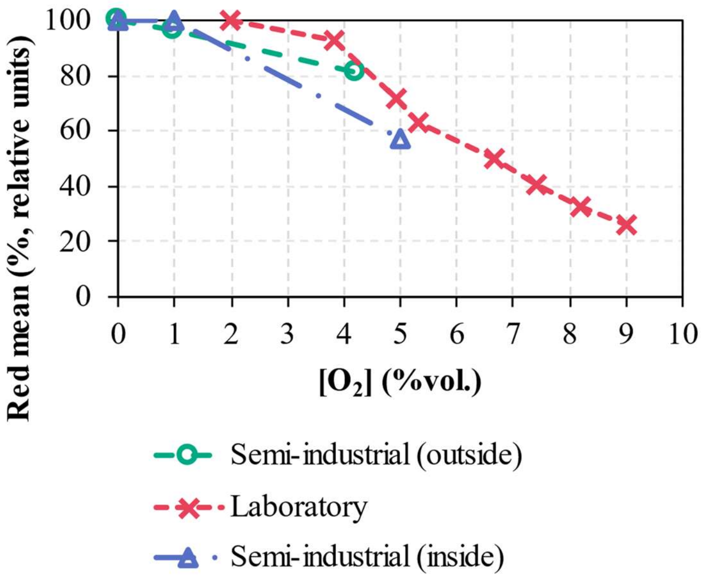

Figure 3. O_2 concentration in flue gases vs. red mean for semi-industrial and laboratory scales, during the combustion of the fuel blend 70 %vol. BFG and 30 %vol. NG. For the semi-industrial scale, the outside and inside placements of the camera are shown

In all the development stages, image features were affected by the combustion conditions. Statistical and textural features were validated as descriptors of combustion conditions for flames with high and low visibility, respectively.

Predictive model

Predictive models were trained to predict O_2 concentration in flue gases for the laboratory and semi-industrial scales. At the semi-industrial scale, the predictive model was developed only for the inside location of the camera (implementation stage) due to the lower amount of flame images captured for the outside set-up (design phase). Five, seven, and eight O_2 classes were studied at a laboratory scale for each fuel blend, while only three classes were considered at a semi-industrial scale. The same methodology was followed for laboratory and semi-industrial scales, explained next.

Three ML algorithms with different characteristics were analysed: Logistic Regression (LR), Support Vector Machines (SVM), and a MultiLayer Perceptron (MLP) with a single hidden layer of a hundred neurons as an artificial neural network. The predictive models were trained, validated, and tested with the datasets of image features. The dataset of each fuel blend was randomly shuffled and split into training and test sets.

In the training set, a subset of image features was automatically selected as input. Each subset of image characteristics comprises the ten variables with the highest variance for the combustion conditions. The training set was also used to tune model hyperparameters and evaluate the performance employing nested Cross-Validation (CV). The nested CV included an outer CV of 10 folds and an inner CV of 5 folds. The training set was split again into 10 pairs of training and validation subsets for the outer CV. For each training subset, the inner CV was used to define the best hyperparameter combination. Next, the selected hyperparameters were employed to train the predictive model with the training subset and measure its accuracy in predicting the O_2 concentration for the validation subset. The accuracy was averaged for every validation subset, providing a single value for each ML algorithm and scale, as shown in Table 3.

Table 3. Nested CV accuracies of the predictive models for different BFG shares (%vol.) in the fuel blend at laboratory and semi-industrial scales

BFG share (%vol.)	Laboratory predictive model			Semi-industrial (inside) predictive model		
	LR	SVM	MLP	LR	SVM	MLP
0	0.9485	0.9667	0.9600	0.9920	0.9936	0.9866
70	0.9679	0.9734	0.9693	0.9666	0.9671	0.9640
80	-	-	-	0.9970	0.9980	0.9962
100	0.7749	0.7949	0.7904	-	-	-

The nested CV accuracy of the predictive models was higher than 0.77 for all the cases and development stages, showing values higher than 0.94 for BFG shares in the fuel blend lower than 90 % vol. at both laboratory and semi-industrial scales. This accuracy was achieved even for flames with low visibility and slight combustion variations that the human eye did not perceive. The increase in accuracy for the semi-industrial scale could be explained by the complexity reduction in the classification task concerning the laboratory scale. In this work, the classification task for the semi-industrial scale may be easier due to the lower number of classes to predict, the more significant image differences between classes, or the lower maximum concentration of BFG in the fuel blend (80 instead of 100 %vol.).

The three ML algorithms achieved similar accuracies in the nested CV, with differences lower than 5%. Nevertheless, SVM reached the highest accuracy for every fuel blend. The performance of this particular ML algorithm was assessed again. Predictive models were trained with the whole training set, and their accuracy was evaluated in predicting O_2 concentration for the test set (Figure 4).

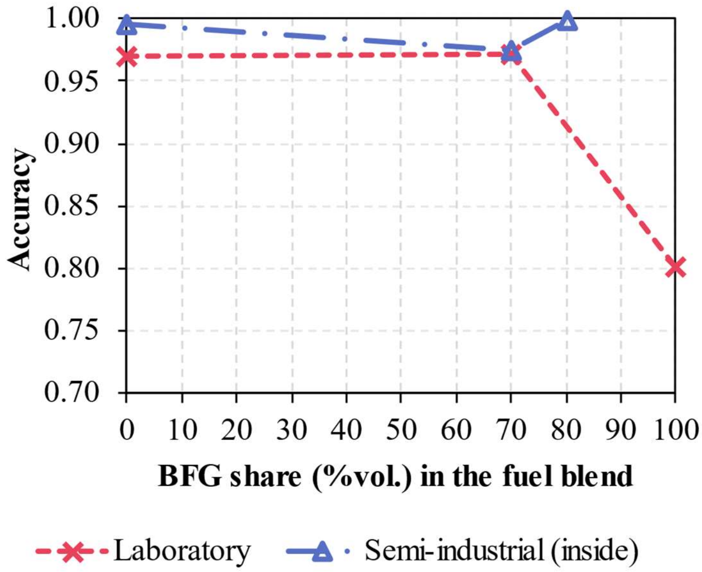

Figure 4. Test accuracies of the predictive models vs. BFG share (%vol.) in the fuel blend for laboratory and semi-industrial scales

To conclude, the defined methodology and the ML algorithms were tested for laboratory and semi-industrial scales. In addition, using ML algorithms with lower complexity (LR and SVM) did not provide significant changes in performance with respect to the MLP.

CONCLUSIONS

An advanced image system for combustion monitoring in the steel industry has been validated at laboratory and semi-industrial scales. The system´s robustness has been assessed by analysing results along the design, development, and implementation stages, identifying condition changes between them. The relationships between combustion conditions, flame images, image features, and performance of predictive models were analysed.

Colour cameras were proven as reliable sensors for monitoring BFG combustion on laboratory and semi-industrial scales, and the simulation of the furnace view was also accurate. For both scales, extracted image features were affected by combustion conditions, and the statistical and textural features provided adequate descriptors of the combustion for images with high and low flame visibility. The predictive models generally achieved accuracy higher than 0.95, with 0.79 as the minimum. The defined methodology was adequate for the two scales, and using ML algorithms with lower and higher capacities did not achieve relevant performance differences. The image processing and predictive models enabled the monitoring of flames with low visibility and slight combustion variations that the human eye did not perceive in the images. In summary, the imaging system was robust and overcame condition changes along the development stages, including scale (lab and semi-industrial), burner type (diffusion and premixed), and camera placement (outside and inside).

With this work, several research lines have been opened for future studies. The monitoring system could be enhanced by simultaneously supervising several burners within the same image. In addition, experimental campaigns at an industrial scale could be performed to increase the technological readiness of the system for the industry.

ACKNOWLEDGMENT

This work has been supported by the European Union's Horizon 2020 Research and Innovation Programme under Grant Agreement No. 820771 (BAMBOO project) and 869939 (RETROFEED project).

NOMENCLATURE

BFG – Blast Furnace Gas, CV – Cross-Validation, LR – Logistic Regression, ML – Machine Learning, MLP – MultiLayer Perceptron, NG – Natural Gas, O_2 – Oxygen, SVM – Support Vector Machine

REFERENCES

1. Li, Y., Zhang, X. and Wang, Y., Experimental Study on the Combustion Characteristics of Premixed Methane-Hydrogen-Air Mixtures in a Spherical Closed Chamber, *Fuel*, Vol. 299, 2021.
2. Zhang, X., Hou, X., Wang, Y. and Zhang, J., Study on Flame Characteristics of Low Heat Value Gas, *Energy Convers. Manag.*, Vol. 196, pp 344-353, 2019.
3. Han, Z., Hossain, M.M., Wang, Y., Li, J. and Xu, C., Combustion Stability Monitoring through Flame Imaging and Stacked Sparse Autoencoder Based Deep Neural Network, *Appl. Energy,* Vol. 259, 2020.
4. Abdurakipov, S.S., Gobyzov, O.A., Tokarev, M.P. and Dulin, V.M., Combustion Regime Monitoring by Flame Imaging and Machine Learning, *Optoelectron. Instrument. Data Process.*, Vol. 54, No. 5, pp.108-115, 2018.
5. Yang, G., He, Y., Li, X, Liu, H. and Lan, T., Gabor-GLCM-Based Texture Feature Extraction Using Flame Image to Predict the O2 Content and NOx, *ACS Omega*, Vol. 7, pp 3889–3899, 2022.
6. Bai, X., Lu, G., Hossain, M. M., Szuhánszki, J., Daood, S. S., Nimmo, W., Yan, Y. and Pourkashanian, M., Multi-Mode Combustion Process Monitoring on a Pulverised Fuel Combustion Test Facility Based on Flame Imaging and Random Weight Network Techniques, *Fuel*, Vol. 202, pp 656–664, 2017.
7. Slefarski, R., Czyzewski, P. and Golebiewski, M., Experimental Study on Combustion of CH4/NH3 Fuel Blends in an Industrial Furnace Operated in Flameless Conditions, *Thermal Science*, Vol. 24, pp 3625-3635, 2020.
8. Cuervo-Piñera, V., Cifrián-Riesgo, D., Battaglia, V., Fantuzzi, M., Della-Rocca, A., Ageno, M., Rensgard, A., Wang, C., Niska, J., Ekman, T., Rein, C. and Nguyen, P. D., *High Efficiency Low NOX BFG Based Combustion Systems in Steel Reheating Furnaces (HELNOx-BFG)*, European Commission, Directorate-General for Research and Innovation, final report, Publications Office, 2018.
9. Caillat, S., Burners in the Steel Industry: Utilization of By-Product Combustion Gases in Reheating Furnaces and Annealing Lines, *Energy Procedia*, Vol. 120, pp 20–27, 2017.
10. Cuervo-Piñera, V., Cifrián-Riesgo, D., Nguyen, P.D., Battaglia, V., Fantuzzi, M., Della-Rocca, A., Ageno, M., Rensgard, A., Wang, C., Niska, J., Ekman, T., Rein, C. and Adler, W., Blast Furnace Gas Based Combustion Systems in Steel Reheating Furnaces, *Energy Procedia*, Vol. 120, pp 357–364, 2017.
11. Zheng, W., Pang, L., Liu, Y., Xie, F. and Zeng, W., Effects of Initial Condition and Fuel Composition on Laminar Burning Velocities of Blast Furnace Gas with Low Heat Value, *Fuel*, Vol. 289, 2021.
12. Zheng, W., Pang, L., Liu, Y., Xie, F., and Zeng, W., Effects of Methane Addition on Laminar Flame Characteristics of Premixed Blast Furnace Gas/Air Mixtures, *Fuel*, Vol. 302, 2021.
13. Zhang, L., Xie, W. and Ren, Z., Combustion Stability Analysis for Non-Standard Low-Calorific Gases: Blast Furnace Gas and Coke Oven Gas, *Fuel*, Vol. 278, 2020.
14. He, L., Guo, Q., Gong, Y., Wang, F. and Yu, G., Investigation of OH* Chemiluminescence and Heat Release in Laminar Methane-Oxygen Co-Flow Diffusion Flames, *Combust. Flame*, Vol. 201, pp 12– 22, 2019.
15. Huang, H. W. and Zhang, Y., Digital Colour Image Processing Based Measurement of Premixed CH 4 + Air and C2H4 + Air Flame Chemiluminescence, *Fuel*, Vol. 90, No. 1, pp 48– 53, 2011.
16. Compais, P., Arroyo, J., González-Espinosa, A., Gonzalo-Tirado, C., Castán-Lascorz, M.A., Barrio, J. and Cuervo-Piñera, V., Experimental Analysis of Blast Furnace Gas Co-Firing in a Semi-Industrial Furnace using Colour Images, *Proceedings of the 7th World Congress on Momentum, Heat and Mass Transfer*, April 7-9, 2022.

17. Tripathi, M. M., Krishnan, S. R., Srinivasan, K. K., Yueh, F. Y., and Singh, J. P., Chemiluminescence-Based Multivariate Sensing of Local Equivalence Ratios in Premixed Atmospheric Methane-Air Flames, *Fuel*, Vol. 93, pp 684– 691, 2012.
18. Compais, P., Arroyo, J., González-Espinosa, A., Castán-Lascorz, M.Á. and Gil, A., Optical Analysis of Blast Furnace Gas Combustion in a Laboratory Premixed Burner, *ACS Omega*, Vol. 7, 2022.
19. Haralick, R.M., Shanmugam, K. and Dinstein, I., Textural Features for Image Classification. *IEEE Trans. Syst. Man Cybern*. Vol. SMC-3, pp 610–621, 1973.

2.4. Artículo IV

Promoting the valorization of blast furnace gas in the steel industry with the visual monitoring of combustion and artificial intelligence. P. Compais, J. Arroyo, F. Tovar, V. Cuervo-Piñera, A. Gil. **Fuel** (2024); Vol. 362, 130770.

Fuel 362 (2024) 130770

Contents lists available at ScienceDirect

Fuel

journal homepage: www.elsevier.com/locate/fuel

Full Length Article

Promoting the valorization of blast furnace gas in the steel industry with the visual monitoring of combustion and artificial intelligence

P. Compais [a], J. Arroyo [a,*], F. Tovar [a], V. Cuervo-Piñera [b], A. Gil [c]

[a] CIRCE Technology Center, Parque Empresarial Dinamiza Avenida Ranillas, 3D 1ª Planta, 50018 Zaragoza, Spain
[b] ArcelorMittal, PO Box 90, Avilés 33480, Spain
[c] Universidad de Zaragoza, IUI mixto CIRCE, Campus Rio Ebro, Mariano Esquillor Gómez, 15, 50018 Zaragoza, Spain

ARTICLE INFO

Keywords:
Combustion monitoring
Predictive model
Color images
Industrial furnace
Steelmaking processes
Machine learning

ABSTRACT

The sustainability and decarbonization of processes in the steel industry are enhanced with the valorization of the gas generated during the chemical reactions produced in blast furnaces. However, the combustion of blast furnace gas (BFG) faces the drawback of lower flame stability, which increases the chance of operation shifts towards abnormal conditions and even the flashback or extinction of the flame. Thus, early detection and correction of regime deviations are needed to increase combustion efficiency, for which image-based systems have a high potential. This work focuses on monitoring an industrial furnace for steelmaking processes based on estimating O_2 concentration in flue gases using color images captured inside the combustion chamber. An experimental campaign was performed in a 1.2-MW burner to develop the supervision system, using three fuel blends of BFG and natural gas. Images were processed to extract intensity and textural features, which were used to train predictive models based on machine learning algorithms: logistic regression, support vector machines, and artificial neural networks (multilayer perceptron). O_2 concentration in flue gases was correctly estimated for at least 97 % of all the test samples and fuel blends. This study shows the potential of image-based systems for the automated control of BFG combustion at the industrial scale.

1. Introduction

Steel is crucial in modern societies as the third most manufactured bulk material, with 1.9 billion tons of world yearly production [1]. Steelmaking is also an energy-intensive industry, accounting for 8 % of global energy demand and 7 % of CO_2 direct emissions from the worldwide energy system. Reducing these quantities is urgent for the European Union, the second-largest steel producer. Consequently, Europe has ambitious targets for steel decarbonization, cutting emissions by 55 % by 2030 and reaching climate neutrality by 2050. Several strategies can help achieve these objectives, such as valorizing gaseous waste streams from the steel production processes. Blast furnaces, used in the basic oxygen steelmaking process to reduce iron ore, are a significant source of waste streams. Chemical reactions inside blast furnaces generate a by-product, the blast furnace gas (BFG), which can be used as fuel in other steelmaking furnaces, reducing natural gas (NG) consumption.

BFG differs from traditional fuels in its large concentration of inert gases and low calorific value. With a typical composition of 1–7 %vol. H_2, 18–25 %vol. CO_2, and 20–28 %vol. CO, balanced with N_2 [2], BFG has a lower heating value (LHV) around 3.3 MJ/Nm^3, one-tenth the calorific value of NG. Even though BFG reduces the thermal energy released during combustion, it can be used in high-temperature processes (such as steel reheating furnaces) by adopting multiple strategies. These solutions include its mixture with NG or coke oven gas (COG) [3], preheating of the combustion air [4], flameless combustion [5,6], and the use of several burner technologies (oxy-fuel, double regenerative and regenerative flat flame) [7].

The combustion of BFG and low-calorific fuels has been analyzed in the past by several numerical and experimental approaches. Regarding the steel industry, BFG and other by-product combustion gases were analyzed by Caillat [3] for their use in reheating furnaces and annealing lines. The study discussed the constraints due to the by-products' variable composition and physical properties. Cuervo-Piñera et al. [7] tested three burner technologies (oxy-fuel, double regenerative, and regenerative flat flame) for the combustion of BFG in steel reheating furnaces. The trials successfully proved the operation of these furnaces with only BFG, supplying oxygen or meeting other specific conditions. However,

* Corresponding author.
E-mail address: jarroyo@fcirce.es (J. Arroyo).

https://doi.org/10.1016/j.fuel.2023.130770
Received 31 October 2023; Received in revised form 13 December 2023; Accepted 26 December 2023
Available online 5 January 2024

the economic viability of these alternatives should be checked for each facility, considering fuel saving, oxygen consumption, burner replacement, and retrofitting investment. The combustion of BFG/NG fuel blends was also simulated and validated for a semi-industrial furnace in the steel sector [8]. The authors analyzed velocity, temperature, OH and O_2 concentrations, and NO_x rate generation. The significant differences in the LHV of the fuel blend modified combustion fluid dynamics, affecting flow pattern, heat transfer, and temperature gradients in the furnace and, thus, process quality. Other works also analyzed the BFG combustion more broadly outside the steel industry. For instance, laminar flame characteristics were studied for several initial conditions and fuel compositions [2]. Moreover, composition, temperature, and fuel-switching effects were evaluated for the combustion stability of hot air heaters [4]. A critical ambient temperature was maintained to achieve stable combustion, which can be reduced by increasing the H_2 proportion in the blend from 1 to 5 %vol. Furthermore, mixtures of BFG and COG required a large concentration of BFG, higher than 80 %vol., to inhibit temperature oscillations.

Indeed, another consequence of the low LHV of BFG is the appearance of combustion instabilities [2,4]. Thus, disturbances under regular furnace operation may cause more severe deviations than other higher volumetric-energy density fuels. Early detection of these changes is essential to adjust the process quickly and reduce the period under suboptimal conditions, optimizing the overall operation. Thus, monitoring fuel blends with BFG is particularly interesting due to its lower combustion stability. In this aspect, image-based systems are a promising alternative to detect early deviations when burning fuels blended with BFG.

Image-based systems are essential in the state-of-the-art of combustion monitoring. This technology relies upon acquiring flame images and their correlation with combustion conditions. For example, images have been employed to estimate variables related to the air–fuel equivalence ratio, such as the air ratio [9], combustion regimes [10,11], and O_2 concentration in flue gases ($[O_2]_{fg}$) [12]. In contrast to conventional sensors, a single camera could simultaneously monitor several burners captured in the same picture. To monitor the combustion, image-based systems perform several activities employing computer vision and machine learning (ML). Like other industrial problems, these tasks can be categorized into image acquisition, pre-processing, segmentation, feature extraction, and interpretation [13]. ML techniques lead the interpretation step, in which image features are transformed (modeled) into variables related to the combustion process. Nowadays, ML provides a set of horizontal techniques for data analysis and modeling. For example, in the field of combustion, ML has been used to predict operation parameters [14], exhaust gas temperature [15], emissions [16,17] and performance [16–18]. Unlike most literature research, the application of computer vision and ML techniques is limited for commercial camera systems installed in the industry. For example, market tools do not include the interpretation step, which depends on a human worker to analyze the information. Moreover, software suppliers generally do not include segmentation and feature extraction tools.

Image-based systems have also been used to monitor BFG combustion. Zheng et al. [2] employed a high-speed camera to compute the laminar burning velocity of BFG fuel blends. Earlier work by the authors [19–21] focused on image monitoring for steel industry applications. In this aspect, a preliminary study assessed the feasibility of combustion monitoring with a color camera in an industrial furnace [19]. At the laboratory scale, emission spectra, color, and radical images were captured and deeply analyzed for optical supervision of BFG combustion, showing strong dependencies with BFG concentration and equivalence ratio [20]. Furthermore, slight combustion variations were detected with accuracies from 0.78 to 0.97, processing flame images and training predictive models [21].

Nevertheless, monitoring BFG combustion at the industrial scale has not been studied in detail in the open literature. Therefore, image processing requires further analyses to tackle differences between lab and industrial levels. This work focuses on that research gap and proposes an image-based system to predict BFG combustion states to increase steelmaking process efficiency and address industry particularities. Trials are performed to analyze the new image processing with an experimental industrial furnace and a 1.2 MW burner used in steel production. A commercial vision system with a transfer device, cooling, and control unit acquired color images of flames, which are processed to predict $[O_2]_{fg}$ by ML algorithms. In addition, image processing is analyzed for the optimum fuel blend under controlled emissions and transient temperature states. The monitoring system is evaluated for three fuel blends under steady emissions and temperature conditions.

In this work, natural gas was used as a baseline, and two blends (70 and 80 BFG %vol.) were studied. These blends are extracted from the blast furnace line of the Asturias plant and are used by ArcelorMittal in their industrial processes to reduce natural gas consumption. The study will aid in promoting higher valorization of BFG and lower NG consumption in steelmaking industries. This contributes to reducing the pollutant emissions from fossil fuels, while a subproduct of the steel production process is valorized within the same plant where it is produced. From a global perspective, large amounts of process gas (BFG), which can be used as fuel in steel production processes, are available at steel production plants [22]. For the case of the ArcelorMittal Asturias plant, it has been estimated that the use of the whole amount of BFG in the steel production processes would involve a reduction of 52.8 kWh per ton of steel produced, with savings of 2.6 € per ton of steel and a decrease of 13.2 kg of CO_2 equivalent per ton of steel.

2. Material and methods

2.1. Experimental setup

The results presented in this work were obtained during a test campaign performed in an industrial testing furnace installed in the facilities of the ArcelorMittal Asturias plant in Spain (Fig. 1). The combustion chamber has the following dimensions: 4.6 m in length, 1.5 m in width, and 2.8 m in height. The furnace accepts different burners up to 1.2 MW of thermal input power and maximum working temperatures of around 1350 °C. These burners can be fueled with NG and with the off-process gases produced in the plant (COG and BFG). Using the same fuels as in the large plant ensures realistic results and avoids issues related to changes in gas composition at different scales. This way, the solution can be scaled up to other plant furnaces without this problem [8].

In the experimental trials, a diffusion burner is employed (Fig. 2). It allows the use of various gaseous fuel blends utilizing different fuel and air injection configurations. In particular, the burner has one central lance, two side lances for fuel, and multiple air inlets.

A water circuit with six semi-circular lances simulates the heat transferred from an industrial furnace to a steel strip. The water enters the circuit through the nearest lance to the burner and increases in temperature as it flows through the other conducts. At the end of the circuit, a fluid cooler reduces the water temperature before being reintroduced to the lances. The furnace has a control and data acquisition system for registering flow, temperatures, pressure, oxygen concentration in flue gases ($[O_2]_{fg}$), and pollutant emissions (CO, NO_x, SO_2, and CO_2). Five thermocouples measure combustion chamber temperature (T_{cc}) at different locations. The furnace can be configured to work with different gaseous blends and allows testing different configurations, such as preheated combustion air and O_2 injection.

Fuels with different compositions are tested in the experimental furnace. They are identified as 100 %vol. NG (BFG0), 30 %vol. NG and 70 %vol. BFG (BFG70), and 20 %vol. NG and 80 %vol. BFG (BFG80). BFG0 and BFG70 were also studied in a previous work [8]. BFG is extracted, filtered, and fed to the furnace directly from the plant's blast furnaces. Its composition is subjected to variability, influenced by the chemical processes inside the blast furnace [7]. A typical composition and LHV of the fuel blends are shown in Table 1.

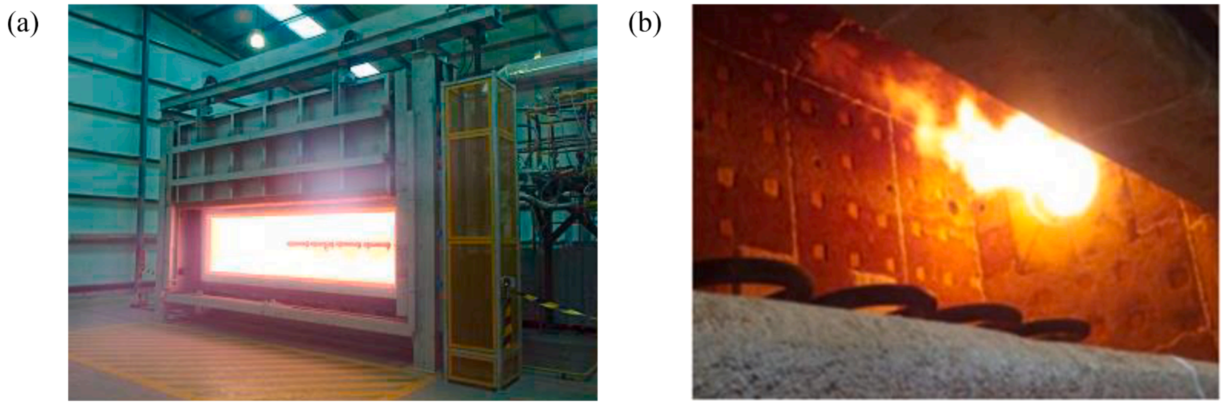

Fig. 1. The ArcelorMittal experimental furnace used for the tests [23].

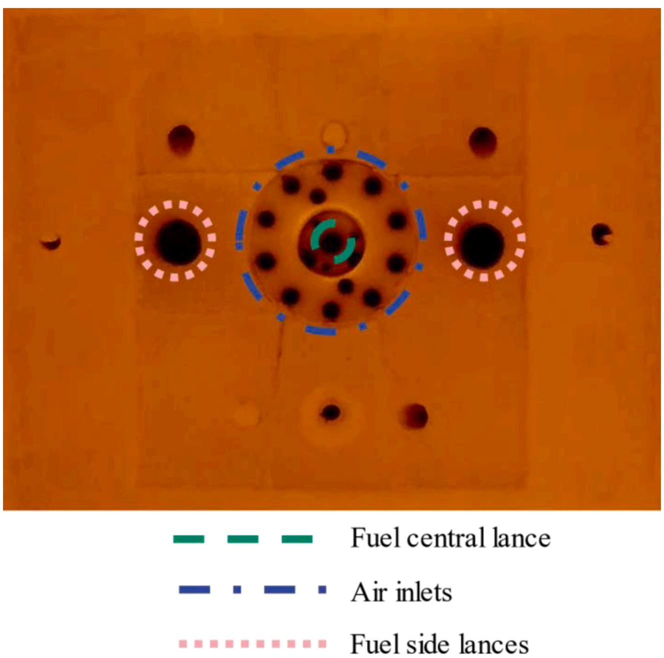

Fig. 2. View of the diffusion burner installed in the furnace.

Table 1
Fuel blends typical composition.

Fuel blend	BFG0	BFG70	BFG80
[CH_4] (%vol.)	92	28	18
[C_2H_6] (%vol.)	8	2	2
[N_2] (%vol.)	–	34	39
[CO] (%vol.)	–	16	18
[CO_2] (%vol.)	–	15	18
[H_2] (%vol.)	–	3	3
[H_2O] (%vol.)	–	1	1
[O_2] (%vol.)	–	1	1
LHV (MJ/Nm^3)	38	14	10

The increase of BFG share in the fuel blend reduces NG consumption, leading to savings in fossil fuel consumption. However, higher concentrations of BFG raise difficulties in reaching the high temperatures needed during the steel production process. Additionally, the lower calorific value of BFG requires higher gas flow rates to meet the thermal energy demands, which could potentially result in operational issues in larger furnaces. Therefore, the use of BFG in the fuel blend is limited, and a certain NG share is required to ensure a stable operation. Considering this, BFG70 was defined as the optimum fuel blend. BFG80 was studied as an operative but suboptimal fuel, while BFG0 was analyzed as a baseline.

A commercial camera system was deployed inside the furnace through a viewing port in front of the burner. The devices included a BASLER BIP2-1920c color camera. The camera has a CMOS sensor, which provides a resolution of 2 MP at 30 frames per second. The camera is protected by a water-cooled metallic case installed on a SOBOTTA automatic transfer device which allows the introduction and extraction of the system inside the furnace. This device protects the optical system by retracting the camera from the furnace when detecting harmful temperatures or system malfunctions.

The image acquisition parameters of the camera were fixed during all the trials to obtain equivalent and comparable images. As a first step, the configuration of the exposure time was optimized by analyzing images and histograms under different conditions, avoiding under- or over-exposed images under any condition.

A data acquisition software recorded the images synchronously to measured variables (process information such as furnace temperatures, gas/air flow rates, pollutants or oxygen concentrations).

2.2. *Methods*

This section includes the methodology used in the research for furnace operation and flame processing.

2.2.1. *Furnace operation*

The furnace was pre-heated before the tests to reach steady conditions for emissions and temperature. Temperature was evaluated by averaging the measures of T_{cc} on five different points. Flue gas emissions stabilized thirty minutes after the start, but the temperature remained transient. When the heating reached 8 h, both emissions and temperature were constant. These two working conditions were labeled steady emissions and transient temperature (SETT) and steady emissions and steady temperature (SEST). The fuel flow rate (and, consequently, the calorific power rate introduced) was constant for each fuel blend. In contrast, the air-flow rate was slightly modified to reach different operation conditions. This resulted in different amounts of excess oxygen in flue gases ($[O_2]_{fg}$), depending on the blend composition and the combustion stoichiometry. Table 2 lists the tests' working conditions, fuel blends, combustion modes, and $[O_2]_{fg}$ concentrations in flue gases.

Each fuel blend under SEST conditions was tested for 0, 1, and 5 % vol. $[O_2]_{fg}$ (sub-stoichiometric, near-stoichiometric and over-stoichiometric conditions). Moreover, BFG70 was studied under SETT state for 1, 2, 3, 4, and 5 %vol. $[O_2]_{fg}$.

Fuel was injected through the central lance for all tests except for BFG80. Main and side burner lances were employed to improve the burner operation with that fuel blend, which implies different

Table 2
Summary of the experimental tests.

Campaign	EXP1	EXP2	EXP3	EXP4
Working condition	SEST	SEST	SEST	SETT
Fuel blend	BFG0	BFG70	BFG80	BFG70
Combustion mode	Regular	Regular	Flameless	Regular
$[O_2]_{fg,1}$ (%vol.)	0	0	0	1
$[O_2]_{fg,2}$ (%vol.)	1	1	1	2
$[O_2]_{fg,3}$ (%vol.)	5	5	5	3
$[O_2]_{fg,4}$ (%vol.)	–	–	–	4
$[O_2]_{fg,5}$ (%vol.)	–	–	–	5

combustion modes. In this configuration, the reactants were strongly diluted with combustion products, and the burner operated in a flameless mode [5]. Flameless combustion is also known as moderate or intense low oxygen dilution (MILD), and it has a more significant reaction zone throughout the combustor volume. This distribution promotes a reduction in peak flame temperature and NO_x emissions [5,24]. The term "flameless" indicates that flames have a lower visibility than conventional flames, but the human eye may still detect them in some cases [24]. For instance, Reddy et al. [25] and Yetter et al. [26] recognized flames under flameless conditions.

Air was preheated at 485 ± 35 °C (21 %vol. O_2 concentration), fuel thermal power varied around 920 ± 15 kW, and T_{cc} around 1285 ± 75 °C. The tests for the three fuel blends provided the same thermal power by modifying the fuel flow rate three to four times higher for BFG70 and BFG80, respectively, compared to BFG0. A 10-minute video was captured during each test, and 1875 flame images were analyzed with an approximate frame rate of 3 images per second. For example, fourteen video fragments (one per test) of 1 s each are available as **supplementary material**. All the fragments are enclosed in a single video, which includes text in each frame to define the associated working condition, fuel blend, and $[O_2]_{fg}$.

2.2.2. Flame processing

Methods for processing flame images are partially based on the feature extraction and interpretation methodology detailed in previous work [21]. However, a significant modification is introduced to adapt the system to the industrial scale by removing the flame-segmentation step.

For the visual monitoring of combustion, flame segmentation is an alternative that can be applied before the feature extraction step. However, its use is not extended to all cases. Flame segmentation classifies image pixels into flame and non-flame groups, enabling the extraction of characteristics from only flame pixels. For instance, Mathew et al. [27] and Katzer et al. [28] employed thresholding to segment flames. Without flame segmentation, features are extracted from the whole image [9,12]. Other works based on deep learning did not perform an explicit flame segmentation, although it could be implicitly included to some extent in the layer operations [10,11]. Bai et al. [9] remarked on the complexity of defining flame boundaries, which can be inaccurate and lead to low performance in monitoring. Identifying the flame body could be easier for flames with more stability and simpler geometry. This is the case of previous authors' work [20], in which flames had a simpler and similar geometry for different combustion conditions. However, image flames processed by Bai et al. [9], Abdurakipov et al. [10], Han et al. [11], and Yang et al. [12] were more diffuse and variable. Therefore, their segmentation could be more complex. Furthermore, the difficulty of flame segmentation also depends on the image background and the appearance of other non-flame elements. For instance, in the studies of Bai et al. [9], Abdurakipov et al. [10], and Han et al. [11], the background was empty, and thus, the classification of pixels into flame and non-flame groups could be more straightforward. Nevertheless, in [19], flames appeared over the furnace background.

To sum up, the complexity of flame segmentation depends on the use case considered in each study. The present research focuses on the same industrial furnace and similar flue blends from the work of Compais et al. [19]. Therefore, segmentation would have the challenge of identifying flames from the furnace background. Moreover, a preliminary inspection of the furnace operation ensured the diffuse and variable geometry of the flames, which would increase the segmentation complexity even more. Thus, due to the high risk of inaccurately identifying flames and lowering the monitoring performance, the present research modifies the procedure of Compais et al. [21] by removing the flame-segmentation step. This more straightforward method could be more suitable for future implementation of the monitoring system at the industrial level, in which unseen flame images and combustion conditions may appear over time.

The flame processing used in this research is summarized in Fig. 3. It consists of extracting 51 features and their interpretation to predict $[O_2]_{fg}$. Flame segmentation is not applied, and image variables are computed from the whole image.

Regarding the feature extraction step, a wide range of image characteristics can be considered for combustion analysis. Standard features are based either on intensity [9,27–29], geometry [28], or texture measures [9,12]. Intensity and texture characteristics can be extracted from the entire image or specific flame pixels. Geometry features generally calculate properties of the flame body, such as length and area [28], and therefore, they require the application of flame segmentation. Usually, each study manually selects a limited group of features tailored to its use case. This work computes a subset of the characteristics from the work of Compais et al. [21], including only those of intensity and textural type. Geometrical features are not analyzed because the present work does not apply flame segmentation. The feature subset comprises 51 variables per color image, and the extraction method is shown in Fig. 4.

The three-color channels of the image (red, green, and blue) are considered separately, analyzing their corresponding monochrome images. Each color channel is processed to extract four intensity features (mean, standard deviation, skewness, and kurtosis of the pixel intensities [21,29]) and compute its gray level co-occurrence matrix (GLCM). This matrix is employed to define thirteen textural features selected from the work of Haralick et al. [30] and also used in other studies [9,21].

Predictive models estimate combustion conditions based on image properties in the final interpretation processing step. With that purpose, the present work uses the same ML method described in [21] to train and test models based on the experimental campaign performed at an industrial scale. The procedure comprises analysis of variance (ANOVA) *F*-tests for feature selection and nested cross-validation (CV) for hyperparameter tuning and performance evaluation. The same ML algorithms analyzed in [21] are tested at an industrial scale in the current work.

Three ML algorithms are studied: logistic regression (LR) [10,11], support vector machines (SVM) [9–11], and artificial neural networks (ANN) [9–11]. A multilayer perceptron (MLP) is defined for the latter with a single hidden layer of 100 neurons. Flame images are labeled according to their associated $[O_2]_{fg}$, and the models classify them into three or five discrete $[O_2]_{fg}$ values. The whole set of images of each experimental campaign is split into training and test sets. The training set is used to automatically select a subset of image characteristics as input, tune hyperparameters, and evaluate the performance of the ML algorithms. Finally, the best algorithm is assessed again, employing the test set. The input subsets of image features include the ten variables with the highest variance for the $[O_2]_{fg}$ classes. These characteristics are selected using ANOVA *F*-tests. The hyperparameter tuning and performance evaluation of the training set are implemented in a nested CV procedure. An outer CV of ten folds splits the training set into ten pairs of training and validation subsets. The accuracy of each training and validation subset is computed and averaged for each ML algorithm. For each training subset, model hyperparameters are selected with an inner CV of five folds. The training subset is split into five pairs of training and

Fig. 3. Method for the processing of flame images.

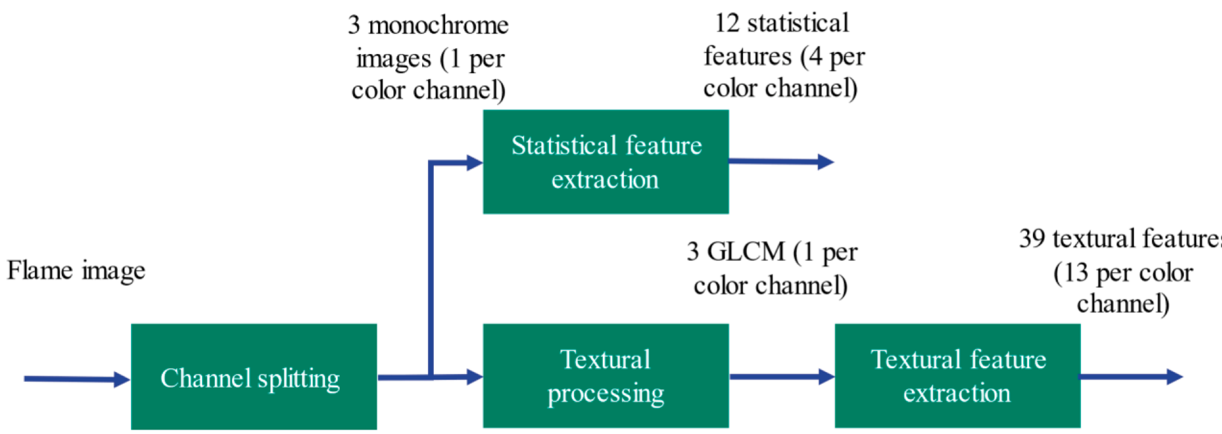

Fig. 4. Method for feature extraction of flame images.

validation subsets, for which several combinations of hyperparameters were evaluated with the model's accuracy. After the nested CV, the ML algorithm with the best performance is analyzed in more detail by computing its confusion matrixes for the validation subsets of the four experimental campaigns. Next, the chosen ML algorithm is re-evaluated with the test set, measuring its test accuracy and comparing it with the achieved for training and validation.

Python is used as a programming language (version 3.7) to develop the code for image processing and predictive models. The following libraries are also employed: OpenCV, Scikit-learn, NumPy, SciPy, Mahotas, and Pandas.

3. Results and discussion

3.1. Flame images for the working conditions, fuel blends, and $[O_2]_{fg}$

Fig. 5 shows flame images captured for SEST conditions and the fuel blends of BFG0, BFG70, and BFG80 at different $[O_2]_{fg}$. In the case of BFG70, images captured for SETT were also studied (Fig. 6). For each working condition (SEST or SETT), fuel blend and $[O_2]_{fg}$, Fig. 5 and Fig. 6 include a single image, which corresponds to the first frame captured in its associated test. Therefore, the images shown were captured at least 8 h or 30 min apart from each other, which are the required time intervals to achieve SEST or SETT conditions, respectively.

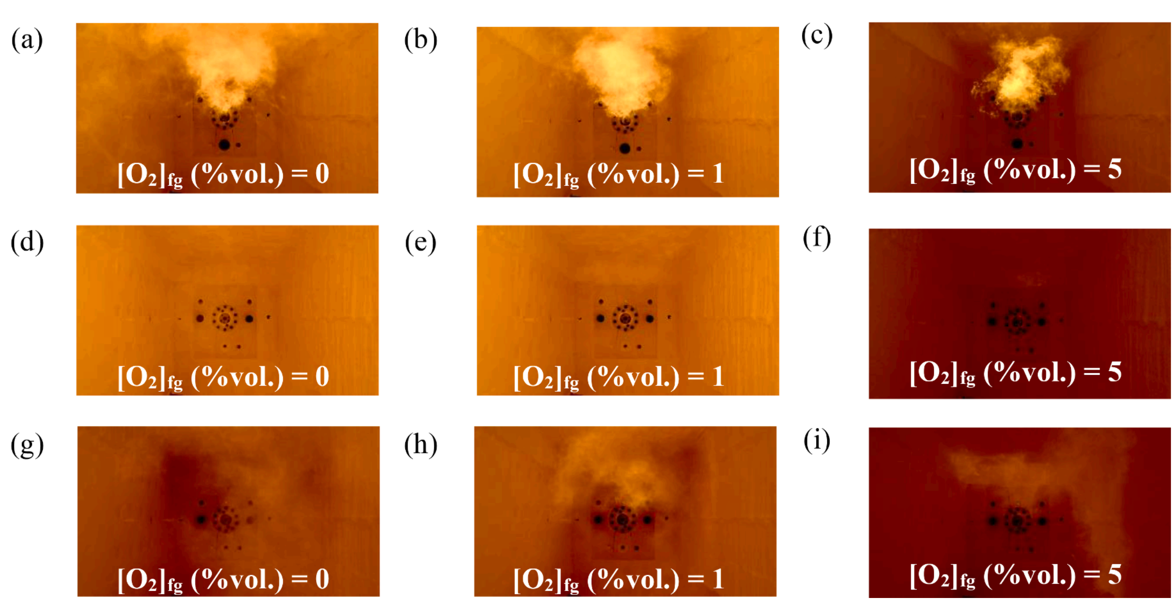

Fig. 5. Flame images for SEST and (a) BFG0, (b) BFG70, and (c) BFG80.

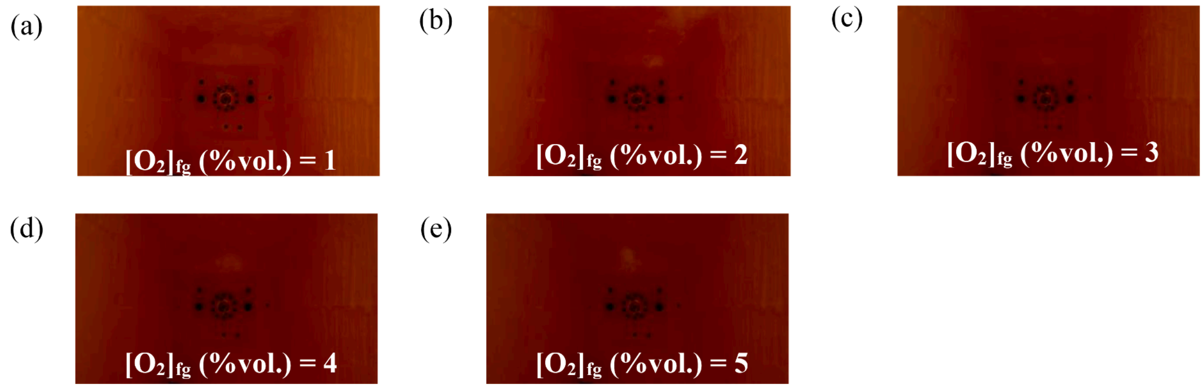

Fig. 6. Flame images for SETT and BFG70 with $[O_2]_{fg}$ of (a) 1, (b) 2, (c) 3, (d) 4, and (e) 5 %vol.

The red color channel predominates over blue and green in diffusion flame images. While premixed flames are bluish and dominated by chemiluminescence, diffusion flames are orangish and characterized by their soot emission [31]. Soot particles emit blackbody radiation [32], ideally described by Planck's law [33]. According to this law, an object at a higher temperature emits higher radiation. Indeed, soot temperature and volume fraction can be retrieved from flame images [34]. The longer period of furnace preheating under SEST conditions caused higher T_{cc} (Fig. 7) and generated brighter images (Fig. 5.e and Fig. 5.f) than SETT ones (Fig. 6.a and Fig. 6.e). In contrast to premixed flames, the color of diffusion flames has a lower dependence on the reactant composition and equivalence ratio [35]. Still, this work detected differences under SEST conditions.

Flames had significantly lower visibility for the fuel blend of BFG70 and BFG80 concerning BFG0. In particular, BFG70 flames in static images were hardly visible to the human eye. In contrast, its capture on video helped their recognition due to the detection of variations in the flame geometry and location in the furnace. The lower visibility of flames for BFG70 and BFG80 is caused by the large volume fraction of inert gases in the fuel, with around 35 %vol. and 15 %vol. of N_2 and CO_2 concentrations, respectively. A similar behavior was detected in [32], where the OH* chemiluminescence peak was reduced when the N_2 dilution for CH_4 diffusion flames was increased. BFG80 images (Fig. 5.g, Fig. 5.h, and Fig. 5.i) also captured the widespread distribution of flames, which is characteristic of flameless combustion.

$[O_2]_{fg}$ was related to $T_{cc,}$ as shown in Fig. 7. In this work, $[O_2]_{fg}$ of 1 %vol. corresponds to near-stoichiometric conditions (where air and fuel flow rates were fixed to produce stoichiometric combustion). Therefore, concentrations below or above that value are related to sub-stoichiometric or over-stoichiometric conditions, respectively. Considering this, temperature trends in Fig. 7 follow the expected behavior of adiabatic flame temperature concerning air–fuel equivalence ratio, reaching maximum temperature for near-stoichiometric conditions.

The brightness of the image increased when the operation moved toward stoichiometric conditions. Both significant and slight image changes were reported based on the temperature variations. For SEST conditions and the same fuel blend, images differed significantly between 1 and 5 %vol $[O_2]_{fg}$. This behavior was slighter for SETT conditions, which reached lower T_{cc} than the SEST regime. Furthermore, in all the tests, images were similar for variations of $[O_2]_{fg}$ around 1 %vol.

3.2. Selection of image characteristics for the estimation of $[O_2]_{fg}$

As described in the methods for flame processing, the initial set of 51 features was manually selected based on the state of the art. To summarize, previous works have monitored combustion with intensity [21,29] and texture features [9,21] considered in this work. The image properties used in this work have been validated for the flame characterization of similar fuel blends at lab scale [21].

From the total of 51 image properties, a subset of ten features was selected using ANOVA *F*-tests. This analysis measured the variance of image features with $[O_2]_{fg}$. Critical *F*-values were computed for each experimental campaign with a 0.05 confidence level, resulting in 3.00 (SEST) and 2.37 (SETT). The critical *F*-value was the same for the tests

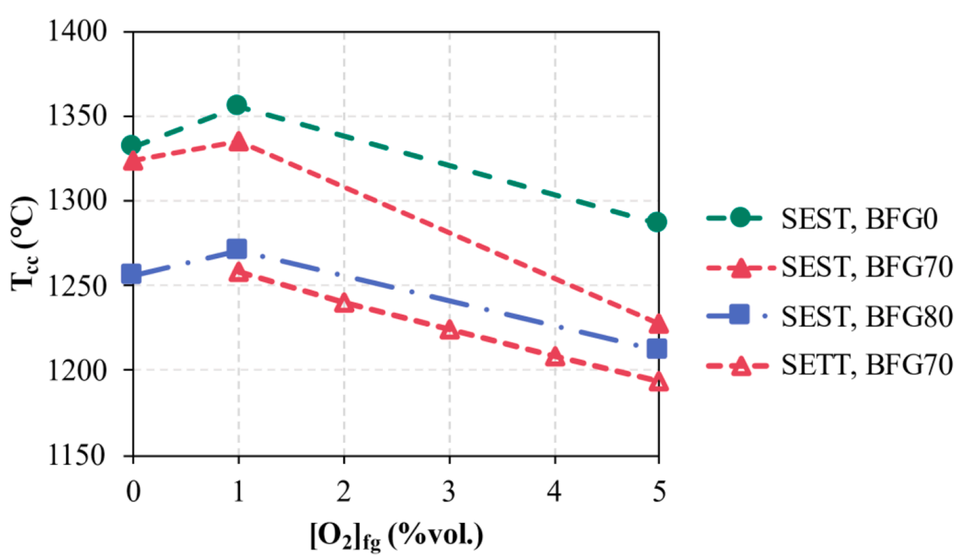

Fig. 7. T_{cc} during the experimental tests.

with SEST conditions because they included the same population (classes of O_2 concentration in flue gases) and number of samples (flame images per experimental campaign). All the *F*-values of image features were at least an order of magnitude higher than the critical *F*-value of their experimental campaign. Therefore, the classes of $[O_2]_{fg}$ affected the mean values of every extracted image feature for regular and flameless combustion. This result proves that the application of flame segmentation was not necessary for these use cases since characteristics from the whole image are effective descriptors of the $[O_2]_{fg}$.

The subset of ten image features with higher *F*-values was used for each experimental campaign to feed predictive models. All the subsets comprise characteristics from the two types of features (intensity and textural) and three-color channels (red, green, and blue), except for SETT. For the latter tests, properties were not computed from the blue channel. In particular, the mean intensity of the pixel values for the red channel had a significant role in all the subsets (Fig. 8). The general behavior of this image feature matched the brightness and temperature changes previously discussed (Fig. 5, Fig. 6 and Fig. 7).

3.3. Evaluation of predictive models for the estimation of $[O_2]_{fg}$

Predictive models were adjusted to estimate $[O_2]_{fg}$ based on the subsets of ten image features. Three different ML algorithms (LR, SVM, and MLP) were studied for each fuel blend. A nested CV was employed to train and validate the predictive models and tune hyperparameters, achieving significant accuracies (Table 3).

Predictive models reached validation accuracies around 0.995, which were lowered to 0.960 for the fuel blend of BFG70 and SEST conditions. Similar results were obtained for the three ML algorithms. However, SVM provided the highest accuracy in all the cases, outperforming ANN, as in [21] and [36]. The higher performance of a specific algorithm could be promoted by its particular characteristics. While LR fits a probability model based on logistic functions, SVM adjusts a hyperplane between classes, maximizing the margin between them. By contrast, MLP is a feed-forward artificial neural network, whose neurons are trained by back-propagation. However, the reduced difference in accuracy between the algorithms (below 1 %) limits the extrapolation of SVM as the best choice. Generalizability, and interpretability (black-box nature) are advanced research lines for ML techniques applied to combustion [37].

Fig. 9 shows the confusion matrixes of the predictive models based on that algorithm, for the validation subsets of all the experimental campaigns. According to the confusion matrixes, the predictive models achieved a balanced behavior, reaching high accuracies (0.9489 as a minimum) for all the $[O_2]_{fg}$ classes, fuel blends, and working conditions.

Table 3
Validation accuracies of the predictive models for estimating $[O_2]_{fg}$.

Campaign	EXP1	EXP2	EXP3	EXP4
Working condition	SEST	SEST	SEST	SETT
Fuel blend	BFG0	BFG70	BFG80	BFG70
LR (accuracy)	0.9920	0.9666	0.9970	0.9998
SVM (accuracy)	0.9936	0.9671	0.9980	0.9999
MLP (accuracy)	0.9866	0.9640	0.9962	0.9998

As a final evaluation, predictive models were adjusted employing the whole training set and the SVM algorithm. Hyperparameters were defined according to the best results of the nested CV, which were a linear kernel, a regularization term of 10 for the three experimental campaigns for SEST, and a regularization term of 0.1 for the tests of SETT. Finally, the accuracy of the models was measured for the test set. The training, validation, and test accuracy of the predictive models based on SVM are compared in Fig. 10.

The accuracy of the predictive models had a similar behavior for training, validation, and test sets without a significant influence of overfitting or underfitting. The predictive models achieved a high accuracy in estimating $[O_2]_{fg}$ based on flame images, although images may have slight variations that the human eye cannot perceive between different conditions. Furthermore, predictions were accurate even for low-visibility flames during regular or flameless combustion and transient conditions. Thus, automation methods can enhance the visual monitoring of the combustion supervised by humans.

4. Conclusions

In this study, the combustion monitoring in the steel sector was analyzed by acquiring color images from the flames of an experimental industrial furnace with a diffusion burner. Predictive models were adjusted to estimate the $[O_2]_{fg}$ based on intensity and textural characteristics extracted from the images. This monitoring was developed for tests with a fixed thermal power of 925 kW, two stability conditions (steady and transient temperature), and three fuel blends (BFG0, BFG70, and BFG80) obtained by mixing NG with BFG. Predictive models were fed by subsets of the computed image features, defined by ANOVA *F*-tests, and comprised the characteristics of a higher variance with $[O_2]_{fg}$.

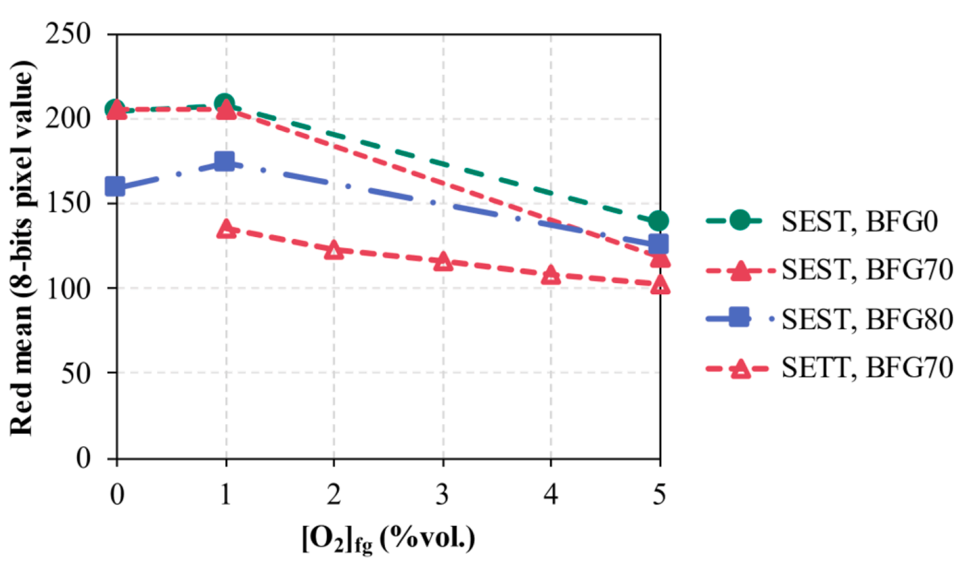

Fig. 8. Image feature of red mean versus $[O_2]_{fg}$. (For interpretation of the references to color in this figure legend, the reader is referred to the web version of this article.)

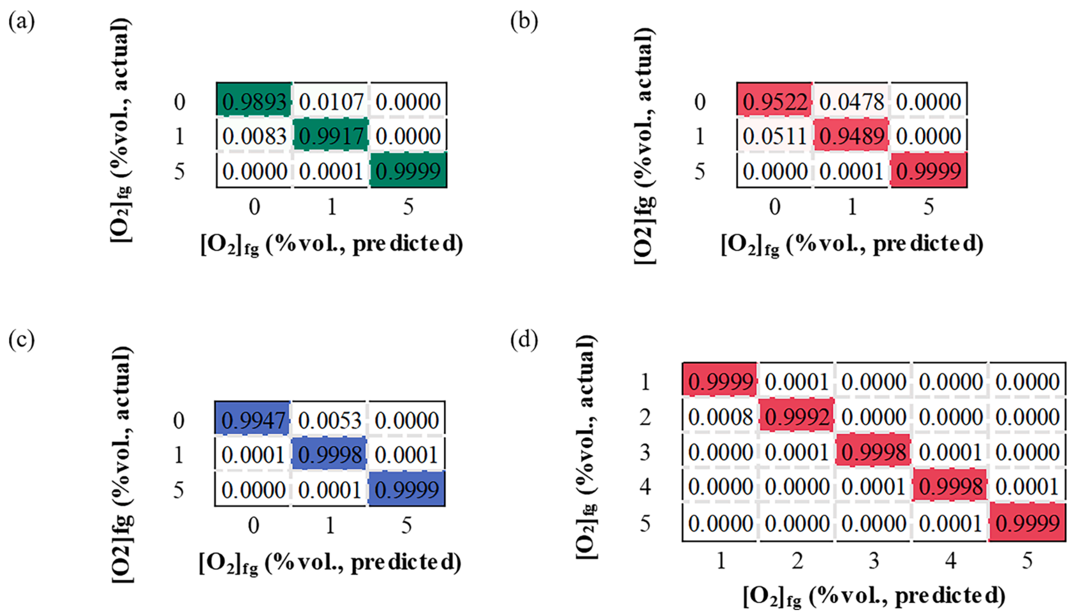

Fig. 9. Confusion matrixes of the predictive models based on SVM for the validation subsets of (a) SEST BFG0, (b) SEST BFG70, (c) SEST BFG80 and (d) SETT BFG70.

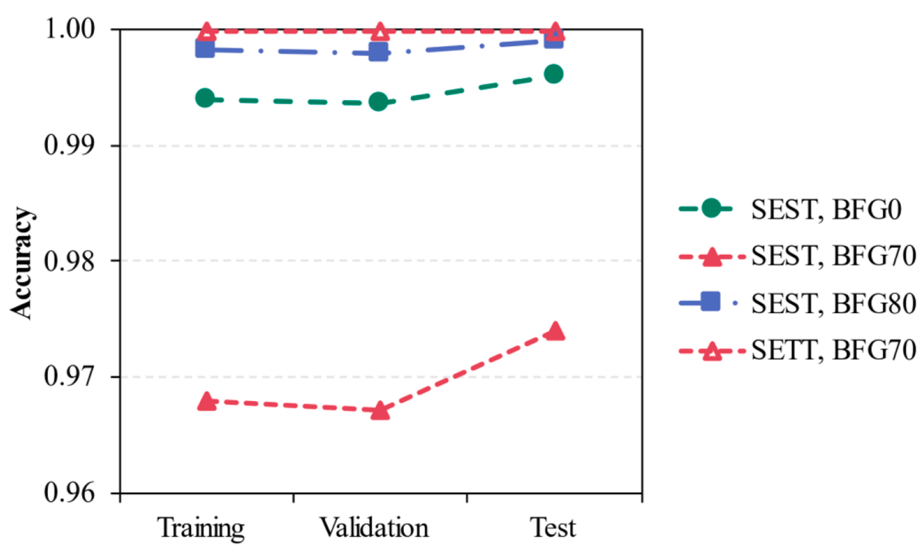

Fig. 10. Training, validation, and test accuracies of the predictive models based on SVM.

Three ML algorithms (LR, SVM, and ANN-MLP) were studied for the predictive models. The accuracy of the algorithms was evaluated by employing training-test split and nested CV.

The main conclusions of this research are as follows.

- Color images were affected by the combustion conditions analyzed. Image brightness increased for higher T_{cc}, related to lower BFG share in the fuel and $[O_2]_{fg}$ closer to 1 %vol. Moreover, adding BFG to NG reduced flame visibility.
- Intensity and textural characteristics from the three-color channels of the images were highlighted as descriptors of $[O_2]_{fg}$ without requiring the application of flame segmentation.
- Predictive models fed by the image characteristics reached high accuracies during training, validation, and testing, with adequate behavior without overfitting or underfitting and a minimum value of 0.96. The use of different ML algorithms (LR, SVM, or ANN) did not significantly affect the results, which were slightly better for SVM.
- Predictive models accurately estimated variations in $[O_2]_{fg}$ during regular and flameless combustion, even when images had minor variations between them. This way, the visual monitoring of combustion performed by humans can be improved.

The current research sets the stage for automated flame monitoring at an industrial scale. The detection of changes in the combustion conditions allows for the correction of deviated parameters, helping to optimize the processes and avoid the appearance of critical instabilities. The results obtained in this study demonstrate high precision for the case analyzed in an industrial test facility incorporating an industrial burner commonly used in steel manufacturing processes. This facility's process conditions and image quality were optimal for model training and development. However, using raw material inside the furnace instead of simulated load could affect the accuracy of the models. The irradiance from the steel load could interfere with the image or create fumes or particles inside the furnace, which may require additional preprocessing.

Further developments should focus on applying the models to industrial furnaces, such as reheating or annealing furnaces, where multiple burners can be captured in a single image. Overall air and fuel flow rates are typically measured in these furnaces, making it challenging to detect imbalances if there are several burners. Applying the models developed in this work to the different burners could provide a valuable monitoring tool, potentially reducing maintenance costs when residual streams are used as fuel. For this application, other challenging aspects of image processing are expected, like the separate segmentation of each burner or interferences of the combustion of the different burners in the same field of view. Nevertheless, industrial furnaces offer interesting possibilities for camera installation and image acquisition, as external viewing ports, which can reduce investment costs, or the installation in optimal locations to monitor the areas of interest.

CRediT authorship contribution statement

P. Compais: Writing – review & editing, Writing – original draft, Validation, Software, Methodology, Investigation, Data curation, Conceptualization. **J. Arroyo:** Writing – review & editing, Writing – original draft, Supervision, Resources, Project administration, Methodology, Investigation, Conceptualization. **F. Tovar:** Writing – review & editing, Investigation, Formal analysis, Data curation. **V. Cuervo-Piñera:** Writing – review & editing, Validation, Supervision, Methodology, Investigation, Conceptualization. **A. Gil:** Writing – review & editing, Writing – original draft, Supervision, Methodology.

Declaration of competing interest

The authors declare that they have no known competing financial interests or personal relationships that could have appeared to influence the work reported in this paper.

Data availability

The data that has been used is confidential.

Acknowledgments

This work has been supported by the European Union's Horizon 2020 Research and Innovation Programme under Grant Agreement No. 820771 (BAMBOO project).

Appendix A. Supplementary data

Supplementary data to this article can be found online at https://doi.org/10.1016/j.fuel.2023.130770.

References

[1] IEA. Iron and steel technology roadmap. https://www.iea.org/reports/iron-and-steel-technology-roadmap; 2020 [accessed 11 September 2023].
[2] Zheng W, Pang L, Liu Y, Xie F, Zeng W. Effects of initial condition and fuel composition on laminar burning velocities of blast furnace gas with low heat value. Fuel 2021;289:119775. https://doi.org/10.1016/j.fuel.2020.119775.
[3] Caillat S. Burners in the steel industry: Utilization of by-product combustion gases in reheating furnaces and annealing lines. Energy Procedia 2017;120:20–7. https://doi.org/10.1016/j.egypro.2017.07.152.
[4] Zhang L, Xie W, Ren Z. Combustion stability analysis for non-standard low-calorific gases: blast furnace gas and coke oven gas. Fuel 2020;278:118216. https://doi.org/10.1016/j.fuel.2020.118216.
[5] Nguyen PD, Ghazal G, Piñera VC, Battaglia V, Rensgard A, Ekman T, et al. Modelling of flameless oxy-fuel combustion with emphasis on radiative heat transfer for low calorific value blast furnace gas. Energy Procedia 2017;120:492–9. https://doi.org/10.1016/j.egypro.2017.07.177.
[6] Nguyen HT, Barnaud C, Domingo P, Nguyen PD, Vervisch L. Large-eddy simulation of flameless combustion with neural-network driven chemistry. Appl Energy Combust Sci 2023;14:100126. https://doi.org/10.1016/j.jaecs.2023.100126.
[7] Cuervo-Piñera V, Cifrián-Riesgo D, Nguyen PD, Battaglia V, Fantuzzi M, Della Rocca A, et al. Blast furnace gas based combustion systems in steel reheating furnaces. Energy Procedia 2017;120:357–64. https://doi.org/10.1016/j.egypro.2017.07.215.
[8] Arroyo J, Pérez L, Cuervo-Piñera V. CFD modeling and validation of blast furnace gas/natural gas mixture combustion in an experimental industrial furnace. Processes 2023;11(2):332. https://doi.org/10.3390/pr11020332.
[9] Bai X, Lu G, Hossain MM, Szuhánski J, Daood SS, Nimmo W, et al. Multi-mode combustion process monitoring on a pulverised fuel combustion test facility based on flame imaging and random weight network techniques. Fuel 2017;202:656–64. https://doi.org/10.1016/j.fuel.2017.03.091.
[10] Abdurakipov SS, Gobyzov OA, Tokarev MP, Dulin VM. Combustion regime monitoring by flame imaging and machine learning. Optoelectron Instrum Data Process 2018;54:513–9. https://doi.org/10.3103/S875669901805014X.
[11] Han Z, Li J, Zhang B, Hossain MM, Xu C. Prediction of combustion state through a semi-supervised learning model and flame imaging. Fuel 2021;289:119745. https://doi.org/10.1016/j.fuel.2020.119745.
[12] Yang G, He Y, Li X, Liu H, Lan T. Gabor-GLCM-based texture feature extraction using flame image to predict the O_2 content and NO_x. ACS Omega 2022;7:3889–99. https://doi.org/10.1021/acsomega.1c03397.
[13] Smith ML, Smith LN, Hansen MF. The quiet revolution in machine vision - a state-of-the-art survey paper, including historical review, perspectives, and future directions. Comput Ind 2021;130:103472. https://doi.org/10.1016/j.compind.2021.103472.
[14] Liu J, Ulishney C, Dumitrescu CE. Random forest machine learning model for predicting combustion feedback information of a natural gas spark ignition engine. J Energy Resour Technol 2021;143(1):012301. https://doi.org/10.1115/1.4047761.
[15] Liu J, Ulishney C, Dumitrescu CE. Machine learning assisted prediction of exhaust gas temperature of a heavy-duty natural gas spark ignition engine. Appl Energy 2021;300:117413. https://doi.org/10.1016/j.apenergy.2021.117413.
[16] Huang Q, Liu J, Ulishney C, Dumitrescu CE. On the use of artificial neural networks to model the performance and emissions of a heavy-duty natural gas spark ignition engine. Int J Engine Res 2022;23(11):1879–98. https://doi.org/10.1177/14680874211034409.
[17] Liu J, Huang Q, Ulishney C, Dumitrescu CE. Comparison of random forest and neural network in modeling the performance and emissions of a natural gas spark ignition engine. J Energy Resour Technol 2022;144(3):032310. https://doi.org/10.1115/1.4053301.
[18] Liu J, et al. A support-vector machine model to predict the dynamic performance of a heavy-duty natural gas spark ignition engine. SAE Technical Paper 2021;2021-01-0529. https://doi.org/10.4271/2021-01-0529.
[19] Compais P, Arroyo J, González-Espinosa A, Gonzalo-Tirado C, Castán-Lascorz, MA, Barrio J et al. Experimental analysis of blast furnace gas co-firing in a semi-industrial furnace using colour images. Proceedings of the 7th World Congress on Momentum, Heat and Mass Transfer 2022;117. https://doi.org/10.11159/csp22.117.
[20] Compais P, Arroyo J, González-Espinosa A, Castán-Lascorz MÁ, Gil A. Optical analysis of blast furnace gas combustion in a laboratory premixed burner. ACS Omega 2022;7:24498–510. https://doi.org/10.1021/acsomega.2c02103.
[21] Compais P, Arroyo J, Castán-Lascorz MÁ, Barrio J, Gil A. Detection of slight variations in combustion conditions with machine learning and computer vision. Eng Appl Artif Intell 2023;126(Pt A):106772. https://doi.org/10.1016/j.engappai.2023.106772.
[22] Uribe-Soto W, Portha JF, Commenge JM, Falk L. A review of thermochemical processes and technologies to use steelworks off-gases. Renew Sustain Energy Rev 2017;74:809–23. https://doi.org/10.1016/j.rser.2017.03.008.
[23] European Commission, Directorate-General for Research and Innovation, Battaglia V, Niska J, Cuervo Piñera V, Fantuzzi M. High efficiency low NOX BFG based combustion systems in steel reheating furnaces (HELNOx-BFG): final report. Publications Office 2018. https://doi.org/10.2777/165777.
[24] Khidr KI, Eldrainy YA, EL-Kassaby MM. Towards lower gas turbine emissions: Flameless distributed combustion. Renew Sust Energ Rev 2017;67:1237–66. https://doi.org/10.1016/j.rser.2016.09.032.
[25] Reddy VM, Sawant D, Trivedi D, Kumar S. Studies on a liquid fuel based two stage flameless combustor. Proc Combust Inst 2013;34(2):3319–26. https://doi.org/10.1016/j.proci.2012.06.028.
[26] Yetter RA, Glassman I, Gabler HC. Asymmetric whirl combustion: a new low NOx approach. Proc Combust Inst 2000;28(1):1265–72. https://doi.org/10.1016/s0082-0784(00)80339-2.
[27] Mathew AP, Asokan A, Batri K, Sivakumar D. Comparative analysis of flame image features for combustion analysis. Indian J Sci Technol 2016;9:1–11. https://doi.org/10.17485/ijst/2016/v9i6/79904.
[28] Katzer C, Babul K, Klatt M, Krautz HJ. Quantitative and qualitative relationship between swirl burner operating conditions and pulverized coal flame length. Fuel Process Technol 2017;156:138–55. https://doi.org/10.1016/j.fuproc.2016.10.013.
[29] González-Cencerrado A, Peña B, Gil A. Experimental analysis of biomass co-firing flames in a pulverized fuel swirl burner using a CCD based visualization system. Fuel Process Technol 2015;130:299–310. https://doi.org/10.1016/j.fuproc.2014.10.041.
[30] Haralick RM, Shanmugam K, Dinstein I. Textural features for image classification. IEEE Trans Syst Man Cybern 1973;SMC-3:610–21. https://doi.org/10.1109/TSMC.1973.4309314.
[31] Huang HW, Zhang Y. Flame colour characterization in the visible and infrared spectrum using a digital camera and image processing. Meas Sci Technol 2008;19:085406. https://doi.org/10.1088/0957-0233/19/8/085406.

[32] He L, Guo Q, Gong Y, Wang F, Yu G. Investigation of OH* chemiluminescence and heat release in laminar methane–oxygen co-flow diffusion flames. Combust Flame 2019;201:12–22. https://doi.org/10.1016/j.combustflame.2018.12.009.

[33] Karnani S, Dunn-Rankin D. Visualizing CH* chemiluminescence in sooting flames. Combust Flame 2013;160:2275–8. https://doi.org/10.1016/j.combustflame.2013.05.002.

[34] Li T, Zhang C, Liu D. Simultaneously retrieving of soot temperature and volume fraction in participating media and laminar diffusion flame using multi-spectral light field imaging. Int J Therm Sci 2023;193:108472. https://doi.org/10.1016/j.ijthermalsci.2023.108472.

[35] Huang HW, Zhang Y. Digital colour image processing based measurement of premixed CH4+air and C2H4+air flame chemiluminescence. Fuel 2011;90:48–53. https://doi.org/10.1016/j.fuel.2010.07.050.

[36] Han Z, Hossain MM, Wang Y, Li J, Xu C. Combustion stability monitoring through flame imaging and stacked sparse autoencoder based deep neural network. Appl Energy 2020;259:114159. https://doi.org/10.1016/j.apenergy.2019.114159.

[37] Zhou L, Song Y, Ji W, Wei H. Machine learning for combustion. Energy AI 2022;7:1011128. https://doi.org/10.1016/j.egyai.2021.100128.

3. Aportaciones y conclusiones

3.1. Aportaciones del doctorando

El trabajo realizado en esta tesis doctoral busca contribuir al desarrollo de sistemas de visión para la monitorización de la combustión del gas de alto horno, con el objetivo final de incrementar su eficiencia en operación, promoviendo su valorización e incrementando la sostenibilidad en los procesos productivos del acero. Para ello se ha realizado un extenso análisis experimental del efecto de la composición del combustible y la relación aire-combustible sobre imágenes de color, a escala de laboratorio y semiindustrial con quemadores de 20 kW_t y 1.2 MW_t, respectivamente. Este estudio ha demostrado la viabilidad del procesamiento de imágenes de llama para el control de la combustión del gas de alto horno, cuya mayor inestabilidad requiere de una detección temprana de pequeñas variaciones.

Las principales aportaciones del trabajo de investigación están alineadas con los objetivos la tesis, y se describen a continuación.

- Análisis del estado del arte. Para la elaboración de la tesis se ha realizado un estudio detallado sobre la caracterización óptica de la combustión. Se ha investigado la caracterización de la radiación de llamas de premezcla y difusión a partir de sus espectros e imágenes, así como el procesamiento de dichas imágenes para la extracción de descriptores de la combustión y su modelado con técnicas de aprendizaje automático. Este estudio ha servido de base para el resto de la investigación, y proporciona un marco de referencia para futuros trabajos de la monitorización de la combustión a partir de técnicas de imagen.

- Estudio de las imágenes de llama con distintos combustibles. El trabajo de investigación ha analizado el efecto la mezcla de combustible y la relación aire-combustible sobre las imágenes de llama, capturadas en distintos escenarios. Se han estudiado imágenes obtenidas en escala de laboratorio y semiindustrial, con quemadores de premezcla y difusión, en condiciones estacionarias y transitorias, y con sistemas de visión desplegados dentro y fuera del horno. Aparte del análisis cualitativo de las imágenes, se han calculado 66 variables numéricas, cuya relación individual con el exceso de aire ha sido también cuantificada.

- Predicción de las condiciones de combustión a partir de las imágenes de llama. Las características de imagen extraídas se han utilizado para modelar el exceso de aire en la combustión con técnicas de aprendizaje automático, optimizando y evaluando distintos modelos mediante una estructura de validación cruzada anidada, y estudiando su rendimiento con distintos excesos de aire, algoritmos de aprendizaje y grupos de muestras. En general, los modelos han detectado correctamente el exceso de aire en más del 95 % de las ocasiones, reduciéndose a un 79 % en el peor escenario, permitiendo monitorizar variaciones más pequeñas que en trabajos previos, imperceptibles para el ojo humano.

La investigación ha tenido como resultado la generación de artículos en tres revistas indexadas y un congreso, incluidos en la siguiente numeración.

I. Optical analysis of blast furnace gas combustion in a laboratory premixed burner. **P. Compais**, J. Arroyo, A. González-Espinosa, M. A. Castán-Lascorz, A. Gil. ACS Omega (2022); Vol. 7, pp. 24498-24510.

II. Detection of slight variations in combustion conditions with machine learning and computer vision. **P. Compais**, J. Arroyo, M. A. Castán-Lascorz, J. Barrio, A. Gil. Engineering Applications of Artificial Intelligence (2023); Vol. 126, 106772.

III. Flame monitoring system based on images for steel reheating furnaces: a case study of validation from laboratory to semi-industrial scales. **P. Compais**, J. Arroyo, V. Cuervo-Piñera, A. Gil. *Proceedings of the 18th Conference on Sustainable Development of Energy, Water and Environment Systems* (2023), Dubrovnik (Croatia).

IV. Promoting the valorization of blast furnace gas in the steel industry with the visual monitoring of combustion and artificial intelligence. **P. Compais**, J. Arroyo, F. Tovar, V. Cuervo-Piñera, A. Gil. Fuel (2024); Vol. 362, 130770.

Aparte de los artículos que constituyen la tesis, se ha participado en un congreso adicional, cuya referencia se incluye a continuación.

A. Experimental analysis of blast furnace gas co-firing in a semi-industrial furnace using colour images. P. Compais, J. Arroyo, A. González-Espinosa, C. Gonzalo-Tirado, M. A. Castán-Lascorz, J. Barrio, V. Cuervo-Piñera. *Proceedings of the 7th World Congress on Momentum, Heat and Mass Transfer* (2022), Virtual Conference.

3.2. Conclusiones finales y trabajo futuro

Esta tesis confirma la viabilidad técnica de la monitorización visual de la combustión de gas de alto horno con imágenes de color. Las llamas se han caracterizado según la intensidad de la radiación, la textura espacial capturada en la imagen, y la geometría de las llamas. A partir de estas propiedades visuales se ha conseguido modelar la relación aire-combustible en distintos escenarios de operación, obteniéndose una elevada precisión en todos ellos.

Este estudio incluye como novedad la adaptación de la monitorización visual de la combustión al caso particular del gas de alto horno. Para ello, se ha definido un procedimiento a medida que integra características de imagen utilizadas en múltiples trabajos previos, seleccionadas automáticamente según un criterio cuantitativo. A continuación, se resumen las conclusiones obtenidas en este trabajo.

- Los procesos industriales limitan el tiempo de adaptación y ajuste de los quemadores para distintas mezclas de combustible, por lo que se utilizan configuraciones de quemador robustas que permiten la combustión en varias condiciones de operación, aunque no alcancen el óptimo de eficiencia para cada una de ellas. Este estudio ha replicado esta metodología a escala de laboratorio mediante el uso de un mismo quemador para mezclas de combustible con diferencias significativas en su poder calorífico. A pesar de esta limitación, se ha conseguido la combustión de cada mezcla, aunque en condiciones ineficientes y con diferentes excesos de aire, obteniéndose combustión incompleta en parte del rango de operación.

- La combustión de gas de alto horno con un quemador de premezcla se ha estudiado a escala de laboratorio con un espectrómetro, una cámara ultravioleta-visible y otra de color. La viabilidad de cada una de estas tecnologías se ha confirmado para la caracterización de la radiación de la llama, definida por la emisión continua del radical CO_2, y afectada por la composición de la mezcla de combustible y el exceso de aire. Las imágenes de color se han procesado para identificar automáticamente los píxeles de llama y extraer características de intensidad, geometría y textura, con las que se ha conseguido modelar el exceso de aire con una elevada precisión.

- A escala semiindustrial se han utilizado cámaras de color para analizar la combustión con quemadores de difusión. Se han detectado diferencias significativas entre las imágenes de laboratorio y semiindustriales, caracterizadas por una mayor iluminación de las paredes del horno y una llama más difusa. En este caso, la identificación de píxeles como llama o fondo ha tenido una mayor incertidumbre, por lo que, en lugar de utilizar la segmentación de laboratorio, las características de intensidad y textura se han extraído de todos los píxeles de la imagen. A pesar de las diferencias visuales, la viabilidad de las cámaras de color se ha confirmado de nuevo, permitiendo medir el efecto de la composición del combustible y la concentración de oxígeno en los gases de combustión en las imágenes, al igual que en laboratorio. Además, esta última variable se ha modelado manteniendo el alto rendimiento conseguido en las pruebas de laboratorio para el exceso de aire. Por último, el procesamiento de imágenes y modelado se ha implementado en un programa informático para su uso en tiempo real a escala semiindustrial.

- A modo de resumen, se ha validado un sistema de monitorización de la combustión de gas de alto horno con técnicas de visualización de imagen en color e inteligencia artificial. Dicho sistema utiliza características visuales de intensidad y textura, así como modelos ajustados con técnicas de aprendizaje automático, evaluados en distintos escenarios y alcanzando un elevado rendimiento en la predicción de la relación aire-combustible asociada a las imágenes de llama.

A partir de esta tesis doctoral, se plantean dos líneas principales de trabajo futuro, descritas en los párrafos siguientes.

- La madurez tecnológica del desarrollo se ha incrementado con los ensayos en escala semiindustrial, que, no obstante, presentan diferencias respecto a los procesos industriales. Por ello, resulta crucial estudiar en detalle estas variaciones para completar el desarrollo del sistema de monitorización visual, y así conseguir su implementación industrial. En primer lugar, en esta tesis se ha utilizado un circuito de agua para simular la transferencia de calor a una carga dentro del horno, en vez de introducir láminas de acero para su tratamiento térmico. En este proceso, el material emite radiación que podría afectar a la imagen, y, además, se podrían generar vapores o partículas adicionales cuyas emisiones no se han analizado en este trabajo. En segundo lugar, para reducir los costes de operación y mantenimiento respecto a otros sensores convencionales, los sistemas de monitorización visual deben supervisar individualmente varios quemadores capturados en la misma imagen. Para lograr este objetivo, la segmentación de los píxeles de llama no es suficiente, ya que esta técnica sólo clasificaría cada píxel como llama o fondo, y se necesitaría la identificación adicional de quemador correspondiente a cada píxel. Esta tarea tiene una alta complejidad, ya que las llamas de distintos quemadores se pueden ocultar entre sí, dependiendo de la posición de la cámara, o irradiar luz sobre áreas del horno asociadas a otro quemador, por lo que la intensidad medida para un píxel podría depender de varios quemadores. Por ello, es de vital importancia estudiar el rendimiento de distintas alternativas para la segmentación de llamas de distintos quemadores.

- Aparte del propio desarrollo del sistema de monitorización visual, también es indispensable el estudio de su integración en los sistemas de control de la industria, con el objetivo de habilitar su uso y aprovechar al máximo sus ventajas. Normalmente, las cámaras se utilizan a escala industrial para facilitar la inspección del interior de hornos por parte de un operario, así como para ayudar en la toma de decisiones y el ajuste de la operación. Algunos sistemas de visión, como el desarrollado en la tesis, transforman la información de las imágenes en variables asociadas al proceso de combustión, lo que facilita su integración en sistemas automatizados de control. Para lograr esta implementación, se requiere analizar el comportamiento dinámico de la combustión del gas de alto horno y el tiempo de procesamiento del sistema de monitorización visual, además de la optimización del código y la realización de pruebas con hardware de distintas prestaciones.

En estos momentos, se ha comenzado el desarrollo de ambas líneas de trabajo futuro, buscando la transferencia industrial del sistema de monitorización, así como su integración con controladores automáticos. De esta manera, se continúa incrementando la madurez tecnológica del sistema para su despliegue final en la industria, cuyo objetivo es la caracterización rápida y precisa de la combustión para reducir el tiempo de operación en condiciones ineficientes. Este trabajo se ha centrado en el estudio de la combustión del gas de alto horno para promover su valorización, una alternativa que incrementa la sostenibilidad de la producción de acero reduciendo la energía consumida y las emisiones de CO_2 equivalentes, además de proporcionar un ahorro económico. Por ello, este estudio es de crucial importancia tanto para la planta de ArcelorMittal Asturias, como para la ruta alto horno-horno de oxígeno básico de la producción de acero.

El desarrollo del sistema de monitorización ha afrontado y resuelto el desafío de detectar pequeñas variaciones visuales en las llamas de gas de alto horno, imperceptibles para el ojo humano, mediante el uso de unas técnicas de visión artificial. Este trabajo pone de relieve que los sistemas de visión artificial pueden superar las capacidades humanas incluso en el rango visible, por lo que su uso puede habilitar la realización de tareas inviables para las personas, como la supervisión de condiciones tradicionalmente conocidos como *sin llama.* Actualmente, la monitorización de estos escenarios tiene una alta relevancia debido a su relación con la combustión del hidrógeno y su uso como vector energético. En este estudio también se ha conseguido incrementar la precisión de la monitorización visual de la combustión respecto a la de estudios previos, configurando un nuevo estado del arte con un alto potencial de aplicación en diferentes procesos industriales.

4. Factor de impacto, área temática y justificación de la contribución de las publicaciones

I. Optical analysis of blast furnace gas combustion in a laboratory premixed burner. P. Compais, J. Arroyo, A. González-Espinosa, M. A. Castán-Lascorz, A. Gil. ACS Omega (2022); Vol. 7, pp. 24498-24510.

   a. Factor de impacto 2023: **3.7**

   b. Factor de impacto de los últimos 5 años: **4.0**

   c. Área temática: **química, multidisciplinar**

   d. Justificación de la contribución: **conceptualización, metodología, software, validación, análisis formal, investigación, conservación de datos, escritura – borrador original, escritura – revisión y edición, visualización**

II. Detection of slight variations in combustion conditions with machine learning and computer vision. P. Compais, J. Arroyo, M. A. Castán-Lascorz, J. Barrio, A. Gil. Engineering Applications of Artificial Intelligence (2023); Vol. 126, 106772.

   a. Factor de impacto 2023: **7.5**

   b. Factor de impacto de los últimos 5 años: **7.4**

   c. Área temática: **automática y sistemas de control, ciencias de la informática, inteligencia artificial, ingeniería eléctrica, electrónica y multidisciplinar**

   d. Justificación de la contribución: **conceptualización, metodología, software, validación, análisis formal, investigación, conservación de datos, escritura – borrador original, escritura – revisión y edición, visualización**

III. Flame monitoring system based on images for steel reheating furnaces: a case study of validation from laboratory to semi-industrial scales. P. Compais, J. Arroyo, V. Cuervo-Piñera, A. Gil. *Proceedings of the 18th Conference on Sustainable Development of Energy, Water and Environment Systems* (2023), Dubrovnik (Croatia).

   a. Área temática: **desarrollo sostenible**

   b. Justificación de la contribución: **conceptualización, metodología, software, validación, análisis formal, investigación, conservación de datos, escritura – borrador original, escritura – revisión y edición, visualización**

IV. Promoting the valorization of blast furnace gas in the steel industry with the visual monitoring of combustion and artificial intelligence. P. Compais, J. Arroyo, F. Tovar, V. Cuervo-Piñera, A. Gil. Fuel (2024); Vol. 362, 130770.

   a. Factor de impacto 2023: **6.7**

   b. Factor de impacto de los últimos 5 años: **6.5**

c. Área temática: **energía y combustibles, ingeniería química**

d. Justificación de la contribución: **conceptualización, metodología, software, validación, análisis formal, investigación, conservación de datos, escritura – borrador original, escritura – revisión y edición, visualización**

5. Bibliografía

[1] IEA. Iron and steel technology roadmap. Octubre 2020. https://www.iea.org/reports/iron-and-steel-technology-roadmap.

[2] F. Rossi, C. Zuffi, M. L. Parisi, D. Fiaschi and G. Manfrida. Comparative scenario-based LCA of renewable energy technologies focused on the end-of-life evaluation. *J. Clean. Prod.*, 405:136931, 2023.

[3] E. Pierri, D. Hellkamp, S. Thiede and C. Herrmann. Enhancing energy flexibility through the integration of variable renewable energy in the process industry. *Proc. CIRP*, 98:7-12, 2021.

[4] P. Larrinaga, A. Campos-Celador, J. Legarreta and G. Diarce. Evaluation of the theoretical, technical and economic potential of industrial waste heat recovery in the basque country. *J. Clean. Prod.*, 312:127494, 2021.

[5] EUROFER. Overview of the steel production process. Diciembre 2023. https://www.eurofer.eu/about-steel/learn-about-steel/what-is-steel-and-how-is-steel-made.

[6] S. Caillat. Burners in the steel industry: Utilization of by-product combustion gases in reheating furnaces and annealing lines. *Energy Procedia*, 120:20–7, 2017.

[7] F. Meng, G. Rong, R. Zhao, B. Chen, X. Xu, H. Qiu, X. Cao and L. Zhao. Incorporating biochar into fuels system of iron and steel industry: carbon emission reduction potential and economic analysis. *Appl. Energy*, 356:122377, 2024.

[8] A. Boretti. The perspective of hydrogen direct reduction of iron. *J. Clean. Prod.*, 429:139585, 2023.

[9] X. Wang., C. Li, C. H. Lam, K. Subramanian, Z. H. Qin, J. H. Mou, M. Jin, S. S. Chopra, V. Singh, Y. S. Ok, J. Yan, H. Y. Li and C. S. K. Lin. Emerging waste valorisation techniques to moderate the hazardous impacts, and their path towards sustainability. *J. Hazar. Mater.*, 423:127023, 2022.

[10] W. Uribe-Soto, J. F. Portha, J. M. Commenge and L. Falk. A review of thermochemical processes and technologies to use steelworks off-gases. *Renew. Sustain. Energy Rev.*, 74:809-23, 2017.

[11] BAMBOO. Grant Agreement. Agosto 2018.

[12] ARCELORMITTAL. Qué hacemos | ArcelorMittal España. Junio 2024. https://spain.arcelormittal.com/que-hacemos/.

[13] V. Cuervo-Piñera, D. Cifrián-Riesgo, P. D. Nguyen, V. Battaglia, M. Fantuzzi, A. Della Rocca, M. Ajeno, A. Rensgard, C. Wang, J. Niska, T. Ekman, C. Rein, and W. Adler. Blast furnace gas based combustion systems in steel reheating furnaces. *Energy Procedia*, 120:357–64, 2017.

[14] W. Zheng, L. Pang, Y. Liu, F. Xie, and W. Zeng. Effects of initial condition and fuel composition on laminar burning velocities of blast furnace gas with low heat value. *Fuel*, 289:119775, 2021.

[15] L. Zhang, W. Xie, and Z. Ren. Combustion stability analysis for non-standard low-calorific gases: blast furnace gas and coke oven gas. *Fuel*, 278:118216, 2020.

[16] METECH STG. Reheating furnaces. Enero 2024. http://www.stggroup.it/en/plants/reheating_furnace.

[17] M. L. Smith, L. N. Smith, and M. F. Hansen. The quiet revolution in machine vision - a state-of-the-art survey paper, including historical review, perspectives, and future directions. *Comput. Ind.*, 130:103472, 2021.

[18] L. He, Q. Guo, Y. Gong, F. Wang, and G. Yu. Investigation of OH* chemiluminescence and heat release in laminar methane–oxygen co-flow diffusion flames. *Combust. Flame*, 201:12-22, 2019.

[19] H. W. Huang, and Y. Zhang. Digital colour image processing based measurement of premixed CH4 + air and C2H4 + air flame chemiluminescence. *Fuel,* 90(1):48– 53, 2011.

[20] M. M. Tripathi, S. R. Krishnan, K. K. Srinivasan, F. Y. Yueh, and J. P. Singh. Chemiluminescence-based multivariate sensing of local equivalence ratios in premixed atmospheric methane-air flames. *Fuel,* 93:684– 691, 2012.

[21] H. Soltanian, M. Z. Targhi, and H. Pasdarshahri. Chemiluminescence usage in finding optimum operating range of multi-hole burners. *Energy*, 180:398–404, 2019.

[22] F. M. Quintino, T. P. Trindade, and E. C. Fernandes. Biogas combustion: chemiluminescence fingerprint. *Fuel,* 31:328–340, 2018.

[23] C. T. Chong, and S. Hochgreb. Flame structure, spectroscopy and emissions quantification of rapeseed biodiesel under model gas turbine conditions*. Appl. Energy,* 185:1383–139, 2017.

[24] L. Merotto, M. Sirignano, M. Commodo, A. D'Anna, R. Dondè, and S. de Iuliis. Experimental characterization and modeling for equivalence ratio sensing in non-premixed flames using chemiluminescence and laser-induced breakdown spectroscopy techniques. *Energy Fuels*, 31(3):3227–3233, 2017.

[25] D. Giassi, S. Cao, B. A. v. Bennett, D. P. Stocker, F. Takahashi, M. D. Smooke, and M. B. Long. Analysis of CH* concentration and flame heat release rate in laminar coflow diffusion flames under microgravity and normal gravity. *Combust. Flame,* 167:198–206, 2016.

[26] H. W. Huang, and Y. Zhang. Imaging based chemiluminescence characterisation of partially premixed syngas flames through DFCD technique. *Int. J. Hydrogen Energy,* 38(11):4839–4847, 2013.

[27] T. Parameswaran, P. Gogolek and P. Hughes. Estimation of combustion air requirement and heating value of fuel gas mixtures from flame spectra. *Appl. Therm. Eng.*, 105:353–361, 2016.

[28] T. F. Guiberti, D. Durox, and T. Schuller. Flame chemiluminescence from CO2- and N2-diluted laminar CH4/air premixed flames. *Combust. Flame,* 181:110–122, 2017.

[29] K. Deng, Y. Zhong, M. Wang, Y. Zhong and K. H. Luo. Effects of acoustic excitation on the combustion instability of hydrogen-methane lean premixed swirling flames. *ACS Omega*, 5:8744– 8753, 2020.

[30] M. Huang, Y. Xiao, Z. Zhang, W. Shao, Y. Xiong, Y. Liu, Z. Liu and F. Lei. Effect of air/fuel nozzle arrangement on the MILD combustion of syngas. *Appl. Therm. Eng.*, 87:200– 208, 2015.

[31] Y. Liu, J. Tan, M. Wan, L. Zhang, and X. Yao. Quantitative measurement of OH* and CH* chemiluminescence in jet diffusion flames. *ACS Omega*, 5:15922– 15930, 2020.

[32] J. Wang, M. Chang, M. Zhang, G. Li, S. Chen and Z. Huang. Flame front identification and its effect on turbulent premixed flames topology at high pressures. *Exp. Therm. Fluid. Sci.*, 107:107-117, 2019.

[33] R. Wu, F. Xie, J. Wei, X. Song, H. Yang, P. Lv and G. Yu. Study on soot emission characteristics of methane/oxygen inverse diffusion flame. *ACS Omega*, 6:23191– 23202, 2021.

[34] MESUREX. SondaTEC. Diciembre 2023. https://mesurex.com/catalogo/productos/camaras-alta-temperatura/sondatec/.

[35] VISIONTIR. Continuous monitoring of furnace temperature in glass manufacturing. Mayo 2023. https://visiontir.com/continuous-monitoring-of-furnace-temperature-in-glass-manufacturing/.

[36] THERMOTEKNIX. ThermaScope HDC Colour Camera – Thermoteknix. Mayo 2023. https://www.thermoteknix.com/products/industrial/thermascope-hdc.

[37] C. Katzer, K. Babul, M. Klatt and H. J. Krautz. Quantitative and qualitative relationship between swirl burner operating conditions and pulverized coal flame length. *Fuel Process. Technol.*, 156:138– 155, 2017.

[38] D. Sun, G. Lu, H. Zhou, Y. Yan and S. Liu. Quantitative assessment of flame stability through image processing and spectral analysis. *IEEE Trans. Instrum. Meas.*, 64(12):3323– 3333, 2015.

[39] A. González-Cencerrado, B. Peña and A. Gil. Coal flame characterization by means of digital image processing in a semi-industrial scale PF swirl burner. *Appl. Energy,* 94:375–384, 2012.

[40] X. Bai, G. Lu, M. M. Hossain, J. Szuhánszki, S. S. Daood, W. Nimmo, Y. Yan amd M. Pourkashanian. Multi-mode combustion process monitoring on a pulverised fuel combustion test facility based on flame imaging and random weight network techniques. *Fuel*, 202:656– 664, 2017.

[41] A. P. Mathew, A. Asokan, K. Batri and D. Sivakumar. Comparative analysis of flame image features for combustion analysis. *Indian J. Sci. Technol.*, 9:1–11, 2016.

[42] G. Yang, Y. He, X. Li, H. Liu and T. Lan. Gabor-GLCM-based texture feature extraction using flame image to predict the O2 content and NOx. *ACS Omega*, 7:3889–99, 2022.

[43] A. González-Espinosa, A. Gil, L. Royo-Pascual, A. Nueno and C. Herce. Effects of hydrogen and primary air in a commercial partially-premixed atmospheric gas

burner by means of optical and supervised machine learning techniques. *Int. J. Hydrogen Energy*, 45(55):31130-50, 2020.

[44] A. González-Cencerrado, B. Peña and A. Gil. Coal flame characterization by means of digital image processing in a semi-industrial scale PF swirl burner. *Appl. Energy*, 94:375-84, 2012.

[45] A. González-Cencerrado, A. Gil and B. Peña. Characterization of PF flames under different swirl conditions based on visualization systems. *Fuel*, 113:798-809, 2013.

[46] A. González-Cencerrado, B. Peña and A. Gil. Experimental analysis of biomass co-firing flames in a pulverized fuel swirl burner using a CCD based visualization system. *Fuel Process. Technol.*, 130:299-310, 2015.

[47] J. Zhu, Z. Wang, R. Li, S. Liu and Y. Hua. Experimental study and prediction model of combustion stability and combustion mode variation of burning methanol/biodiesel blends for diesel engines. *Fuel*, 335:127038, 2023.

[48] D. Sun, G. Lu, H. Zhou, X. Li and Y. Yan. A simple index based quantitative assessment of flame stability. *2013 IEEE Int. Conf. Imaging Syst. Technol. Proc. (IST)*, 190-193, 2013.

[49] Y. Liu, Q. Xue, H. Zuo, F. Yang, X. Peng and J. Wang. Effects of CO2 and N2 dilution on the combustion characteristics of H2/CO mixture in a turbulent, partially premixed burner. *ACS Omega*, 6:15651-62, 2021.

[50] P. Brynolfsson, D. Nilsson, T. Torheim, T. Asklund, C. T. Karlsson, J. Trygg, T. Nyholm and A. Garpebring. Haralick textura features from apparent diffusion coeficiente (ADC) MRI images depend on imaging and pre-processing parameters. *Sci. Rep.*, 7(1):4041, 2017.

[51] C. Luo, Z. Yu, Y. Wang and Y. Ai. Experimental investigation of lean methane-air laminar premixed flames at engine-relevant temperatures. *ACS Omega*, 6:17977-87, 2021.

[52] A. C. Vargas, A. M. García, C. E. Arrieta, J. S. Del Rio and A. Amell. A burning velocity of turbulent methane/air premixed flames in subatmospheric environment. *ACS Omega*, 5:25095-103, 2020.

[53] Z. Han, J. Li, B. Zhang, M. M. Hossain and C. Xu 2021. Prediction of combustion state through a semi-supervised learning model and flame imaging. *Fuel,* 289:119745, 2021.

[54] S. S. Abdurakipov, O. A. Gobyzov, M. P. Tokarev, V. M. Dulin. Combustion regime monitoring by flame imaging and machine learning. *Optoelectron. Instrument. Data Process*, 54:513–519, 2018.

[55] Y. Cheng, Y. Huang, B. Pang and W. Zhang. ThermalNet: A deep reinforcement learning-based combustion optimization system for coal-fired boiler. *Eng. Appl. Artif. Intell.*, 74:303-11, 2018.

[56] M. Y. Jung, J. H. Chang, M. Oh and C. Lee. Dynamic model and deep neural network-based surrogate model to predict dynamic behaviors and steady-state performance of solid propellant combustion. *Combust. Flame*, 250:112649, 2023.

[57] M. Park, J. Hur and W. Lee. Prediction of oil-fired boiler emissions with ensemble methods considering variable combustion air conditions. *J. Clean. Prod.*, 275:134094, 2022.

[58] P. H. Ibargüengoytia, M. A. Delgadillo, U. A. García and A. Reyes. Viscosity virtual sensor to control combustion in fossil fuel power plants. *Eng. Appl. Artif. Intell.*, 23:2153-63, 2013.

[59] D. Quesada, G. Valverde, P. Larrañaga and C. Bielza. Long-term forecasting of multivariate time series in industrial furnaces with dynamic Gaussian Bayesian networks. *Eng. Appl. Artif. Intell.*, 103:104301, 2021.

[60] M. O. Lawal. Tomato detection based on modified YOLOv3 framework. *Sci. Rep.*, 11:1447, 2021.

[61] F. Matkvoic, M. Ivasic-Kos and S. Ribaric. A new approach to dominant motion pattern recognition at the macroscopic crowd level. *Eng. Appl. Artif. Intell.*, 116:105387, 2022.

[62] M. Mowbray, T. Savage, C. Wu, Z. Song, B. A. Cho, E. A. Del Rio-Chanona and D. Zhang. Machine learning for biochemical engineering: A review. *Biochem. Eng. J.*, 172:108054, 2021.

[63] A. M. Roy. Adaptive transfer learning-based multiscale feature fused deep convolutional neural network for EEG MI multiclassification in brain-computer interface. *Eng. Appl. Artif. Intell.*, 116:105347, 2022.

[64] Z. Wang, X. Zhao, Z. Han, L. Luo, J. Xiang, S. Zheng, G. Liu, M. Yu, Y. Cui, S. Shittu and M. Hu. Advanced big-data/machine-learning techniques for optimization and performance enhancement of the heat pipe technology – a review and prospective study. *Appl. Energy*, 204:116969, 2021.

[65] R. Vaish, U. D. Dwivedi, S. Tewari and S. M. Tripathi. Machine learning applications in power system fault diagnosis: Research advancements and perspectives. *Eng. Appl. Artif. Intell.*, 106:104504, 2021.

[66] G. Singer and Y. Cohen. A framework for smart control using machine-learning modeling for processes with closed-loop control in Industry 4.0. *Eng. Appl. Artif. Intell.*, 102:104236, 2021.

[67] M. Aliramezani, C. R. Koch and M. Shahbakhti. Modeling, diagnostics, optimization and control of internal combustion engines via modern machine learning techniques: A review and future directions. *Prog. Energy Combust. Sci.*, 88:100967, 2022.

[68] M. Ihme, W. T. Chung, A. A. Mishra. Combustion machine learning: principles, progress and prospects. *Prog. Energy Combust. Sci.*, 91:101010, 2022.

[69] N. Otsu. A threshold selection method from gray-level histogram. *IEEE Trans. Syst. Man. Cybern.*, 9(1):62-66, 1979.

[70] R. M. Haralick, K. Shanmugam and I. Dinstein. Textural features for image classification. *IEEE Trans. Syst. Man. Cybern.*, SMC-3(6):610-621, 1973.

[71] A. Hanuschkin, S. Zündorf, M. Schmidt, C. Welch, J. Schorr, S. Peters, A. Dreizler and B. Böhm. Investigation of cycle-to-cycle variations in a spark-ignition

engine based on a machine learning analysis of the early flame kernel. *Proc. Combust. Inst.*, 38(4):5751-5759, 2021.

[72] Z. Zhao, M. Hui, M. Liu, L. Dong, X. Liu and Y. Zhao. Centroid shift analysis of microlens array detector in interference imaging system. *Opt. Commun.*, 254:132-, 2015.

[73] K. Sreedhar. Enhancement of images using morphological transformations. *Int. J. Comput. Sci. Inf. Technol.*, 4(1):33-50, 2012.

[74] G. C. Cawley and N. L. C. Talbot. On over-fitting in model selection and subsequent selection bias in performance evaluation. *J. Mach. Learn. Res.*, 11:2079-107, 2010.

[75] M. J. Abdulaal, A. J. Casson and P. Gaydecki. Performance of nested vs. non-nested SVM cross-validation methods in visual BCI: Validation study. *26th European Signal Processing Conference (EUSIPCO)*, 1680-4, 2018.

[76] J. Wainer and G. Cawley. Nested cross-validation when selecting classifiers is overzealous for most practical applications. *Expert Syst. Appl.*, 182:115222, 2021.

[77] European Commission, Directorate-General for Research and Innovation, V. Battaglia, J. Niska, V. Cuervo Piñera and M. Fantuzzi. High efficiency low NOX BFG based combustion systems in steel reheating furnaces (HELNOx-BFG): final report. Publications Office, 2018.

[78] P. D. Nguyen, G. Ghazal, V. C. Piñera, V. Battaglia, A. Rensgard, T. Ekman and M. Gazdallah. Modelling of flameless oxy-fuel combustion with emphasis on radiative heat transfer for low calorific value blast furnace gas. *Energy Procedia*, 120:492-9, 2017.

[79] H. T. Nguyen, C. Barnaud, P. Domingo, P. D. Nguyen and L. Vervisch. Large-eddy simulation of flameless combustion with neural-network driven chemistry. *Appl. Energy Combust. Sci.*, 14:100126, 2023.

[80] K. I. Khidr, Y. A. Eldrainy and M. M. EL-Kassaby. Towards lower gas turbine emissions: Flameless distributed combustion. *Renew. Sust. Energy Rev.*, 67:1237-66, 2017.

[81] V. M. Reddy, D. Sawant, D. Trivedi and S. Kumar. Studies on a liquid fuel based two stages flameless combustor. *Proc. Combust. Inst.*, 34(2):3319-26, 2013.

[82] R. A. Yetter, I. Glassman and H. C. Gabler. Asymmetric whirl combustion: a new low NOx approach. *Proc. Combust. Inst.*, 28(1):1265-72, 2000.

[83] J. Blauwens, B. Smets and J. Peeters. Mechanism of "prompt" NO formation in hydrocarbon flames. *Symp. (Int.) Combust.*, 16(1):1055– 1064, 1977.

[84] W. Zheng, L. Pang, Y. Liu, F. Xie and W. Zeng. Effects of methane addition on laminar flame characteristics of premixed blast furnace gas/air mixtures. *Fuel*, 302:121100, 2021.

[85] E. S. Cho and S. H. Chung. Numerical evaluation of NOx mechanisms in methane-air counterflow premixed flames. *J. Mech. Sci. Technol.*, 23:659-666, 2009.

[86] Z. Ahmadi and M. Z. Targhi. Thermal performance investigation of a premixed surface flame burner used in the domestic heating boilers. *Energy*, 236:121481, 2021.

[87] Y. Ding, D. Durox, N. Darabiha and T. Schuller. Chemiluminescence based operating point control of domestic gas boilers with variable natural gas composition. *Appl. Therm. Eng.*, 149:1052– 1060, 2019.

[88] S. L. Sheehe and S. I. Jackson. Identification of species from visible and near-infrared spectral emission of a nitromethane-air diffusion Flame. *J. Mol. Spectrosc.*, 364:111185, 2019.

[89] C. Toro, S. Torres, V. Parra, R. Fuentes, R. Castillo, W. Diaz, G. Reyes, E. Balladares and R. Parra. On the detection of spectral emissions of iron oxides in combustion experiments of pyrite concentrates. *Sensors*, 20(5):1284, 2020.

[90] I. Glassman. *Combustion*. Elsevier, 1996.

[91] Z. Han, M. M. Hossain, Y. Wang, J. Li and C. Xu. Combustion stability monitoring through flame imaging and stacked sparse autoencoder based deep neural network. *Appl. Energy*, 259:114159, 2020.

[92] H. W. Huang and Y. Zhang. Flame colour characterization in the visible and infrared spectrum using a digital camera and image processing. *Meas. Sci. Technol.*, 19:085406, 2008.

[93] S. Karnani and D. Dunn-Rankin. Visualizing CH* chemiluminescence in sooting flames. *Combust. Flame*, 160(10):2275-2278, 2013.

[94] T. Li, C. Zhang and D. Liu. Simultaneously retrieving of soot temperature and volume fraction in participating media and laminar diffusion flame using multi-spectral light field imaging. *Int. J. Therm. Sci.*, 193:108472, 2023.